Interplay of Interaction and Topology

From Topological Band Theory to Topological Field Theory

A thesis submitted in partial fulfillment
for the degree of
Doctor of Philosophy
In the Faculty of Science

Submitted By
Gaurav Kumar Gupta

Supervisor
Dr. Tanmoy Das
& Prof. H. R. Krishnamurthy

Department of Physics
Indian Institute of Science
Bangalore – 560012

October 2018

Declaration

I, hereby, declare that the work reported in this thesis has been carried out in the Department of Physics, Indian Institute of Science, under the supervision of Dr. Tanmoy Das and Prof. H. R. Krishnamurthy. I also declare that this work has not formed the basis for the award of any Degree, Diploma, Fellowship, Associateship or similar title of any University or Institution.

In keeping with the general practice of reporting scientific observations, due acknowledgment has been made whenever the work described is based on the findings of other investigators. Any omission which might have occurred by oversight or error in judgment is regretted.

Gaurav Kumar Gupta
Department of Physics
Indian Institute of Science
Bangalore–560012, Karnataka, India

To,

My family

List of Publications

Based on this thesis:

1. Quantum Spin Hall density wave insulator of correlated fermions. **Gaurav Kumar Gupta**, Tanmoy Das, Phys. Rev. B (Rapid Comm.) **95**, 151109 (2017) (arXiv:1703.07629)

2. Axion-Higgs interplay and anomalous magnetic phase diagram in TlCuCl3, **Gaurav Kumar Gupta**, Kapildeb Duloi, Abhinav Mishra, D.D. Sarma, Tanmoy Das. (arXiv:1805.00166) (Under Review)

3. Bosonic Quantum Hall effect in an interacting lattice model, **Gaurav Kumar Gupta**, H.R. Krishnamurthy, Subhro Bhattacharjee. (ongoing work)

Other works:

1. 3D SSH model: A new model for topological insulators, **Gaurav Kumar Gupta**, Kapildeb Duloi, Tanmoy Das. (Ongoing work)

2. Statistics-tuned phases of pseudofermions in one dimension, Adhip Agarwala, **Gaurav Kumar Gupta**, Subhro Bhattacharjee, Vijay B. Shenoy. (arXiv:1811.11776)

3. Surprises in the t-J model: Implications for cuprates, A. V. Mallik, **Gaurav Kumar Gupta**, Vijay B. Shenoy and H. R. Krishnamurthy. (arXiv:1805.02429)

4. Discovery of highly spin-polarized conducting surface states in the strong spin-orbit coupling semiconductor Sb_2Se_3, Shekhar Das, Anshu Sirohi, **Gaurav Kumar Gupta**, Suman Kamboj, Aastha Vasdev, Sirshendu Gayen, Prasenjit Guptasarma, Tanmoy Das, and Goutam Sheet, Phys. Rev. **B** 97, 235306 (2018) (arXiv: 1801.00929)

5. Large Landau level splitting with tunable one-dimensional graphene superlattice probed by

magneto capacitance measurements, Manabendra Kuiri, **Gaurav Kumar Gupta**, Yuval Ronen, Tanmoy Das, and Anindya Das, Phys. Rev. **B** 98, 035418 (arXiv:1801.06630)

6. Probing the Fermi surface and magnetotransport properties in $MoAs_2$, Ratnadwip Singha, Arnab Pariari, **Gaurav Kumar Gupta**, Tanmoy Das, Prabhat Mandal, Phys. Rev. B **97**, 155120 (2018) (arXiv:1708.07294)

Acknowledgment of Collaborative Contributions

1. The content presented in chapter 3 has contributions from Kapildeb Duloi and Abhinav Mishra. The collaboration is duly acknowledged.

Preface

In this thesis I have studied three problems of current interest:

- Quantum Spin Hall Density Wave Insulator of Correlated Fermions,
- Higgs-Axion conversion and anomalous magnetic phase diagram in $TlCuCl_3$, and
- Bosonic integer and fractional quantum Hall effect in an interacting lattice model

In the first piece of work, I present the theory of a new type of topological quantum order which is driven by the spin-orbit density wave order parameter and distinguished by Z_2 topological invariant. The resulting quantum order parameters break translational symmetry but preserve time-reversal symmetry. As a consequence, the system is inherently associated with a Z_2 topological invariant along each density wave propagation direction which makes it a weak topological insulator in two dimensions, with an even number of spin-polarized boundary states. In the second work, I discuss the effect of the parent topological ground state on the local order. In particular, I focus on a well-studied (experimentally) material $TlCuCl_3$ and show that it has unique unexplored topological properties which arise when a time reversal breaking antiferromagnetic order parameter sets into the system and how they can explain the uncanny properties of this material such as unconventional paramagnon lifetime, finite Higgs mass across the phase transition, among other. In the last work, I discuss our attempt to confirm the presence

of bosonic integer and fractional quantum Hall effect in an interacting lattice model. The model consists of bosons spread over the honeycomb lattice with the nearest neighbor and next nearest correlated hopping with π flux per hexagon. I provide evidence for the presence of integer as well as fractional quantum Hall states and also a superfluid state, for different fillings and tuning parameters.

I have used mean field theory and path integral methods as the theoretical tools to study the above problems. Furthermore, I have also used numerical methods such as Density Functional Theory (DFT, as implemented in VASP) and exact diagonalization (using Lanczos algorithm) where appropriate. As I have shown in the thesis, a large number of interesting results emerge from these studies, leading to a better understanding of the problems and uncovering some interesting underlying physics.

This thesis is organized as follows. The first two chapters serve as an introduction. In Chapter 1, I give an introductory overview of topological band theory and topological field theory keeping in mind their relevance for the problems dealt with in the later chapters. In Chapter 2, I give a brief introduction to the field theoretic methods that are used in the thesis.

In Chapter 3, I present the theory of a new type of topological quantum order which is driven by the spin-orbit density wave order parameter and distinguished by a Z_2 topological invariant. I show that when two oppositely polarized chiral bands [resulting from the Rashba-type spin-orbit coupling α_k, where k is the crystal momentum] are significantly nested with a special nesting wavevector $\mathbf{Q} \sim (\pi, 0)/(0, \pi)$, this induces a spatially modulated inversion of the chirality ($\alpha_{k+Q} = \alpha_k^*$) between different sublattices. The resulting quantum order parameters break translational symmetry but preserve time-reversal symmetry. They are inherently associated with a Z_2-topological invariant along each density wave propagation direction. Hence it gives rise to a weak topological insulator in two dimensions, with an even number of spin-polarized boundary states. This phase is analogous to the quantum spin-Hall state, except here the time-reversal polarization is spatially modulated, and thus it is dubbed quantum spin-Hall density

wave (QSHDW) state. This order parameter can be realized or engineered in quantum wires, or quasi-2D systems, by tuning the spin-orbit coupling strength and chemical potential to achieve the special nesting condition.

In Chapter 4, I focus on the experimentally well-studied material, $TlCuCl_3$ and ask the question: what is so unique in $TlCuCl_3$ which drives so many unique magnetic properties, such as a massive Higgs mode at the magnetic critical point, long-lived paramagnons, and dimerized antiferromagnetism? To answer these questions, I employ a combination of *ab-initio* band structure, tight-binding parametrization, and an effective quantum field theory. Within a density-functional theory (DFT) calculation, I find an unexpected bulk Dirac cone without spin-orbit coupling (SOC). Tracing back its origin, I identify, for the first time, the presence of Su-Schrieffer-Heeger (SSH) like dimerized Cu chains hidden in the 2D crystal structure. The SSH chains, combined with SOC, stipulates an anisotropic 3D Dirac cone where chiral and helical states are intertwined (namely, 3D SSH model). As a Heisenberg interaction is introduced, I show that the dimerized Cu sublattices of the SSH chains condense into dimerized spin-singlet magnets. In the magnetic ground state, I also find a naturally occurring topological phase, distinguished by the axion invariant. Finally, to study how the topological axion excitations couple to magnetic excitations, I derive a Chern-Simons-Ginzburg-Landau action from the 3D SSH Hamiltonian. I find that axion term provides an additional mass term to the Higgs mode, and a lifetime to paramagnons, which are independent of the quantum critical physics.

Finally, in Chapter 5, I numerically explore the presence of bosonic integer and fractional quantum Hall effect in an interacting lattice model. Our model consists of bosons on a bipartite honeycomb lattice with correlated next nearest neighbor hopping and π magnetic flux per unit cell. I use Exact Diagonalization (ED), employing the Lanczos algorithm to calculate the ground state as well as few excited states with an aim to characterize the different phases of the system and to find preliminary evidence for integer as well as fractional quantum Hall effect of bosons. I provide evidence to show that the ground state of the Hamiltonian can host a bosonic integer

quantum Hall effect (BIQHE) as well as a bosonic fractional quantum Hall effect (BFQHE), and also a superfluid (SF) phase, depending upon the parameter choice and the filling. The most attractive property of our model is the presence of both a symmetry protected topological (SPT) phase and a non-SPT phase at different fillings. Although the BIQH phase is an example of symmetry protected topological (SPT) phase, the BFQH phase is not and hence it can host fractional bosonic excitations as well. I have tried to establish this by explicitly calculating the charge pump by threading a 2π flux through the central hexagon of the system.

In Chapter 6, I conclude the thesis by first summarizing the results that I have presented in the thesis and then discussing their limitations. Later on, I comment on the possible directions for future work to uncover more physics in the problems I've discussed and for getting a better understanding of deeper problems.

Acknowledgment

First and foremost, I would like to express my sincere gratitude to my Ph.D. advisors, Tanmoy Das and H. R. Krishnamurthy, for being encouraging and inspiring and for their commitment and dedication to my work, career and personal life. It has been a great privilege to work with them. I owe them for the many ways they shaped my career thus far, and the career that lies ahead.

I would like to thank my fellow physicists along with my collaborators, for the many wonderful discussions I shared with them. They have inspired, challenged, and taught me to become a better physicist. I'm also indebted to the IISc Physics Department staffs, for their ability to keep the department running smoothly, to allow us to focus on our work.

I would also like to thank our present and past chairman for their numerous support be it academic or non-academic, they were always supportive. I've taken a number of courses from a lot of people in the department and outside. They have shown me how much there is to learn, and I have greatly benefited from their experience; I aspire to be a great teacher just as they are.

Finally, my family has been a tremendous source of support for me through my years in IISc. Their unwavering support has given me the strength to overcome the challenges that I have faced in my life. Without their love and kindness, I would not be where I am today; I dedicate this thesis to them.

Contents

List of Figures

1

Introduction and Overview

Condensed matter physics is a branch of physics that provides a framework for describing the physical properties of the phases of matter in the condensed form. The aim is to understand these phases based on the known laws of physics, mostly considering the low energy properties of the system. It is needless to mention that the number of degrees of freedom ($\sim 10^{23}$) in the system is too large to deal with individually[8]. We can, however, measure/calculate some of the properties of the system (e.g., density, magnetization, response to the external field, etc.) which can be used to characterize and distinguish the phases of the system. The general idea of characterizing a phase is to find some kind of order parameter, e.g., charge density for charge density wave, magnetization for ferromagnet, staggered-magnetization for anti-ferromagnet, polarization for ferroelectric, etc. If the system posses finite expectation value of any of the order parameters, it is classified into that phase. This way of classifying phases falls under the well known Landau symmetry breaking paradigm [9]. Landau's theory of symmetry breaking provides a semi-phenomenological framework to explain the phase transition from a symmetric

phase (such as at high temperature) to a less symmetric, broken symmetry phase (at extreme conditions such as low-temperature) through a phase transition, accompanied by singular changes in the thermodynamic entities. Such phase transitions can also occur (as the parameters in the Hamiltonian are varied) at zero temperature and are dubbed quantum phase transitions.

However, in the last three decades or so, it has become clear that there are phases which do not possess any local order, instead, they (sometimes) have (highly) non-local order. One of the experimentally verified examples is the fractional quantum Hall (FQH) state which has a highly non-local order which corresponds to annihilating an electron and unwinding a number of fluxes. These phases are called *"topological"* phases without any local order. A general definition of topological phase would be ~~*"a* phase of matter characterized by a topological invariant (a non-local order parameter) rather than a local order parameter"~~ *"a phase whose effective action contains a topological term, i.e., a term that is invariant under smooth deformations of the manifold."*. Recently, topological phases got a surge of attention because of the proposal of *"topological quantum computation"* using non-abelian anyons of FQH states [10]. Since the order is highly non-local in FQH, the information stored is less susceptible to local decoherence processes [10, 11].

The area of topological insulators (TIs) started back in the 80s when von Klitzing *et al.*[1] discovered the quantum Hall effect (QHE). Astonishingly, they found plateaus in the transverse Hall conductivity (σ_{xy}) at high magnetic fields (Fig. 1.1) in a usual two-dimensional electron gas (2 DEG) Hall device. Hall conductivity (same as conductance in 2-D geometry) is defined as

$$\sigma_{xy} = \frac{j_x}{E_y} \equiv \frac{1}{\rho_{xy}}, \tag{1.1}$$

where j_x is the current density along x direction and E_y is the electric field (developed) along y direction, in the presence of a magnetic field applied in the z direction. In a classical picture, the transverse resistivity, ρ_{xy} is proportional to the applied magnetic field **B**. On the contrary, for the

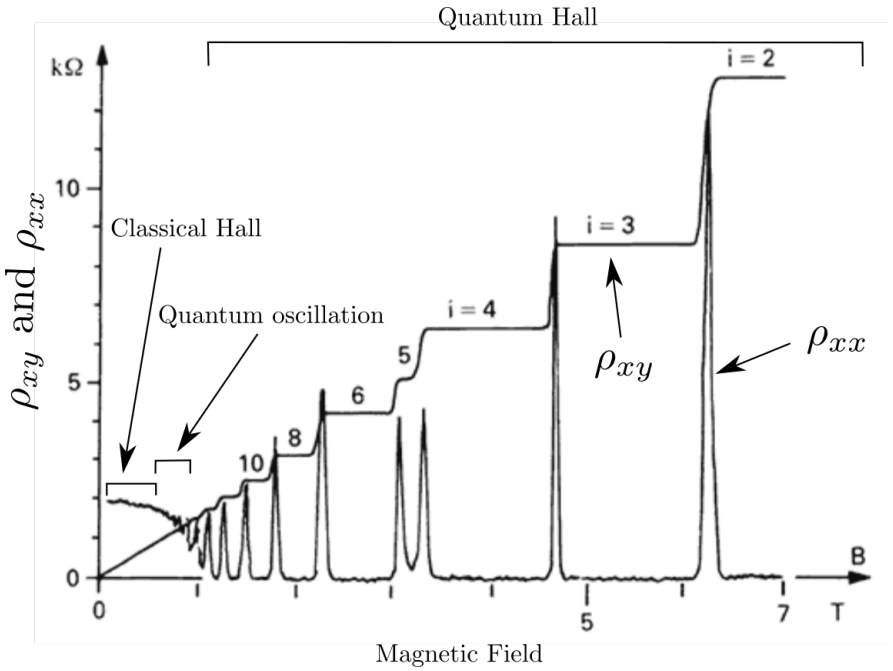

Figure 1.1: Experimental plot showing the plateaus in ρ_{xy} and zeros of ρ_{xx}[1].For small magnetic field, resistance grows linearly with $\mathbf{B}$ which corresponds to the classical Hall effect. In the intermediate magnetic field, ρ_{xx} shows oscillation and this region correspond to the quantum oscillation regime. At the high magnetic field, we see plateaus in ρ_{xy}, where $\rho_{xx} \to 0$.

high magnetic field, transverse Hall conductivity was found to have a structure with steps (see Fig. 1.1), with the flat plateaus exactly quantized as:

$$\sigma_{xy} = \nu \frac{e^2}{h}, \tag{1.2}$$

where e is the electronic charge, h is Plank's constant and ν is an integer. This phenomenon was dubbed as the quantum version of the Hall effect or Quantum Hall Effect (QHE). [1] Later on Thouless *et al.*[12] along with Simon [13] showed the connection between QHE and the topology of Bloch wave functions. They showed that σ_{xy} is quantized as long as there exists an

[1]Essentially the Hall resistance data shown in Fig. 1.1 can be split into three regions, weak, intermediate and strong magnetic field. In the weak field region, ρ_{xy} goes linearly with $\mathbf{B}$ and ρ_{xx} is constant, which is the classical Hall regime. At strong magnetic fields, we see plateaus in ρ_{xy} with $\rho_{xx} \to 0$, which is the Quantum Hall regime. In the middle, we see oscillation in ρ_{xx}, which can be understood in a semi-classical approximation, where the density of states at the Fermi level oscillates because of the crossing of Landau Levels across the Fermi-level.

insulating gap in the bulk energy spectrum. ν ($\nu \in \mathbb{Z}$) is nothing but the first Chern number. In 1988, Haldane showed that one doesn't even need an external magnetic field to observe QHE, but breaking the time-reversal symmetry (TRS) is necessary[14], in addition to a non-trivial band structure (defined later).

Since σ_{xy} [2] is odd under the time reversal (j_x changes sign in Eq. (1.1) while E_y remains the same), σ_{xy} vanishes in TRS systems and hence this classification is not applicable on TRS systems. Later on, Kane and Mele showed that even in TRS systems, a distinct topological invariant can be defined by subtracting the Hall conductance of the two copies of the Hamiltonian which are time-reversal conjugate to each other, but individually they break TRS. This can be conveniently done in spin-systems where spin is a good quantum number, and hence one obtains quantum spin Hall (QSH) insulator in 2D[15]. Finally, a more general version of the topological invariant was deduced for TRS systems in 2D and 3D where the Hall conductance was replaced by the "TR polarization", giving rise to a $\mathbb{Z}_2$ [3] classification of the topological insulators. Both 2D and 3D TI's were subsequently observed experimentally[16, 17, 18, 19, 20]

Using the von Neumann-Wigner classification[21] of level crossing, it can be shown that fundamental time reversal breaking (TRB) insulators exist in 2+1 D (and are classified by the first Chern number), whereas the fundamental TRS insulators exist in 4+1 D (and are classified by the second Chern number). It turns out that all the TRS insulators in 1,2 or 3-D can be understood from the 4+1 D Chern-Simons theory using a so-called procedure of dimension reduction[22].

The purpose of this chapter is to serve as an introduction to and a brief review of the theoretical concepts of topological band theory. The next chapter serves as an introduction to the Landau kind of symmetry breaking phase transition, and some numerical tools which are used to study

[2] Strictly speaking, the Hall conductivity is $(\sigma_{xy} - \sigma_{yx})/2$. If the lab axes are not aligned with the principal axes of a lattice, σ_{xy} will have a symmetric part too, but this is even under time-reversal and non-topological.

[3] On the other hand the Chern number classifies insulators into an infinite number of topologically different classes ($\nu \in \mathbb{Z}$).

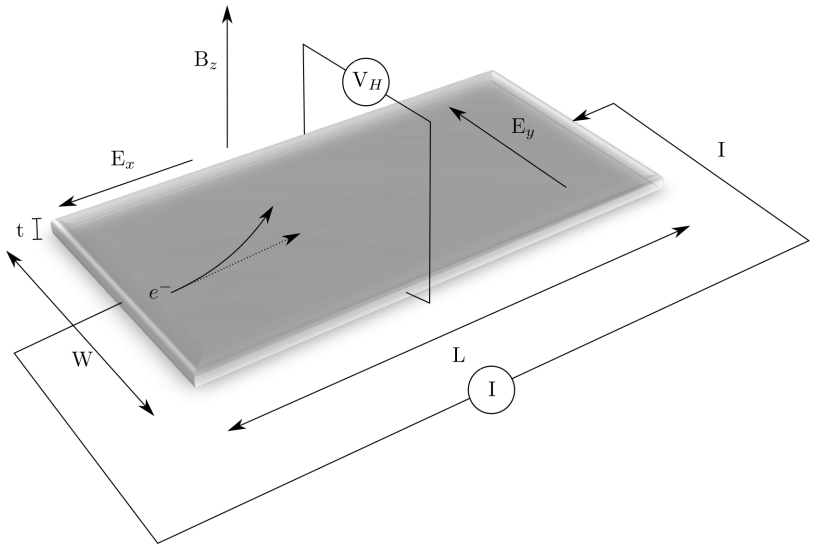

Figure 1.2: Schematic of the classical Hall measurement having a Hall bar of width W, length L and thickness t (t<<W). A magnetic field B_z is applied perpendicular to the surface of the Hall bar and a current I is made to flow along the length of the sample. An electric field, E_y and Hall voltage, V_H is developed along the width of the sample.

the problems discussed in the further chapters. There are many excellent books covering these fields in much greater depths and details [23, 24, 25, 26].

The aim of this thesis is to combine the effects of interaction and topology, to address their interplay and the resultant new states of matter. Here we deploy a number of analytical and numerical techniques such as mean field theory, path-integral, DFT(as implemented in VASP), numerical diagonalization, etc., to study this interconnection. There are already several known examples of interaction-driven topological phases such as anti-ferromagnetic topological insulator[27], topological Mott insulator[28], topological Kondo insulator[29], topological superconductors[30, 31, 32], etc.

1.1 Classical Hall Effect

In 1879, Edwin Hall found that when an electrical conductor is subjected to a perpendicular electric and magnetic fields, it develops a voltage difference perpendicular to both the applied fields [33]. Here we have electrons confined in two-Dimensions (2D) (say the $x-y$ plane), and we apply a constant magnetic field $\mathbf{B}$ along the $\hat{z}$ direction (i.e., $\mathbf{B} = B_0\hat{z}$) and a current I_x is made to flow along the x-direction by the application of an electric field E_x as shown in the Fig. 1.2. The magnetic field deflects the electrons due to Lorentz force, opposite charge accumulates at the edges transverse to the current, leading an electric field (E_y) between the edges. In the Drude picture, the equation of motion is given by

$$m\frac{d\mathbf{v}}{dt} = -e\mathbf{E} - e\mathbf{v}\times\mathbf{B} - \frac{m\mathbf{v}}{\tau}, \tag{1.3}$$

where τ is the relaxation time[4]. The equilibrium solution of the above equation ($d\mathbf{v}/dt = 0$) is

$$\mathbf{v} + \frac{e\tau}{m}\mathbf{v}\times\mathbf{B} = -\frac{e\tau}{m}\mathbf{E}. \tag{1.4}$$

As the current density is given by

$$\mathbf{J} = -ne\mathbf{v} = \sigma\mathbf{E}, \tag{1.5}$$

where n is the density of the charge carrier and σ is the conductivity tensor. Eq. 1.4 can be written as

$$\begin{pmatrix} 1 & \omega_B\tau \\ -\omega_B\tau & 1 \end{pmatrix}\mathbf{J} = \frac{e^2 n\tau}{m}\mathbf{E}, \tag{1.6}$$

[4]relaxation time (τ) is the time duration between two subsequent collisions of the particles by the scatterer.

where $\omega_B = eB/m$ is the cyclotron frequency. From the above equation, we get

$$\sigma = \frac{\sigma_{DC}}{1+\omega_B^2\tau^2}\begin{pmatrix} 1 & -\omega_B\tau \\ \omega_B\tau & 1 \end{pmatrix}, \tag{1.7}$$

where $\sigma_{DC} = \frac{ne^2\tau}{m}$ is the DC conductivity in the absence of the magnetic field. Now we can define the resistivity (ρ) by

$$\rho = \sigma^{-1} = \frac{1}{\sigma_{DC}}\begin{pmatrix} 1 & \omega_B\tau \\ -\omega_B\tau & 1 \end{pmatrix} = \frac{m}{ne^2}\begin{pmatrix} \frac{1}{\tau} & \omega_B \\ -\omega_B & \frac{1}{\tau} \end{pmatrix}. \tag{1.8}$$

The remarkable property of the above equation is the absence of τ in ρ_{xy} which means that it doesn't get affected by the disorder and captures some intrinsic properties of the material.

The potential drop (V_y) between the edges of the Hall bar is $V_y = E_y W$ (W is the width of the Hall bar). The transverse resistance (R_{xy}) is defined as the ratio of the transverse voltage to the electric current.

$$R_{yx} = \frac{V_y}{I_x} = \frac{LE_y}{LJ_x} = \frac{E_y}{J_x} = -\rho_{xy} \tag{1.9}$$

We can also define the Hall coefficient as

$$R_H = -\frac{E_y}{J_x B} = \frac{\rho_{xy}}{B} \tag{1.10}$$

which in Drude model gives

$$R_H = \frac{\omega_B}{B\sigma_{DC}} = -\frac{1}{ne} \tag{1.11}$$

The remarkable property of the above equation is that R_H only depends on the carrier density and the sign of its charge. Because of this property Hall measurement is commonly done to determine the carrier density and carrier type (i.e., electron or hole) and sometimes they are also used to measure the magnetic field as well.

1.2 Quantum Hall Effect

When the electrons are confined in 2D[5], the applied magnetic field is high and the sample is pure enough[6], von Klitzing *et al.*[1] found that ρ_{xy} develops plateaus as a function of $\mathbf{B}$,

$$\rho_{xy} = -\frac{h}{\nu e^2}, \tag{1.12}$$

where ν is an integer. This is contrary to the classical Hall effect (Eq. (1.9)) where ρ_{xy} changes linearly with the applied magnetic field. In addition, ρ_{xx} (the longitudinal resistivity) vanishes at these plateaus (Fig. 1.1). State-of-the-art experiments have confirmed the quantization of ν with the accuracy of a part in a billion. As the name suggests, classical equations cannot explain this phenomenon and we need to fully invoke quantum theory to solve this problem.

1.2.1 Landau Levels

The Hamiltonian of a free electron in the magnetic field is given by

$$\mathcal{H} = \frac{1}{2m}\left(\mathbf{p} + e\mathbf{A}\right)^2 = \frac{1}{2m}\mathbf{\Pi}^2, \tag{1.13}$$

where m is the mass of the electron, p is the momentum, e is the electronic charge and $\mathbf{A}$ is the vector potential. A solution of the above Hamiltonian can be reduced to the solution of a degenerate set of harmonic oscillators[7] and the discrete levels are commonly known as Landau

[5] We need the confinement along the z-direction to make sure that the discrete levels because of the "z" quantum numbers (because of the confinement along z direction) are well separated in energy and the higher ones can be neglected. This can be achieved in many heterostructure which are commonly known as 2D electron gas (2 DEG)

[6] We need pure sample but a small disorder is always required to see the QHE, otherwise one is expected to see a linear resistivity curve similar to the classical Hall resistivity in a pristine sample.

[7] One can easily see this by choosing a gauge, lets say Landau gauge ($\mathbf{A} = (-B_0 y, 0, 0)$). Since $\mathcal{H}$ is now independent of x, the solution to the Schrödinger equation will be a plane wave along the $x-$direction. Now the Hamiltonian in Eq. (1.13) becomes

$$\mathcal{H} = \frac{1}{2m}\left(\hbar k - eB_0 y\right)^2 + \frac{1}{2m}p_y^2$$

Levels (LL) with the energy $\left(n+\frac{1}{2}\right)\hbar\omega_B$ where $\omega_B = eB_0/m$ is the cyclotron frequency. These energy levels (Landau Levels) are highly degenerate with the degeneracy $N = AB_0/\phi_0$, where A is the area of the sample and $\phi_0 = 2\pi\hbar/e$ is the flux quanta. When the n^{th} LL is completely filled (filling factor, $\nu = n$), the Hall conductance is $\sigma_{xy} = ne^2/h$. It turns out that these quantized values of σ_{xy} are robust against weak disorder and interaction, and the accuracy of the quantization is one part in a billion.

The relationship between the Hall conductivity and Bloch wave functions was famously demonstrated by TKNN[12] along with Simon and co-workers[13, 34]. For a particle in a periodic potential, the wave functions are given by

$$\psi^{\alpha}_{\mathbf{k}}(\mathbf{r}) = e^{i\mathbf{k}.\mathbf{r}}u^{\alpha}_{\mathbf{k}}(\mathbf{r}), \tag{1.14}$$

with $u^{\alpha}_{\mathbf{k}}(\mathbf{r})$ being periodic over the unit cell ($u^{\alpha}_{\mathbf{k}}(\mathbf{r}+\mathbf{a}) = u^{\alpha}_{\mathbf{k}}(\mathbf{r})$ where $\mathbf{a}$ is the lattice translation vector) and α the band index. We can now describe the topology underlying the QHE but before that, we need to satisfy the following three conditions:

- the Brillouin Zone (BZ) is a torus, T^2. With some assumptions, this can be satisfied even in the presence of magnetic field and consequently the energy levels of the system organize themselves into energy bands[8],
- electrons do not interact with each other[9], and
- the system is an insulator.

Based on the above assumption and using the Kubo formula[10], the transverse conductivity σ_{xy}

which is equivalent to the problem of a harmonic oscillator along the $y-$direction.

[8] As long as the ratio of the flux through a unit-cell to the flux quanta is a rational number, we can write $\phi/\phi_0 = p/q$. Hence making a super-cell of q unit cells, the flux through it becomes an integral multiple of ϕ_0. This new unit-cell is known as the magnetic unit-cell

[9] such that a single particle picture is valid but the idea can be generalized even for interacting electrons

[10] Kubo formula is used to calculate the linear response using correlation functions[35]

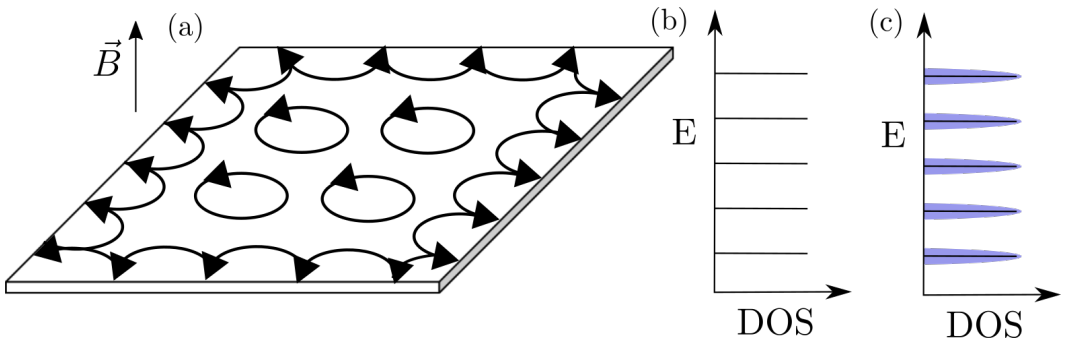

Figure 1.3: (a) Cartoon showing the cyclotron orbits of electrons in the presence of perpendicular magnetic field as well as a skipping orbit on the edge. (b-c) the density of states (DOS) in QH system (b) in the absence of disorder and (c) in the presence of disorder.

can be shown to take the form [36]

$$\sigma_{xy} = \frac{ie^2}{\hbar}\sum_{\alpha}\oint_{T^2}\frac{d^2\mathbf{k}}{(2\pi)^2}\left(\langle\partial_y u^{\alpha}_{\mathbf{k}}|\partial_x u^{\alpha}_{\mathbf{k}}\rangle - \langle\partial_x u^{\alpha}_{\mathbf{k}}|\partial_y u^{\alpha}_{\mathbf{k}}\rangle\right). \tag{1.15}$$

It turns out that the above integral is quantized[36] as long as the bulk gap remains (will show it in the upcoming section) and it can be written as

$$\sigma_{xy} = -\frac{e^2}{2\pi\hbar}\sum_{\alpha} c_{\alpha}, \tag{1.16}$$

where $c_\alpha \in \mathbb{Z}$ and α runs over the filled bands, although, unless the circumstances are such that bands have non-trivial topology, the c_α's are all zero. This equation is interesting in many ways. First of all, it doesn't depend on the energy, except to determine which bands are to be summed over (filled bands). That means small deformation to the Hamiltonian doesn't affect σ_{xy}. As long as the system is gapped, σ_{xy} is always quantized.

1.2.2 Gapless chiral edge states

How does an insulator give finite and precise conductivity? The answer to this question lies on the edge of the system. *Topological* insulators, as opposed to *trivial* insulators, have conducting

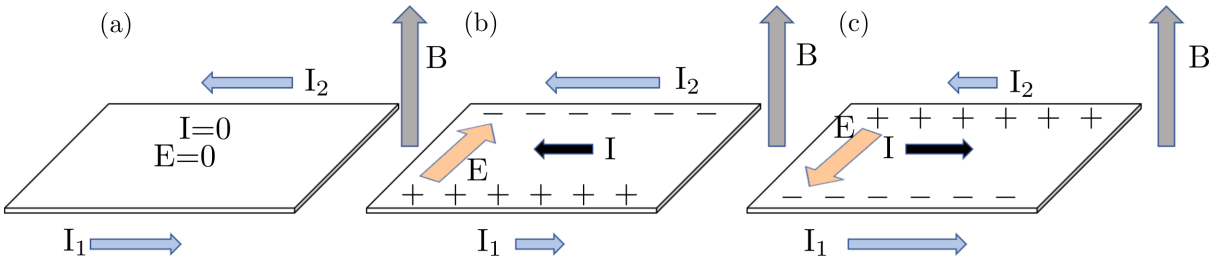

Figure 1.4: Cartoon picture of chiral edge states in the Quantum Hall system.

chiral edge states which are *topologically protected*. Here the chirality means that the states are directional, i.e, particles in these states move in a particular direction. This can be understood well in a semi-classical picture. At a high enough magnetic field, the cyclotron radius is small enough such that the electrons in the bulk do not see the edge and are localized. For electrons near the boundary, they collide with the boundary and move in *"skipping orbits"* which leads to a current along the edge as shown in Fig. 1.3(a). The existence and chirality of the quantum version of these, the edge states, are topologically protected, that means they are robust against local interactions and disorder as long as the bulk is gapped. The reason behind this is quite simple, each edge hosts edge states of same chirality that lie within the band gaps of the insulator and hence decay exponentially into the bulk. Since the states of other chirality are physically very far on the other edge, small local interaction and disorder cannot scatter them into each other, and hence they are protected.

Most of the topological properties of the system show up in the edge states. This intertwining is refereed to as *"bulk-boundary correspondence"* which says that while going from one topological phase to another, the gap must close[11] [37, 38, 39]. So, if we connect two Chern insulators with Chern number ν_1 and ν_2 then we will have $|\nu_1 - \nu_2|$ edge states at the interface[40, 41, 42, 43].

To explain the presence of topology and its connection to the plateaus in the transverse conductivity, we need to first understand the non-trivial properties of the Bloch wave functions

[11] In other words, phases with different topological invariants constitute different quantum phases and going form one quantum phase (say Hall insulator) to another (say vacuum) requires gap closing

One of them is the non-dynamical phase[12] acquired by the wave function while moving in the parameter space[13], known as Pancharatnam phase or Berry phase.

1.3 Pancharatnam phase or Berry phase

Pancharatnam phase or Berry phase is the phase acquired by a wave function of the system while traversing a path in parameter space adiabatically. It results from the geometric properties[14] of the parameter space of the Hamiltonian [44]. The phenomenon was independently discovered by Pancharantnam in 1956[45], and by Longuet-Higgins in 1958[46]. It was later on generalized by Berry in 1984[47]. The Berry connection ($\mathcal{A}_\alpha$) and Berry phase (γ_α) of the α^{th} band are defined as[15]

$$\mathcal{A}_\alpha(k) = i\langle\psi^\alpha_{\mathbf{k}}|\nabla_{\mathbf{k}}|\psi^\alpha_{\mathbf{k}}\rangle, \quad \gamma_\alpha = \oint_{\mathcal{O}} \mathcal{A}_\alpha . d\mathbf{k} \tag{1.17}$$

where $\mathcal{O}$ is a closed loop in k-space. It should be noted that $\mathcal{A}_\alpha$ is a gauge-dependent quantity but γ_α is not (in a closed loop). Under the gauge transformation, $\theta(k)$,

$$|\psi^\alpha_{\mathbf{k}}\rangle \rightarrow e^{i\theta(\mathbf{k})}|\psi^\alpha_{\mathbf{k}}\rangle, \tag{1.18}$$

the Berry connection and Berry phase transform as:

$$\begin{aligned} \mathcal{A}_\alpha &\rightarrow \mathcal{A}_\alpha - \nabla_{\mathbf{k}}\theta(\mathbf{k}) \\ \gamma_\alpha &\rightarrow \gamma_\alpha - (\theta_{final} - \theta_{initial}). \end{aligned} \tag{1.19}$$

As θ can only change by an integral multiple of 2π in a closed loop, γ_α can also change by an integral multiple of 2π. Since the form of Berry connection resembles close to the

[12] Non-dynamical phase is the phase which is acquired by the wave function not because of the usual time evolution but because of the other features such as geometry of the parameter space.
[13] Here it is the 2D Brillouin zone (BZ)
[14] Such as the geometry of the parameter space. In QHE, the parameter space is a 2-Torus, $\mathbb{T}^2$
[15] Detailed derivation is given in Appendix A

electromagnetic vector potential, we can define a Berry field or curvature as

$$\vec{\mathcal{F}}_\alpha(\mathbf{k}) \;=\; \vec{\nabla}_{\mathbf{k}} \times \vec{\mathcal{A}}_\alpha, \quad \mathcal{F}^a_\alpha(\mathbf{k}) = -Im\left[\epsilon^{abc}\langle\partial_b\psi^\alpha_{\mathbf{k}}|\partial_c\psi^\alpha_{\mathbf{k}}\rangle\right]. \tag{1.20}$$

Now we can define

$$\nu_\alpha = \frac{1}{2\pi}\oint_{T^2} d^2\mathbf{k}.\mathcal{F}_\alpha = \frac{\gamma_\alpha}{2\pi} \tag{1.21}$$

where $\nu(\in \mathbb{Z})$ is known as the first Chern number. On looking closely, it becomes evident that c_α in Eq. (1.16) is the same as ν defined above.

1.4 Topological phase in 1D: SSH model

The simplest example of a topological phase in 1D arises in the famous Su-Schrieffer-Hegger (SSH) model for poly-acetylene [48]. Poly-acetylene is a 1D chain of C-atoms with staggered hopping amplitude between nearest neighbor (NN) sites. This makes for a two sub-lattice unit cell[16] as shown in Fig. 1.5. The low energy Hamiltonian can be written in a "two-band" model as

$$\mathcal{H}_{SSH} = \sum_{i=1}^{N} t c^\dagger_{A,i} c_{B,i} + \sum_{i=1}^{N-1} t' c^\dagger_{A,i+1} c_{B,i} + h.c. \tag{1.22}$$

where $c^\dagger_{\alpha,i}(c_{\alpha,i})$ are the creation (anhilation) operator on the sub lattice $\alpha(= A, B)$ in the i^{th} unit cell, and t, t' are the staggered hopping as shown in the Fig. 1.5.

On performing the Fourier transformation on the above Hamiltonian, in the k-space we get

$$\mathcal{H}_{SSH} = \sum_k (t + t' e^{-ika}) c^\dagger_{A,k} c_{B,k} + h.c., \tag{1.23}$$

[16] the reason why we have di-atomic chain is because of the Peierls instability. This instability arises because of the diverging response of the Fermi sea to small perturbation in low dimensions. For details see dedicated texts such as Grüner[49] for further readings.

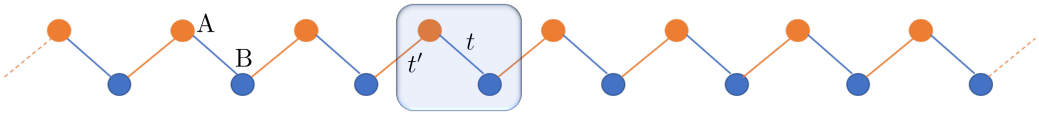

Figure 1.5: Cartoon showing the SSH model with staggered hopping

where a is the size of the unit cell and $c^{\dagger}_{\alpha,k}(c_{\alpha,k})$ are $c^{\dagger}_{\alpha,i}(c_{\alpha,i})$ equivalents in the momentum space[17]. In the matrix form, the Hamiltonian looks

$$\begin{aligned} \mathcal{H}_{SSH} &= \sum_k \begin{pmatrix} c^{\dagger}_{A,k} & c^{\dagger}_{B,k} \end{pmatrix} \mathcal{H}_{SSH}(k) \begin{pmatrix} c_{A,k} \\ c_{B,k} \end{pmatrix} \\ \mathcal{H}_{SSH}(k) &= \begin{pmatrix} 0 & t + t'e^{-ika} \\ t + t'e^{ika} & 0 \end{pmatrix} = \begin{pmatrix} 0 & h(k) \\ h^*(k) & 0 \end{pmatrix} = \mathbf{d}(k).\hat{\sigma} \end{aligned} \tag{1.24}$$

where $h(k) = t + t'e^{-ika}$, $\mathbf{d}(k) = (t + t'\cos(ka), -t'\sin(ka), 0)$ and $\hat{\sigma} = (\sigma_x, \sigma_y, \sigma_z)$ are the three Pauli matrices. Note that d_x and d_y are respectively the real and imaginary parts of $h(k)$. The eigenvalues of $\mathcal{H}_{SSH}(k)$ are given by

$$\mathcal{E}_{SSH}(k) = \pm\sqrt{t^2 + t'^2 + 2tt'cos(ka)} \tag{1.25}$$

1.4.1 Topological properties

As can be seen from the Eq. (1.25) and the band structure of $\mathcal{H}_{SSH}(k)$ in Fig. 1.6, the system is gapped $\forall t \neq t'$. But $\mathbf{d}(k)$ does not behave the same way for $|t| < |t'|$ and $|t| > |t'|$, as shown in the Fig. 1.7. This tells us that there is something different in these two cases although the band

[17] Fourier transformation is defined as:

$$c^{\dagger}_{\alpha,k} = \frac{1}{\sqrt{N}} \sum_i e^{-ik.r_i} c^{\dagger}_{\alpha,i},$$

$$c_{\alpha,k} = \frac{1}{\sqrt{N}} \sum_i e^{ik.r_i} c_{\alpha,i}$$

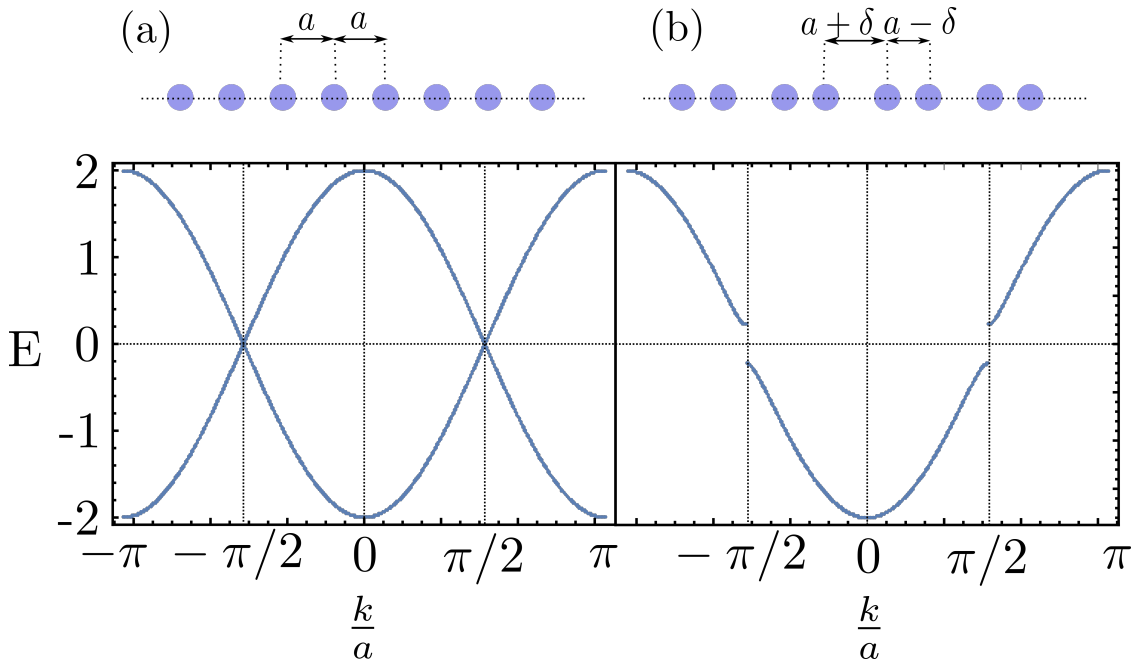

Figure 1.6: Figure showing the SSH model (a) with $|t| = |t'|$ and (b) with $|t| \neq |t'|$.

structure looks exactly the same. From Eq. 1.17, we get

$$\nu = \frac{1}{2\pi i}\int_{-\pi}^{\pi} dk \frac{d}{dk} ln(h(k)) = \frac{1}{2\pi i}\oint \frac{dh(k)}{h(k)}, \tag{1.26}$$

where $h(k) = d_x(k) - id_y(k)$ and the closed loop integral is over the circle shown in Fig. 1.7. ν is known as the winding number, which counts the number of times $\mathbf{d}(k)$ circles around the origin in $d_x - d_y$ (or the complex $h(k)$) plane (when k changes from $-\pi$ to π) as shown in the Fig. 1.7. The integrand in Eq. 1.26 has a pole at $\vec{d} \to \vec{0}$. Thus if the circle that $\vec{d}$ (or $h(k)$) traverses encircles the pole at the origin, we obtain a finite residue, otherwise zero. This is reflected in the results:

- $|t| > |t'|, \nu = 0$
- $|t| < |t'|, \nu = 1$

Here, the winding number ν can be regarded as a topological invariant.

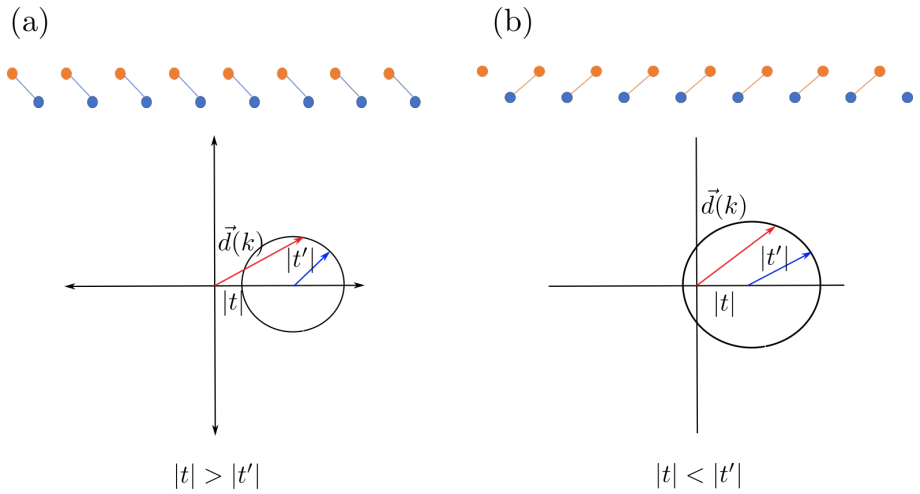

Figure 1.7: Variation of $h(k)$ in the $d_x - d_y$ [or equivalently, in the complex $h(k)$] plane for (a) with $|t| > |t'|$ and (b) with $|t| < |t'|$. If $|t| < |t'|$, $h(k)$ encircles the origin, while if $|t| > |t'|$ it doesn't.

To support the point, it can be clearly seen in Fig. 1.8 (which shows the energy eigenvalues for a finite system with open boundary condition) that these two limits are different. When $|t| > |t'|$, there is no zero energy state but when $|t| < |t'|$, there are two zero energy states.

1.4.2 Topological phase in 2D: Chern Insulator

QHE is not just limited to the system with an applied magnetic field. In 1988 Haldane[14] showed that an external magnetic field is not required but breaking TRS is necessary. The easiest way to understand this is by an example. We will take an example of Chern Insulator (CI) on a square lattice. Consider a model Hamiltonian for spin-less electrons in a two sub-lattice system in 2D given by

$$\begin{aligned} \mathcal{H}_{CI}(\mu) &= \sum_{k,\alpha,\beta} h_{\alpha\beta}(k) c^{\dagger}_{k\alpha} c_{k\beta} \\ h(k) &= [\cos(k_x) + \cos(k_y) - \mu]\, \sigma_z + \sin(k_x)\sigma_x + \sin(k_y)\sigma_y \end{aligned} \tag{1.27}$$

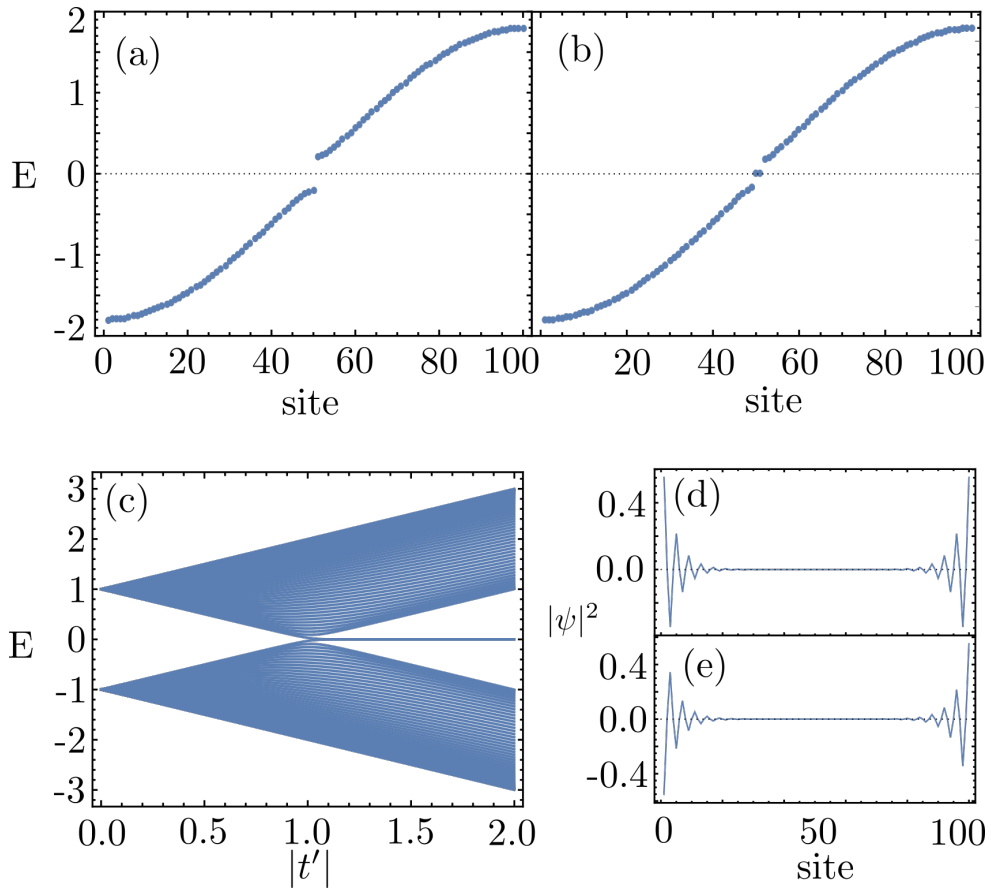

Figure 1.8: Spectrum of the finite SSH model when (a) $|t| > |t'|$ and (b) $|t| < |t'|$ and (c) as a function of $|t'|$. Spectrum in (b) shows two zero energy states. These states are localized on the boundary of the system as seen from (d) and (e).

where σ's are the Pauli matrices (operating in the space of the two sub-lattice indices)[18]. Under the time reversal operation, σ_x remain invariant while sin(k_x) changes its sign; hence, the above Hamiltonian explicitly breaks TRS. The Chern number of the above Hamiltonian (calculated using Eq. 1.21) as a function of μ gives

[18] σ may represent spin or sublatice, in both the cases, $\mathcal{H}_{CI}$ breaks TRS. If it represents spin, $(cos(k_x) + cos(k_y) - \mu)\,\sigma_z$ breaks TRS while if it is sub-lattice $sin(k_x)\sigma_x$ breaks TRS. We stick to the sub-lattice picture because we need spin later on for something else.

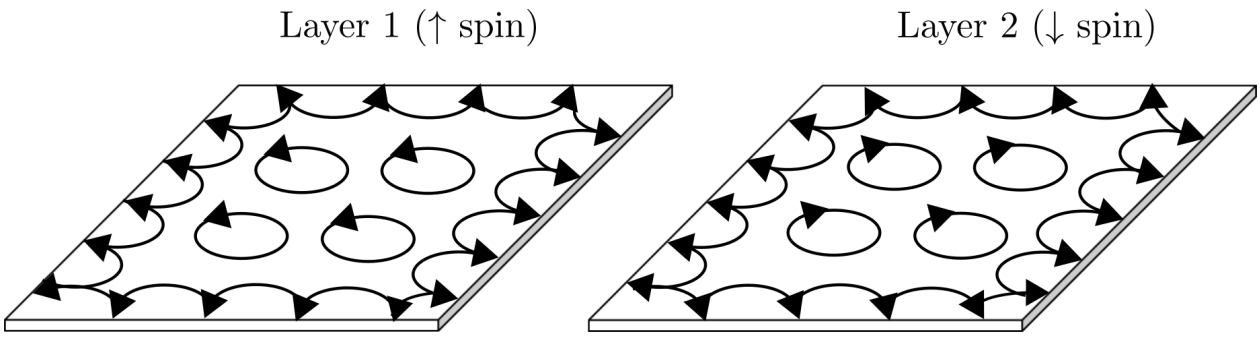

Figure 1.9: Cartoon showing the edge states in the Quantum Spin Hall system, two different states on each edge represents two different spin states of opposite chirality.

$$\begin{aligned} \nu &= -1, (0 < \mu < 2) \\ &= +1, (-2 < \mu < 0) \\ &= 0, \ otherwise. \end{aligned} \tag{1.28}$$

This example also tells us that TRS breaking is necessary but not sufficient to get non-zero Chern number ($\forall |\mu| > 2, \nu = 0$).

1.5 Quantum Spin Hall effect (QSHE)

As we have seen in the previous discussions, QHE arises because of the breaking TRS due to an externally applied magnetic field but only TRS breaking is necessary to get QHE, a magnetic field is not[14]. Now one can ask a question if we can have QHE in presence of TRS? The answer is obviously no because σ_{xy} is odd[19] under TR and hence for a TRS system, it must be zero.

In 2005, Kane and Mele[15] came up with a model with TRS which has 2 copies of TRS

[19] $\sigma_{xy} = j_x/E_y$, j_x is odd under TR while E_y is even, so σ_{xy} is odd under TR

breaking model which corresponds to two different spins. They showed that both of the copies have opposite Chern number and hence the total Chern number is zero (as expected), but the difference between the two is not zero. They called it *"Spin Chern number"*. This is the first example of Quantum Spin Hall Insulator(QSHI). Since both the copies have opposite Chern number, each edge hosts two counter propagating edge states. In contrast to the QHI, QSHI was first predicted[15] and then observed later[50, 51].

1.5.1 An example of QSHE

We can easily demonstrate the idea of Kane and Mele[15] using the CI example used in the previous section. We can make up a TRS Hamiltonian by using the simple trick, making the Hamiltonian a 4×4 matrix using two 2×2 $h(k)$:

$$\mathcal{H}_{TRS}(k) = \begin{pmatrix} h(k) & 0 \\ 0 & h^*(-k) \end{pmatrix} \tag{1.29}$$

where $h(k)$ (a 2×2 matrix) is the same as in Eq. 1.27. $h^*(-k)$ is the Hamiltonian we get upon the action of TR on $h(k)$. Since $\mathcal{H}_{TRS}$ contains both the copies ($\mathcal{T}^2 = -1$), it is invariant under TRS. Now if we calculate Chern number again using the Eq. 1.21, we will get 0 $\forall \mu$ (as expected) but we have already seen that $h(k)$ can have finite Chern number (depending on μ), so, we can define a new topological invariant called *"Spin Chern Number"* which essentially takes the difference of the Chern number of $h(k)$ and $h^*(-k)$. This will be finite for a certain range of μ ($|\mu| < 2$).

1.6 Z_2 Classification

The above description of the spin Chern number becomes inapt for those Hamiltonians where spin is not a good quantum number. Such a case often arises in the spin-orbit coupled system. In such a case a new and more generalized topological invariant was proposed by Kane and Mele[15] in 2D and Fu, Kane and Mele[17] in 3D systems. Although the complete understanding and derivation of this topological invariant is quite lengthy, some underlying concepts can be obtained with an analogy to the previous concept of QHE. In a QH insulator, the bulk topology characterized by the Chern number is equivalent to the charge polarization to the edges which is a direct consequence of *"bulk-boundary correspondence"*. In a QSH insulator, the bulk spin Chern number corresponds to spin polarization (without breaking TR symmetry) to the edges. Based on these commonalities, Kane and Mele proposed that for TR invariant systems, a mathematical quantity, namely, TR polarization is accumulated at the edge or surfaces. Such TR polarization must correspond to a topological invariant (equivalent to the Chern number) in the bulk. This topological invariant takes two values of 0 and 1 (corresponding to trivial and non-trivial topological phases). Hence this TR invariant topological invariant is often termed as a Z_2 invariant. We can define the polarization for a band state $|\psi_I(\mathbf{k})\rangle$ and its time reversal partner $|\psi_{II}(\mathbf{k})\rangle = |\mathcal{T}\psi_I(\mathbf{k})\rangle$ (where $\mathcal{T}$ is the time reversal operator ($\mathcal{T}^2 = -1$)) as

$$\begin{aligned} P_I &= i\int \langle\psi_I(\mathbf{k})|\nabla_{\mathbf{k}}|\psi_I(\mathbf{k})\rangle.d\mathbf{k} \\ P_{II} &= i\int \langle\mathcal{T}\psi_I(\mathbf{k})|\nabla_{\mathbf{k}}|\mathcal{T}\psi_I(\mathbf{k})\rangle.d\mathbf{k}. \end{aligned} \tag{1.30}$$

Now, $P = P_I - P_{II}$ is the measure of the TR polarization. After a lengthy derivation, it can be shown that this is a Z_2 invariant. It turns out that the topological invariant in case of QSHI counts the number of times a band gets exchanged with its time reversal partner in one half of the BZ. It

can formally be calculated by calculating the pfaffian[20] of the ground state and counting its zeros in the BZ.

$$\begin{aligned} I &= \frac{1}{2\pi i}\int_C d\mathbf{k}.\nabla \log(P(\mathbf{k})) \\ P(\mathbf{k}) &= Pf\left[\langle u_i(\mathbf{k})|\mathcal{T}|u_i(\mathbf{k})\rangle\right]. \end{aligned} \tag{1.31}$$

For the two bands spin full model, $\mathcal{T} = -i\sigma_y\mathcal{K}$ where $\mathcal{K}$ is the complex conjugation operator.

If the system is parity invariant, the TR polarization can be easily evaluated by calculating

$$I = \prod_{\alpha}^{\text{occupied bands}} \prod_{i=1}^{N} \delta_{i,\alpha}, \tag{1.32}$$

where δ_i's are the parity eigenvalues at the TRI k-points, α is the band index, and N is the total number of TRI k-points, N is 4 in 2D and 8 in 3D.

1.6.1 An Example of Z_2 invariant Topological Insulator

To demonstrate how a Z_2 invariant can emerge even when the spin Chern number is not defined, we consider the same model discussed before but introduce a spin flip term Δ. The requirement is that Δ has to be TRI:

$$\mathcal{H}'_{TRS}(k) = \begin{pmatrix} h(k) & \Delta \\ \Delta^\dagger & h^*(-k) \end{pmatrix}, \tag{1.33}$$

[20]The Pfaffian of a $2n \times 2n$ skew-symmetric matrix $A = [a_{ij}]$ is given by

$$Pf[A] = \frac{1}{2^n n!}\sum_{\sigma \in S_{2n}} \text{sgn}(\sigma)\prod_{i=1}^{n} a_{\sigma(2i-1),\sigma 2i}$$

where S_{2n} is the symmetric group of the dimension $(2n)!$ and $\text{sgn}(\sigma)$ is the signature of σ.

where Δ is an adiabatic term which preserves the TRS and doesn't close the gap. Here spin is no longer a good quantum number but the Z_2 invariant from Eq. 1.31 gives 1. In the above Hamiltonian, the Z_2 invariant (I) remains 1 as long as Δ doesn't close the gap for the proper choice of μ.[21]

1.7 Topological Field Theory: Chern-Simons theory

Chern-Simons theory is a field theoretic approach for studying topological phases, or more technically, it is a 3-dimensional *"topological quantum field theory"*. As shown in the previous section, the first Chern number (Eq. 1.21) (in 2+1 D) is quantized for any continuous state $|\alpha\mathbf{k}\rangle$ defined over the 2D BZ. The combination of quantum Hall current ($j_i = \sigma_H \epsilon^{ij} E_j$) and the continuity equation ($\frac{\partial \rho}{\partial t} = -\nabla.\mathbf{j}$) leads to another equation

$$\frac{\partial \rho}{\partial t} = -\nabla.\mathbf{j} = -\sigma_H \nabla \times \mathbf{E} = \sigma_H \frac{\partial \mathbf{B}}{\partial t} \tag{1.34}$$

$$\implies \rho(\mathbf{B}) - \rho(0) = \sigma_H \mathbf{B} \tag{1.35}$$

where $\rho(0)$ is the charge density in the ground state. The above equations can be combined in a covariant way as

$$j^\alpha = \frac{C_1}{2} \epsilon^{\alpha\beta\gamma} \partial_\beta A_\gamma, \tag{1.36}$$

where $\alpha, \beta, \gamma = 0, 1, 2$ are the temporal and spatial indices in 2+1 D and C_1 is an integer known as first Chern number (it is the same Chern number defined as ν_α in Eq. 1.21 and c_α in Eq. 1.16). For the external gauge field A_α, the above response can be described by the so called ~~topological~~ Chern-Simons field theory[52],

[21] the idea is to start with $\Delta = 0$ such that $\mathcal{H}'_{TRS}$ has non-trivial *Spin Chern Number* and crank up Δ such that the gap remains.

$$S_{eff} = \frac{C_1}{4\pi} \int d^2x \int dt A_\alpha \epsilon^{\alpha\beta\gamma} \partial_\beta A_\gamma, \tag{1.37}$$

from which the above responses can be recovered as $\delta S_{eff}/\delta A_\alpha = j^\alpha$. It should be noted that this topological action is gauge invariant[22], although the integrand is not.

A straight forward generalization of the above 2+1 D Chern-Simons action in 4+1 D is given by[22]

$$S_{eff} = \frac{C_2}{24\pi^2} \int d^4x dt \epsilon^{\alpha\beta\gamma\rho\tau} A_\alpha \partial_\beta A_\gamma \partial_\rho A_\tau, \tag{1.38}$$

where $\alpha, \beta, \gamma, \rho, \tau = 0, 1, 2, 3, 4$ are again temporal and spatial indices in 4+1 D and C_2 is an integer also known as second Chern number and is given by

$$\begin{aligned} C_2 &= \frac{1}{32\pi^2} \int d^4k \epsilon^{ijkl} \text{tr}[f_{ij} f_{kl}] \\ f_{ij}^{\alpha\beta} &= \partial_i a_j^{\alpha\beta} - \partial_j a_i^{\alpha\beta} + i[a_i, a_j]^{\alpha\beta}, \\ a_i^{\alpha\beta}(\mathbf{k}) &= -i\langle \alpha, \mathbf{k} | \frac{\partial}{\partial k_i} | \beta \mathbf{k} \rangle \end{aligned} \tag{1.39}$$

where $i, j, k, l = 1, 2, 3, 4$. The responses are given in a similar fashion

$$j_\alpha(\mathbf{x}) = \frac{\delta S_{eff}[\mathbf{A}]}{\delta A_\alpha(\mathbf{x})}. \tag{1.40}$$

1.7.1 Axion Angle

In a 3D topological insulator, the electromagnetic response is described by Maxwell's action

[22] this term is gauge invariant only on a closed manifold in space-time

$$S_{EM} = \frac{1}{8\pi}\int d^3x dt \left(\epsilon \mathbf{E}^2 - \frac{1}{\mu}\mathbf{B}^2\right), \tag{1.41}$$

where ϵ and μ are the dielectric constant and magnetic permeability of the material and $\mathbf{E}$ and $\mathbf{B}$ are the electromagnetic fields inside the insulator[23]. However, based on symmetry, it is also possible to write another quadratic term in the effective action

$$S_\theta = \frac{\theta}{2\pi}\frac{\alpha}{2\pi}\int d^3x dt \mathbf{E}.\mathbf{B} \tag{1.42}$$

where $\alpha = e^2/\hbar c$ is the fine structure constant and θ (axion angle) is the parameter which characterizes the topological properties and is equivalent to the Z_2 invariant in TRS systems. Under periodic boundary conditions, the Lagrangian is invariant under the shift of θ by 2π, hence θ is defined mod(2π).[24] As $\mathbf{E}.\mathbf{B}$ is odd under TR, θ can take values only 0 or π for TRS insulators to keep S_θ TR invariant.[25] It turns out that topological insulators are described by $\theta = \pi$ and get connected to $\theta = 0$ trivial insulators continuously on breaking TRS[22]. This effective action has the form which implies that an electric field can induce a magnetic polarization and vice versa.

The parameter θ depends on the band structure of the material and is given by[22]

$$\theta = \frac{1}{4\pi}\int d^3k \epsilon^{ijk} \mathrm{Tr}\left[A_i \partial_j A_k + i\frac{2}{3}A_i A_j A_k\right] \tag{1.43}$$

where A is the momentum space gauge field (Berry connection, defined earlier) of the occupied

[23] Frankly, this is the Lagrangian of EM field, it doesn't changes based on whether the system is topologically trivial or non trivial or even metal.

[24] This is the reason why θ is called as an "angle"

[25] 0 and π are equivalent to -0 and $-\pi$ respectively.

bands. It has been shown that the axionic field in a topological insulator gives rise to novel physical effects such as the anyonic statistics and image monopoles[53].

Here we end our discussion of topological bands and field theory, and in the next chapter, we will briefly discuss some of the field theoretic techniques employed in this thesis to study the interplay of interaction and topology.

2

Introduction and Overview Cont...

In the last chapter we discussed the classification of the phases based on topological invariants (non-local order), now we will discuss the classification of phases based on local order. We will start with the use of spontaneous symmetry breaking (SSB) ideas to describe phase transitions.

2.1 Spontaneous Symmetry breaking

Spontaneous symmetry breaking (SSB) is a phenomenon in which the ground state has lower symmetry than the parent Hamiltonian. Generally, such a symmetry breaking occurs upon tuning some parameter, e.g., temperature, coupling constant, interaction, etc. Spontaneous in SSB refers to the feature that the system has multiple choices for the ground state but chooses one partially based on the instantaneous preference to one of them as shown in Fig. 2.1. On breaking the symmetry, the system develops a local order parameter which is generally used to characterize the phase. Common examples of SSB is the broken U(1) gauge symmetry in superconductors,

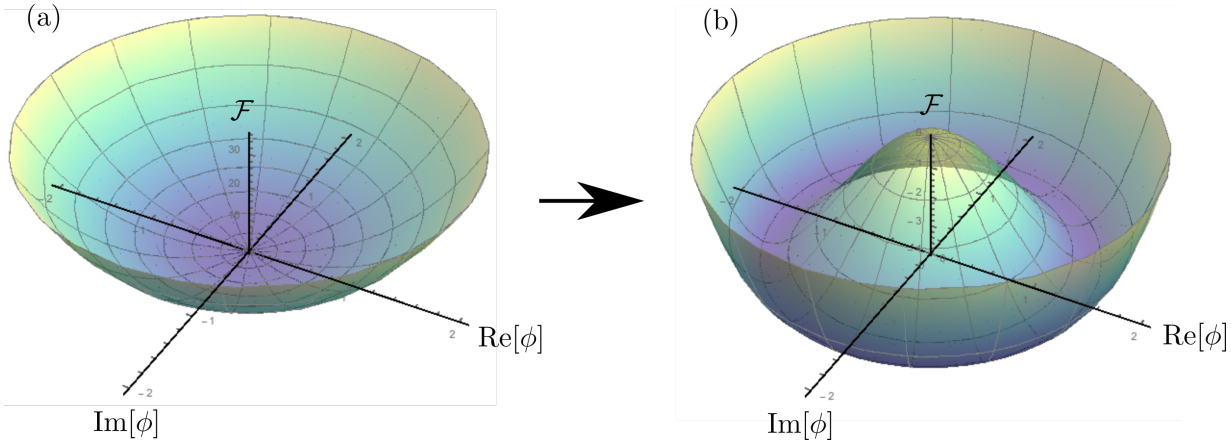

Figure 2.1: Cartoon showing the spontaneous symmetry breaking: (a) in the unbroken phase, a vanishing order parameter minimizes the free energy, (b) while in the broken symmetry phase, some finite value of the order-parameter minimizes the free energy. It should be noted that the free energy minima is not a point but a contour and hence there are an infinite number of possible ground states in the complex order parameter space.

broken spin rotation symmetry (SU(2)) in case of ferromagnet or anti-ferromagnet, discrete translation symmetry breaking in density waves, etc. In the sub-section below we will discuss different approaches to address spontaneous symmetry breaking.

2.1.1 Mean field order parameter

Order parameter, as the name suggests, is a quantity ~~(mostly physical)~~ which quantitatively captures the order in the system. It can be easily understood with the help of an example. Let's consider the attractive U Hubbard model. The interaction term is given by

$$\mathcal{H}_{int} = -U \sum_i n_{i\uparrow} n_{i\downarrow}, \quad n_{i\sigma} = c^\dagger_{i\sigma} c_{i\sigma}$$

where $U > 0$ and $c_{i\sigma}(c^\dagger_{i\sigma})$ are electronic annihilation (creation) operator. In the momentum space, it becomes[1]

$$\mathcal{H}_{int} = -U \sum_{k,k',q} c^\dagger_{k\uparrow} c^\dagger_{k'\downarrow} c_{k'+q\downarrow} c_{k-q\uparrow}. \tag{2.1}$$

Under the mean field[2] approximation, the term inside the summation breaks into[3]

$$c^\dagger_{k\uparrow} c^\dagger_{k'\downarrow} c_{k'+q\downarrow} c_{k-q\uparrow} = \langle c^\dagger_{k\uparrow} c^\dagger_{k'\downarrow}\rangle c_{k'+q\downarrow} c_{k-q\uparrow} + \langle c_{k'+q\downarrow} c_{k-q\uparrow}\rangle c^\dagger_{k\uparrow} c^\dagger_{k'\downarrow} - \langle c^\dagger_{k\uparrow} c^\dagger_{k'\downarrow}\rangle \langle c_{k'+q\downarrow} c_{k-q\uparrow}\rangle \tag{2.2}$$

where $\langle , \rangle$ represents the ensemble average and the operators have their usual meanings. At zero temperature, $\langle c^\dagger_{k\uparrow} c^\dagger_{k'\downarrow}\rangle$ acquires a finite value for $k' = -k$. As can be easily seen, this breaks the particle number conservation (U(1) gauge) symmetry[4] of the system. Given the fact that the mean-field order parameter goes into the Hamiltonian, and the expectation value of the same order parameter can itself be calculated from the ground-state of the mean-field Hamiltonian, these two are related in a self-consistent[5] way. This means one has to determine the order parameter self-consistently for each parameter choice of the Hamiltonian.

[1] Using the same transformation used before.

[2] as the name suggests, the mean field approximation neglects the effect of fluctuation and only take the average (mean) value of the operators into account. It is defined as

$$AB \overset{MF}{=} \langle A\rangle B + A\langle B\rangle - \langle A\rangle\langle B\rangle$$

[3] It should be noted that this mean field decomposition is one of the many possible decompositions as we will see in the later chapters. Generally, one of them has lower free energy than other and that decides the ground state. In the present case it is the superconducting order parameter which has the lowest free energy.

[4] It can be easily seen that this mean-field Hamiltonian doesn't remain invariant under the transformation $c_{k\sigma} \to e^{i\phi} c_{k\sigma}$. Also, the total number operator ($n = \sum_{k\sigma} n_{k\sigma}; n_{k\sigma} = c^\dagger_{k\sigma} c_{k\sigma}$) doesn't commute with the mean-field Hamiltonian and hence it is no longer a conserved quantity.

[5] Self-consistent equations are of the form $\Delta = \mathcal{F}(\Delta)$, one provides a Δ_i as an input and gets another Δ_f as the output; upon iteration, the process often converges such that the input and output are same, whence self-consistency is achieved.

2.2 Field-theoretic approach

In this section, we discuss the field-theoretic approach to phase transitions and related areas. We discuss (as an example) a continuum model with on-site attractive interaction. We start by writing the Hamiltonian as

$$\mathcal{H} = \int d^d r \left(\sum_\sigma c_\sigma^\dagger(\mathbf{r}) \frac{\hat{\mathbf{p}}^{\mathbf{2}}}{2m} c_\sigma(\mathbf{r}) - U c_\uparrow^\dagger(\mathbf{r}) c_\downarrow^\dagger(\mathbf{r}) c_\downarrow(\mathbf{r}) c_\uparrow(\mathbf{r}) \right) \tag{2.3}$$

where the operators have their usual meaning. The quantum partition function is given by

$$\mathcal{Z} = \mathrm{Tr} e^{-\beta(\hat{\mathcal{H}} - \mu \hat{N})} \tag{2.4}$$

$$= \int_{\psi(\beta)=-\psi(0)} D(\bar{\psi}, \psi) exp\left(- \int_0^\beta d\tau d^d r \left[\sum_\sigma \bar{\psi}_\sigma \left(\partial_\tau + \frac{\hat{\mathbf{p}}^2}{2m} - \mu \right) \psi_\sigma - U \bar{\psi}_\uparrow \bar{\psi}_\downarrow \psi_\downarrow \psi_\uparrow \right] \right), \tag{2.5}$$

where $\psi_\sigma(\mathbf{r}, \tau), \bar{\psi}_\sigma(\mathbf{r}, \tau)$ (we have suppressed $(\mathbf{r}, \tau)$ for brevity) denote Grassmann (anti-commuting) fields[6]. Here we can use the famous Hubbard Stratonovich[7] decoupling to reduce the quartic term in the partition function to quadratic terms at the cost of introducing new pairing fields $(\bar{\Delta}, \Delta)$ into the problem.

[6] for details regarding Grassmann variables (fields) and their algebra, readers are referred to dedicated references such as Altland and Simons [23]

[7] Hubbard-Stratonovich transformation is an exact mathematical transformation given by:

$$exp\left(-\frac{a}{2}x^2\right) = \sqrt{\frac{1}{2\pi a}} \int_{-\infty}^{\infty} exp\left[-\frac{y^2}{2a} - ixy\right] dy$$

$$e^{U\int d^d r\bar{\psi}_\uparrow\bar{\psi}_\downarrow\psi_\downarrow\psi_\uparrow} = \int D(\Delta,\bar{\Delta})exp\left(-\int d^d r\left[\frac{1}{U}|\Delta(\mathbf{r},\tau)|^2 + (\bar{\Delta}\psi_\downarrow\psi_\uparrow + \Delta\bar{\psi}_\uparrow\bar{\psi}_\downarrow)\right]\right) \quad (2.6)$$

Now the full partition function becomes

$$\begin{aligned}\mathcal{Z} &= \int D(\bar{\psi},\psi,\bar{\Delta},\Delta)\exp\left[-\int d^d r\frac{|\Delta|^2}{U}\right]\exp\left[-\int d^d r(\bar{\psi}_\uparrow,\psi_\downarrow)\mathcal{G}^{-1}(\bar{\psi}_\uparrow,\psi_\downarrow)^\dagger\right], \quad (2.7)\\ \mathcal{G}^{-1} &= \begin{bmatrix}\left[G_0^{(p)}\right]^{-1} & \Delta\\ \bar{\Delta} & \left[G_0^{(h)}\right]^{-1}\end{bmatrix},\end{aligned}$$

where $\left[G_0^{p/h}\right]^{-1} = \partial_\tau \pm \left(\frac{\hat{\mathbf{p}}^2}{2m} - \mu\right)$. Since the integral in Eq.(2.7) is quadratic in fermion fields, we can formally integrate[8] them out to get

$$\begin{aligned}\mathcal{Z} &= \int D(\bar{\Delta},\Delta)\exp\left[-\int dx\frac{1}{U}|\Delta|^2 + \ln\det\left(\mathcal{G}^{-1}\right)\right], \quad (2.8)\\ &= \int D(\bar{\Delta},\Delta)\exp\left[-\mathcal{S}\left[\bar{\Delta},\Delta\right]\right]. \quad (2.9)\end{aligned}$$

Now our partition function, $\mathcal{Z}$, is written only in terms of the integral over Hubbard-Stratonovich fields, and the free energy is given by

$$\mathcal{F} = -k_B T\ln\mathcal{Z} \quad (2.10)$$

[8] using the identity $\int D(\bar{\psi},\psi)\exp\left[-\int\bar{\psi}\hat{A}\psi\right] = \det\hat{A} = \exp\left[\ln\det\hat{A}\right]$

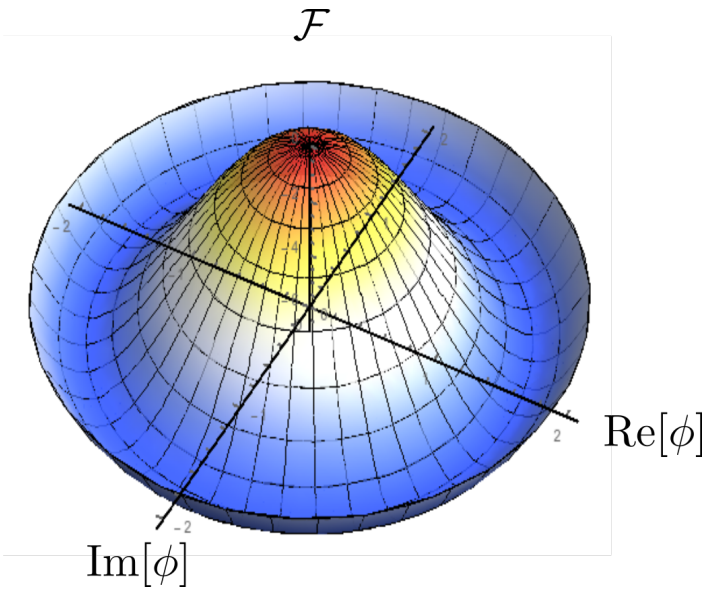

Figure 2.2: Cartoon to show the Mexican hat potential which is rotationally symmetric.

2.2.1 Saddle Point Approximation

Till now (Eq. 2.8), the theory is formally exact and no approximations have been made, but it is hard to proceed further without making any approximation. The simplest approximation involves finding the extremal pairing field, Δ_0 that minimizes $\mathcal{S}\left[\bar{\Delta}, \Delta\right]$ and then approximating the partition function as

$$\mathcal{Z} = \exp\left[-\mathcal{S}\left[\bar{\Delta}_0, \Delta_0\right]\right] \tag{2.11}$$

This saddle point approximation[9] is easily shown to be equivalent to the mean field approximation discussed in the previous section.

[9] valid only when $T \ll T_c$ (T_c is the critical temperature for the phase transition), so that the fluctuations are weak and do not contribute much.

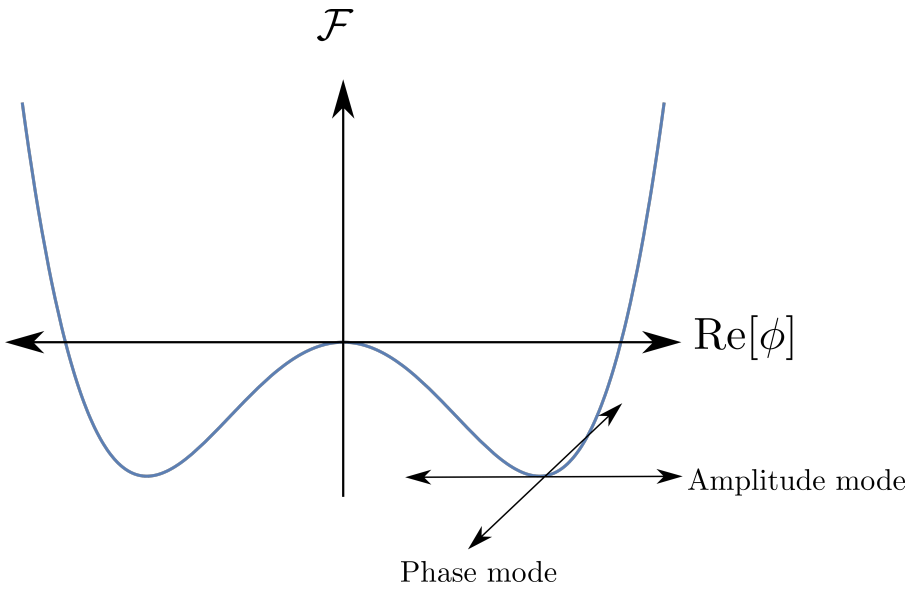

Figure 2.3: Figure showing a cut of the Mexican hat potential. Radial mode is the Higgs-mode while the angular mode is the Goldstone-mode.

2.2.2 Ginzburg-Landau theory

A slightly better way to solve the problem is to use the Ginzburg-Landau theory. Here one expands $\mathcal{G}^{-1}$ (and hence the effective action $\mathcal{S}$) in a power series in $|\Delta|$. For rotationally invariant problems, terms with odd powers of $|\Delta|$ vanish and only the term with even powers survive. Near the transition point, where Δ is small and the correlation time is large compared to β

$$\mathcal{S}[\Delta] = \int d^d r \left[b|\Delta|^2 + K|\partial\Delta|^2 + d|\Delta|^4 + \dots \right] \tag{2.12}$$

where $b = 1/2g + \Pi(0,0)/2$, $K = \lim_{q\to 0} \partial_q^2 \Pi(q,0)/2 > 0$ and $d > 0$. If one were to constrain the functional integral to the neighborhood of a specific configuration of the pairing field, then the free energy is given by

$$\begin{aligned} \mathcal{F}[\Delta] &= -k_B T \ln \mathcal{Z} = -k_B T \ln e^{-\mathcal{S}[\Delta]} \\ \mathcal{F}[\Delta] &= k_B T \mathcal{S}[\Delta] = k_B T \int d^d r \left[b|\Delta|^2 + K|\partial\Delta|^2 + d|\Delta|^4 + \dots \right] \end{aligned} \tag{2.13}$$

this is the famous Ginzburg-Landau free energy functional[10]. Let's forget about the $|\partial\Delta|^2$ term in the Eq. (2.13) for the time being. For $b > 0$ and $d > 0$, the free energy minimum lies at $\Delta = 0$ and hence the state of the system doesn't break any symmetry. When $b < 0$ while $d > 0$, the free energy minima lie at $|\Delta| = \sqrt{-b/2d}$, this leads a Mexican hat kind of free energy profile as shown in the Fig. 2.2. In a 2^{nd} order phase transition, it turns out that b goes from a positive value to a negative value as one lowers the temperature. Hence, the system breaks the symmetry upon lowering the temperature and since the order parameter developed continuously, this represents a continuous or 2^{nd} order phase transition. On the other hand, if the order parameter changes discontinuously, the transition is 1^{st} order.

2.2.3 Higgs and Goldstone modes

Since Δ is a complex field, the low energy fluctuations are of two types, amplitude fluctuations and phase fluctuations as shown in Fig. 2.3. We can calculate the mass of amplitude and phase modes by taking $\Delta = |\Delta_0 + \delta\Delta|e^{i\phi+i\delta\phi}$, where $\delta\Delta$ and $\delta\phi$ are amplitude fluctuations and phase fluctuations respectively, and substituting it into the Eq. (2.13). The coefficient of $\delta\Delta^2$ and $\delta\phi^2$ are the masses of the amplitude (Higgs) and phase (Goldstone)[11] modes. From Eq. 2.13 (ignoring the $|\partial\Delta|$ term), we get

$$\mathcal{F}[|\Delta_0 + \delta\Delta|e^{i\phi+i\delta\phi}] = b|\Delta_0 + \delta\Delta|^2 + d|\Delta_0 + \delta\Delta|^4, \tag{2.14}$$

[10] Detailed derivation is given in the Appendix B.

[11] obviously mass of the phase mode is zero, Goldstone modes are massless. We can see it explicitly by calculating the coefficient of $\delta\phi^2$

which clearly shows that free energy doesn't depend on $\partial\phi$, hence the mass associated with the Goldstone mode (phase fluctuation) is

$$M_{phase} = \left.\frac{\partial^2 \mathcal{F}}{\partial \delta\phi^2}\right|_{\delta\phi=0} = 0. \tag{2.15}$$

On the other hand,

$$M_{amp.} = \left.\frac{\partial^2 \mathcal{F}}{(\partial \delta\Delta)^2}\right|_{\delta\Delta=0} = 2b + 12d|\Delta_0|^2 \tag{2.16}$$

2.3 Brief introduction to Exact Diagonalization

In the previous two sections, we discussed a few approximations for solving interacting problems. ED is an accurate diagonalization of the Hamiltonian expressed in the entire Hilbert space of a finite-sized sample of the given system. Clearly, this is a mammoth task especially in higher dimensions as the Hilbert space dimension grows exponentially with the D^{th} power of the linear system size; but one can use the technique quite well in 1D and sometimes in 2D as well.

There are broadly two ways of doing ED. One is to calculate all the eigenvalues and eigenvectors of the Hamiltonian, and the other way is to calculate only a few of them. The former is required when we are not only interested in the low energy states but also in high energy states, for example in many body localization (MBL) problems where states of the system with a finite energy density are studied, and hence all the states are required. While the latter ED method is sufficient when we are only interested in the ground state and a few excited states. As one can expect, the former one is more costly in terms of computation compared to the latter one for given system size.

The procedure is to create a complete basis in the Hilbert space of the finite-sized system and then diagonalize the Hamiltonian in that basis based on one of the approaches discussed above.

As we are diagonalizing the full Hamiltonian which is of the dimension of the Hilbert Space, there is an upper limit (usually very small) of the system size which can be handled using ED.

- Spin S=1/2 models:40 sites square lattice, 39 sites triangular, 42 sites star lattice at S_z=0, 64 spins or more in elevated magnetization sectors, with up to 1.5 billion (=10^9) basis states with symmetries.

- t-J models: 32 sites checker board with 2 holes, 32 sites square lattice with 4 holes, with up to 2.8 billion basis states.

- Fractional quantum Hall effect: different filling fractions ν, up to 16-20 electrons, with up to 3.5 billion basis states.

- Hubbard models: 20 sites square lattice at half filling, 20 sites quantum dot structure, 22-25 sites in ultra cold atoms setting w.o. spatial symmetries, with up to 160 billion basis states.

2.4 Overview of this Thesis

The remaining thesis is divided into three main chapters and one last sixth chapter which contains the concluding discussion. In the next three chapters, we introduce three problems in the broad area of topological insulator and attempt to address them in great detail using the analytical and/or numerical techniques introduced above. Most of the questions addressed are motivated primarily by theoretical interest but many of them have connections to material realizations as well. Many of these open up ample opportunities for future work which we will briefly discuss in the last chapter. Below I outline the new results obtained in this thesis which are discussed in detail in the next three chapters.

2.4.1 Quantum Spin Hall Density Wave Insulator of Correlated Fermions

In chapter 3, we present a Z_2 type topological order parameter which is defined by spontaneous translational symmetry breaking. We start with a Rashba-type spin-orbit coupled helical band structure. We show that when the opposite chiral bands are significantly nested by a 'magic' Fermi surface nesting vector$\mathbf{Q} \sim (\pi, 0)/(0, \pi)$, the chirality between a momentum k, and that at $k + Q$ is completely reversed. This has a very intriguing consequence to the quantum and topological properties of the system. Owing to the nesting driven Fermi surface instability, a new class of quantum order parameter develops which we attribute as spin-orbit density wave. More interestingly, due to the associated chirality inversion between the main and folded bands, which manifests into chirality inversion between different lattice sites in the real space, modulated band inversion occurs. The resulting insulating phase exhibits a quantum spin-Hall (QSH) effect, with metallic Dirac excitation at the edge. Since the QSH effect is spatially modulated, and arises from spontaneous translations symmetry breaking, while time-reversal symmetry is intact, we call it a quantum spin-Hall density wave (QSHDW) state.

2.4.2 Higgs-Axion conversion and anomalous magnetic phase diagram in $TlCuCl_3$

In chapter 4, we have focused on the experimentally well-studied material $TlCuCl_3$ and asked the question: what is so special in TlCuCl3 which drives such a wide variety of unusual magnetic properties in the same crystal? We looked at this problem with a combination of quantum field theory, tight-binding model, and the DFT band structure calculations. In the DFT band structure, we are surprised to find a Dirac cone in the bulk band structure without any spin-orbit coupling or magnetism. We discover that the Dirac cone comes from a Su-Schrieffer-Heeger (SSH) like dimer Cu-chain lying in the crystal structure. The SSH model was previously studied only in a

1D polyacetylene chain in pursuit of solitons. We present $TlCuCl_3$ as the first 3D bulk crystal where such an SSH chain finds its inhabitance. The SSH chain produces a 3D Dirac cone in the non-magnetic phase. As a Heisenberg type interaction is introduced, the two Cu-sublattices of the SSH chain naturally forms a spin-singlet dimer. Such a dimerized magnetic state is very different from the typical spin-density-wave order in other monoatomic antiferromagnetic systems. Moreover, as we introduce the spin-orbit coupling (SOC), the SSH chain, dimerized spin-singlet, and the SOC are intertwined to give a topological phase transition to an axion insulator. Finally, to study the interplay between the magnetic excitations (Goldstone mode, Higgs modes, and paramagnons) and the topological axion mode, we derive the Chern-Simons-Ginsburg-Landau (CSGL) theory starting from the materials specific Hamiltonians. We showed that the topological axion term gives an additional contribution to the Higgs mass, and hence Higgs mode remains massive even at the quantum critical point, Secondly, we also showed that axion term introduces a constant to the paramagnon lifetime near the critical point, prohibiting the paramagnons to decay into the usual particle-hole continuum.

2.4.3 Bosonic Integer and Fractional Quantum Hall effect in an interacting lattice model

Finally, in chapter 5, we explore the presence of bosonic integer, as well as the fractional quantum Hall effect in an interacting lattice model. Our model is defined over bipartite honeycomb lattice with π magnetic flux per unit cell and is populated by bosons with hardcore constraint. The bosons can hop to the nearest neighbor (simple hopping) and to the next nearest neighbor (correlated hopping). We use the Lanczos algorithm (Exact Diagonalization (ED)) to find the ground state as well as a few excited states of the system with an aim to characterize the different phases of the system. We have performed calculations for two different fillings and provide evidence for the presence of the bosonic integer quantum Hall effect (BIQHE) and the bosonic

fractional quantum Hall effect (BFQHE). We also show the phase transition from the bosonic quantum Hall state to the superfluid (SF) state. We have also performed the adiabatic flux threading to confirm the quantum Hall states.

3

Quantum Spin Hall Density Wave Insulator of Correlated Fermions

3.1 Introduction

In the previous chapters, we discussed the classification of the phases of condensed matter based on the order parameter (either local, Landau Kind or non-local, Topological). In this chapter, we will show how a local order can give rise to a non-local order. In other words, how a Landau kind of symmetry breaking can lead to a topological transition in a quantum system.

~~A topological state of matter can arise when two bands with opposite chirality are inverted across the Fermi level at an odd number of TR invariant momenta (TRIM).~~ One possible route of achieving a TR invariant topological state of matter is having band inversion(s) across the Fermi level at an odd number of TR invariant momenta (TRIM).[1] The band inversion needs

[1] band inversion is the phenomena in which the concerned bands (in momentum space) changes its characteristics (such as parity, orbital weight, etc. while in the present case, chirality) rapidly with a small change in momentum.

to happen in between the bands of opposite spin state or chirality [54, 55, 56]. One of the prerequisites is thus to obtain a momentum dependence of the spin state or chirality, which is often triggered by the SOC. The inversion of the chirality between the bulk conduction and valence bands across the insulating band gap at the TRIM is protected by the TR symmetry, leading to a Z_2 TI. At the boundary, both helical states meet at the TRIM with gapless edge or surface states. Within the Dirac Hamiltonian notation, the inverted bulk band gap (denoted by $m < 0$) at the TRIM provides the negative Dirac mass, ~~while~~ with the associated gapless boundary states.

While strong quantum fluctuations or disorder are often detrimental to the band topology, they can conversely drive the inversion of the helical bands with non-trivial topological properties. These states are not always defined by a Landau order parameter, rather they are distinguished by a topological invariant of the correlated electronic bands. Examples of such states include topological Mott[57, 58], Kondo[59], and Anderson[60] insulators. Antiferromagnetic order parameter can give a distinct topological class which breaks TR and translation symmetries but preserves their combinations[61]. To date, TIs have been realized in various non-interacting systems including HgTe/CdTe[51, 50], InAs/GaSb [62] quantum wells for two-dimensional (2D) TIs, and Bi-based chalcogenides for 3D TIs[63, 64, 65, 66, 67]. SmB_6 [59, 68], and YbB_6 [69] have been extensively studied both theoretically and experimentally as potential candidates for topological Kondo insulators.

In low dimensions, due to prominent Fermi surface nesting, interaction often leads to either charge or spin density wave ground state[49, 70, 71]. In 2012, a new kind of density wave order was proposed [72, 2] which is different from both spin and charge density wave, it is spin-orbit density wave (SODW). It was experimentally confirmed in Pb nano wires[3] (Fig. 3.2). It arises in the system with strong SOC as well as interaction.

This can be easily characterized by calculating the fidelity of the band which shows a sudden dip at the band inversion point.

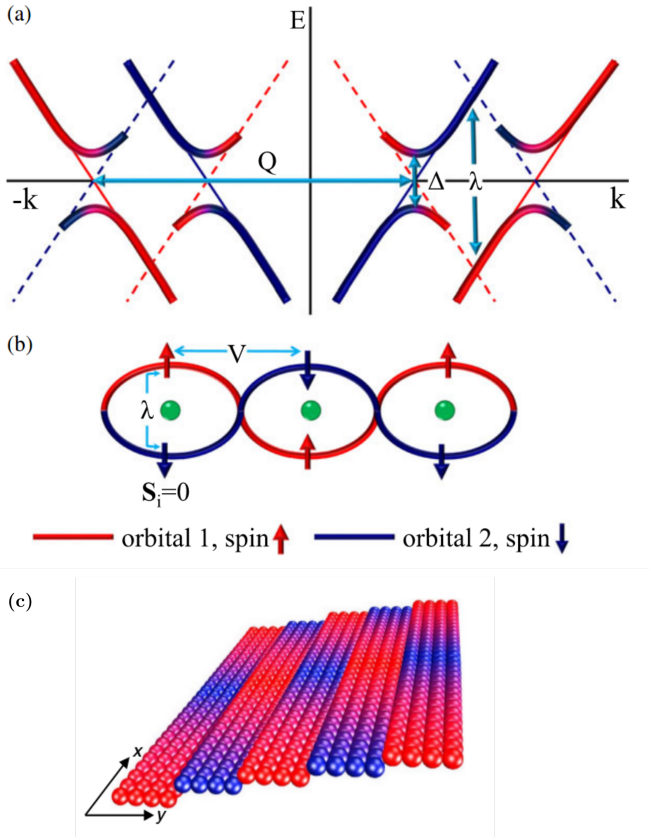

Figure 3.1: Schematic to show the SODW phase in momentum space and real space. (a) We show the two helical SOC coupled bands (thin blue and red lines, single particle) nested by **Q** (in light blue). In SODW phase (represented by thick blue-red mixed lines), helicity of the bands gets mixed because of the nesting. (b) Real space representation of the SODW phase. The SODW order parameter modulates between the nearest neighbor atomic site because of the interaction V. Figure is taken from Ref. [2]. (c) Real space representation of SODW in 2D. Blue and red color represent the helicity of the state. SODW cause the helicity modulation along the nesting direction. The figure is taken from Ref. [3]

This emergent phase of matter can be understood starting from the non-interacting SOC Hamiltonian. In 1D, the Fermi surface is just two points[2]. This leads to a logarithmic divergence in the susceptibility[49] in the particle-hole channel, which in turn tell us that the system is unstable against perturbations[3]. Now the question is, which pair of Fermi surfaces (or rather

[2]The Fermi surface has two points for a single band spin-less model and four points for single band spin-orbit coupled model.

[3]Susceptibility calculates the the response of the system under small perturbation, if the susceptibility diverges, this

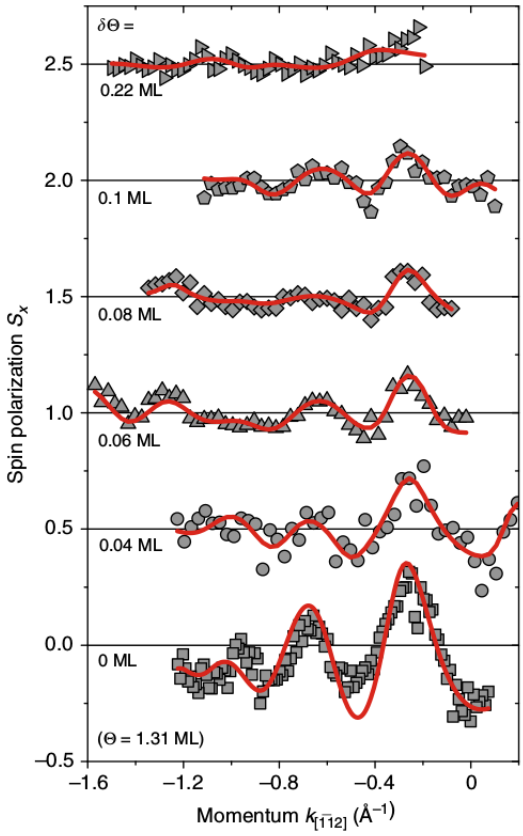

Figure 3.2: Experimental data from ARPES in Pb atomic wire showing the change in the spin polarization as a function of ML. Here ML stands for mono layer, and increasing ML causes the decrease in interaction[3]. The figure is taken from Ref. [3]

points) will get nested to give rise to a density wave like ground state. It was shown in Ref [72], that the ground state formed by the nesting of the Fermi surfaces of opposite helicity has lower free energy compared to the ones with the same helicity.[4] A schematic of the SODW phase in momentum as well as in real space is shown in Fig. 3.1. λ is the SOC gap and V is the interaction strength. This leads to a SODW gap Δ, due to the Fermi-surface nesting between the bands of opposite chirality with nesting vector Q. This exotic state of matter was experimentally

means that the system is unstable against that kind of perturbation and these perturbation will destroy the ground state of the system.

[4]The resultant order parameter looks like $\langle c^{\dagger}_{k\sigma} c_{k+Q\sigma'} \rangle$, where σ, σ' represents the spin and Q is the nesting vector.

verified in Pb atomic wire [3]. It was shown that the increase in mono layer (ML) causes a decrease in the interaction strength which eventually destroys the SODW state as shown in Fig. 3.2.

In 2D, the Fermi surface consists of two co-centric circles of different spin helicity as shown in Fig. 3.3(d). As the Fermi-surface *nesting* between the states of opposite chirality increases, depending upon the Fermi-Surface topology, it gets unstable. To get rid of this instability, a translational symmetry breaking order develops spontaneously to open up a gap in the system. This state has a density wave order of helical states and hence results in the spatial modulation of helicity depending upon the nesting wave vector $\mathbf{Q}$ as shown in Fig. 3.3(d). A real space representation of SODW state in 2D is shown in Fig. 3.1 (c). In the present work, we will discuss the similar kind of density wave in quasi 1D and show that the resultant ground state is an insulator at half filling with Z_2 topological invariant.

3.2 Proposal

We develop the theory of a Landau-type topological order parameter driven by staggered helical band inversion. The order parameter arises from the translational symmetry breaking due to Fermi surface (FS) nesting between Rashba-type SOC (RSOC) split bands. Such nesting between opposite helical states may occur in 2D systems or quantum wires of Bi, Pb, Sb, and similar elements in which both SOC and interaction are large.[73, 3] The nesting strength is enhanced with reduced system dimensionality and thickness.[73, 3] Our theory relies on a particular nesting vector $\mathbf{Q} \sim (\pi, 0)$ or $(0, \pi)$, where the helicity of the RSOC

$$\alpha_{\mathbf{k}} = \alpha_R(\sin k_y - i \sin k_x) \tag{3.1}$$

(α_R being the RSOC strength, and $k_x,\ k_y$ are the crystal momenta) is reversed to $\alpha_{\mathbf{k}+\mathbf{Q}} = \alpha^*_{\mathbf{k}}$.

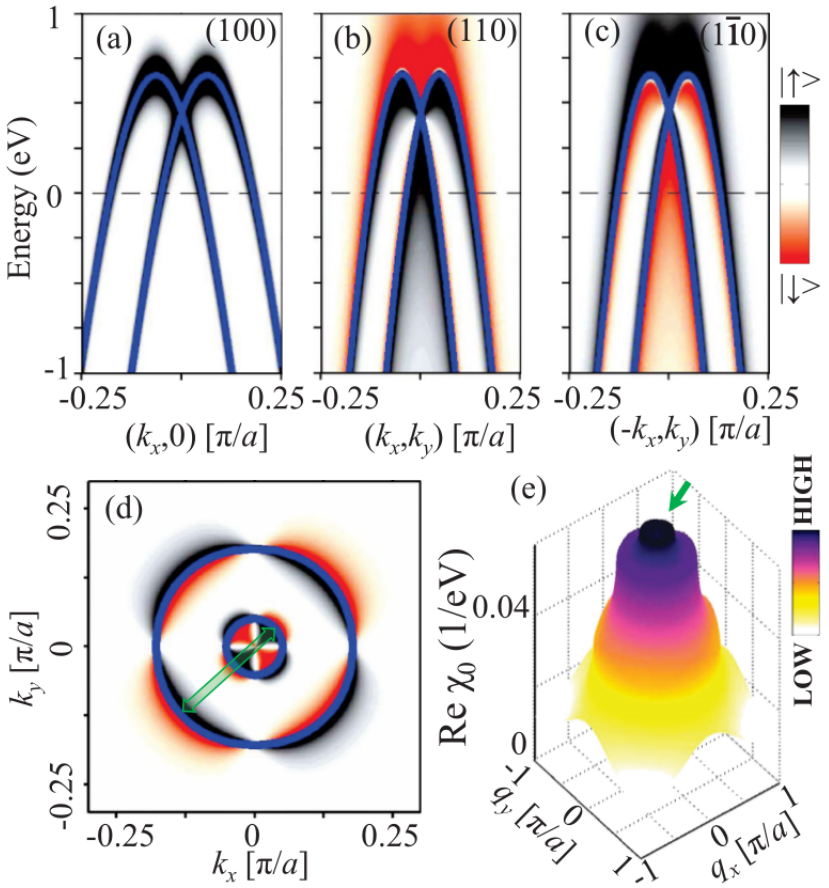

Figure 3.3: (a-c) Non interacting Rashba SOC bands along with the spin weight plotted along different directions. (d) Fermi surface of non-interacting Rashba SOC coupled bands with a *green* arrow showing the nesting vector **Q**. (e) Real part of the Lindhard susceptibility as a function of q_x and q_y showing the instability. The figure is taken from Ref. [4]

This is the key feature responsible for modulated helical band inversion. We find that as a Landau-type order parameter develops due to this FS instability, it leads to a negative Dirac mass and insulating band gap. Along the direction of the nesting, we find that correlated electronic bands are associated with non-trivial Z_2 invariant, with spin-polarized zero-energy boundary states. Such a state can be compared with a non-interacting QSH insulator in 2D, with the distinction that here every alternative atom possess opposite chirality in the same valence band, owing to translational symmetry breaking, as illustrated in Fig. 3.4(b). Thus we call it a quantum

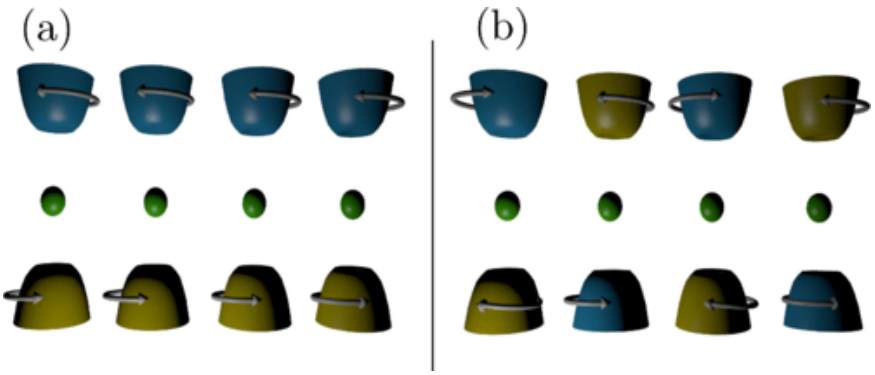

Figure 3.4: Distinction between a QSH and QSHDW insulator in real space. (a) A typical QSH insulator where all lattice sites have the same chirality in the valence band. (b) The QSHDW insulator where two sub-lattice sites have the opposite chirality in the valence band.

spin-Hall density wave (QSHDW) insulator.

3.3 Theory of QSHDW

To develop the theory of QSHDW, we use a single band tight-binding model in a 2D lattice with RSOC. The FS nesting is generally known to increase as the dimensionality is reduced. For this reason, we use anisotropic tight-binding hoppings along the x- and y-directions (t_x and t_y), so that the nesting at the wave vector $Q = (\pi, 0)$ or $(0, \pi)$ can be monitored by changing the ratio t_x/t_y. The concept and formalism of the QSHDW is general for any dimension as long as the corresponding nesting wave vector allows for the chirality inversion at all given dimensions. We use a tight-binding dispersion with nearest neighbor hopping as

$$\xi_{\mathbf{k}} = -2\left[t_x \cos(k_x a) + t_y \cos(k_y b)\right] - \xi_{\mathrm{F}}, \tag{3.2}$$

where ξ_{F} is the chemical potential, and a and b are the lattice constants along the x- and y-directions, respectively. For the RSOC $\alpha_{\mathbf{k}}$ we assume an isotropic SOC strength, α_R for

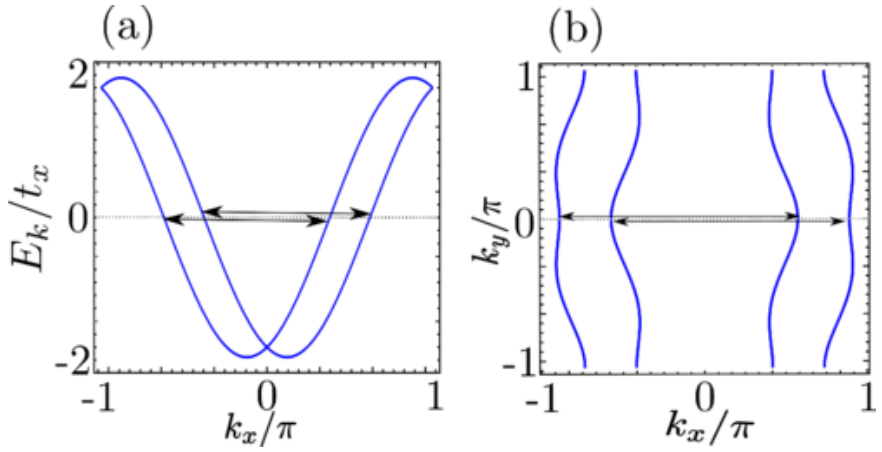

Figure 3.5: FS topology. (a) Non-interacting RSOC split bands are plotted along k_x with $k_y = 0$. Black horizontal arrows show the nesting vectors. (b) We show the nesting on the quasi-1D FS.

simplicity.

The non-interacting dispersion with RSOC is shown in Fig. 3.5(a), with two horizontal arrows dictating the $\mathbf{Q}$ nesting vectors connecting the two helical bands. For our numerical calculations, we use $t_y/t_x = 0.2$, $\xi_{\rm F} = 0$, and $\alpha_R = -1.25/t_x$, which are realistic parameters for Bi-surface state grown on Ag thin films.[72] For Bi- and Pb- atomic wires with one mono layer coverage, the intrinsic value of the FS nesting is $\sim (0.42\pi/a, 0)$[72, 73]. Starting from this band parameter, we estimate that the required chemical potential shift to obtain the $(\pi, 0)$ nesting is about 1.74 t_x, which can be achieved with chemical doping or gating or varying thickness, among others.

The interaction term responsible for the emergence of the QSHDW can be sought from on-site Hubbard, or Hund's coupling or Heisenberg interaction, as shown explicitly in the upcoming section. Here we use a generalized form as

$$H_{\rm int} = g \sum_{\substack{\mathbf{k}_1-\mathbf{k}_4, \\ \sigma_1-\sigma_4}} c^\dagger_{\mathbf{k}_1,\sigma_1} c_{\mathbf{k}_2,\sigma_2} c^\dagger_{\mathbf{k}_3,\sigma_3} c_{\mathbf{k}_4,\sigma_4}, \tag{3.3}$$

where g is the strength of the on-site interaction. $c^\dagger_{\mathbf{k},\sigma}$ ($c_{\mathbf{k},\sigma}$) is the creation (annihilation) operator for an electron with Bloch momentum $\mathbf{k}$, and spin $\sigma = \pm$.

We define a four-component Nambu-Gor'kov spinor $\Psi_{\mathbf{k}} = (c_{\mathbf{k},\uparrow}, c_{\mathbf{k},\downarrow}, c_{\mathbf{k}+\mathbf{Q},\uparrow}, c_{\mathbf{k}+\mathbf{Q},\downarrow})$. For the particular type of nesting depicted in Figs. 3.5(a-b), one singlet and two possible triplet order parameters which can develop as:

Singlet:

$$\langle O_1 \rangle = \sum_{\mathbf{k}} \langle \Psi_{\mathbf{k}} | \Gamma_1 d_{1\mathbf{k}} | \Psi_{\mathbf{k}} \rangle , \tag{3.4}$$

Triplet:

$$\langle O_2 \rangle = \sum_{\mathbf{k}} \langle \Psi_{\mathbf{k}} | \Gamma_2 d_{2\mathbf{k}} + \Gamma_3 d_{3\mathbf{k}} | \Psi_{\mathbf{k}} \rangle , \tag{3.5}$$

$$\langle O_3 \rangle = \sum_{\mathbf{k}} \langle \Psi_{\mathbf{k}} | \Gamma_4 d_{4\mathbf{k}} | \Psi_{\mathbf{k}} \rangle , \tag{3.6}$$

where the Dirac Γ-matrices have the representation

$$\Gamma_{(1,2,3,4,5,6,7)} = (\tau_y \otimes \sigma_y, \tau_x \otimes \sigma_x, \tau_x \otimes \sigma_y, \tau_x \otimes \sigma_z, \tau_z \otimes \mathbb{I}, \mathbb{I} \otimes \sigma_x, \tau_z \otimes \sigma_y) \tag{3.7}$$

in the same spinor Ψ. τ_i, and σ_i are the 2×2 Pauli matrices in the sub-lattice and spin basis, respectively, and $\mathbb{I}$ is the 2×2 identity matrix. Except for Γ_1 and Γ_5, all other Γ matrices here are odd under TR symmetry. Here, we are interested only in the TR invariant order parameters for Z_2 topological consequence. Therefore, the TR invariance of these order parameters requires that the structure factor $d_{i\mathbf{k}}$ must complement the symmetry of the corresponding Γ_i matrices under TR symmetry. Therefore $d_{1\mathbf{k}}$ for singlet state must be even under TR symmetry, while all three $d_{2,3,4}$ for the triplet states must be odd under TR symmetry. In what follows, the order parameters can be either even parity and spin singlet or odd parity and spin triplet. This is also consistent with the fermionic antisymmetric property of the order parameters.

These order parameters introduce electronic gap terms as $\Delta_i = g \langle O_i \rangle$. All order parameters govern the nontrivial topological phase as to be shown later. For the singlet case, we take

$\Delta_{1\mathbf{k}} = \Delta_{10}$ (s-wave) without losing generality. For the triplet gaps $\Delta_{2,3}$, we find through a self-consistent solution that Δ_2 has higher ~~prosperity~~ propensity to form and possesses a larger amplitude than the Δ_3 term. Henceforth, we thus consider only the Δ_2 term for the triplet case. We consider a p-wave form factor for the odd parity term as $\Delta_{2\mathbf{k}} = \Delta_{20} \sin(k_x a)$. We note that the essential topological character deduced here does not depend on the form factor, which will be clearer below. At $\mathbf{Q} = (\pi, 0)$ or $(0, \pi)$, the mean-field Hamiltonian can be fully expressed in terms of the Dirac matrices as (for singlet):

$$H_1(\mathbf{k}) = \xi^+_{\mathbf{k}} \mathrm{I}_{4\times4} + \xi^-_{\mathbf{k}} \Gamma_5 + \alpha'_{\mathbf{k}} \Gamma_6 + \alpha''_{\mathbf{k}} \Gamma_7 + \Delta_{10} \Gamma_1, \tag{3.8}$$

and eigenvalues:

$$E_{1k} = \xi^+_k \pm \sqrt{(\xi^-_k \pm |\alpha_k|)^2 + \Delta^2_{10}}, \tag{3.9}$$

and for triplet:

$$H_2(\mathbf{k}) = \xi^+_{\mathbf{k}} \mathrm{I}_{4\times4} + \xi^-_{\mathbf{k}} \Gamma_5 + \alpha'_{\mathbf{k}} \Gamma_6 + \alpha''_{\mathbf{k}} \Gamma_7 + \Delta_{2\mathbf{k}} \Gamma_2, \tag{3.10}$$

and eigenvalues:

$$E_{2k} = \xi^+_k \pm |\alpha_k| \pm \sqrt{(\xi^-_k)^2 + \Delta^2_{2,\mathbf{k}}}. \tag{3.11}$$

Here $\xi^\pm_{\mathbf{k}} = (\xi_{\mathbf{k}} \pm \xi_{\mathbf{k}+\mathbf{Q}})/2$, and $\alpha'_{\mathbf{k}}$, and $\alpha''_{\mathbf{k}}$ are the real and imaginary parts of the RSOC (α_k). In analogy with the Dirac Hamiltonian, we can easily recognize that $\xi^-_{\mathbf{k}}$ gives the Dirac mass term which controls the topological phase transition, while $\Delta_{\mathbf{k}}$ helps open the electronic gap between the opposite helical states.

3.3.1 Electronic insulator

For a pure 1D case ($t_y/t_x \to 0$), any infinitesimally small value of Δ produces an insulating band gap. As the FS warping increases with increasing t_y/t_x, some parts of the FS (which are

not nested by $\mathbf{Q}$) remain ungapped for small values of Δ (topological invariant may still be defined for the cases with small FS pockets, giving rise to QSHDW semimetals). With larger Δ, the insulating gap appears. The critical value of Δ required for the insulating state increases with increasing t_y/t_x.

In Figs. 3.6(a-b), we demonstrate the electronic dispersion for a QSHDW triplet (singlet) insulator. The vertical width of each line in Fig. 3.6(a-b) dictates the electronic weight associated with the main bands (thickness of the line corresponds to the contribution from first reduced BZ (RBZ)). As the main and shadow bands possess different spin-orbit chirality (due to $\alpha_{k+Q} = \alpha_k^*$), the emergence of QSHDW order is naturally accompanied by chirality inversion at the TRS momenta. In the present QSHDW theory, due to non-collinearity of the spins coming from the SOC, the spin expectation value of two different bands at each sub-lattice cancels each other, and no magnetic order develops in this ordered phase.

3.3.2 General Interaction Hamiltonian

$$H_{\rm int} = g \sum_{\substack{\mathbf{k}_1-\mathbf{k}_4,\\ \sigma_1-\sigma_4}} c^\dagger_{\mathbf{k}_1,\sigma_1} c_{\mathbf{k}_2,\sigma_2} c^\dagger_{\mathbf{k}_3,\sigma_3} c_{\mathbf{k}_4,\sigma_4}, \tag{3.12}$$

where g is U for Hubbard interaction, J for Heisenberg interaction and J_H for Hund's coupling. The momentum and spin conservations imply that $\mathbf{k}_1 + \mathbf{k}_3 = \mathbf{k}_2 + \mathbf{k}_4$, and $\sigma_1 + \sigma_3 = \sigma_2 + \sigma_4$, with $\sigma = \pm$. For Hubbard interaction, we obtain $\sigma_1 = \sigma_2 = -\sigma_3 = -\sigma_4$, while for Hund's coupling and Heisenberg interaction with in-plane spin, we get $\sigma_1 = -\sigma_2 = \sigma_3 = -\sigma_4$. For the non-interacting RSOC bands Fig. 2(a), the FS nesting $\mathbf{Q}$ between the two helical states further constraints the momentum, and spin indices to be $\mathbf{k}_1 = \mathbf{k}_2 = \mathbf{k}$, $\mathbf{k}_3 = \mathbf{k}_4 = \mathbf{k} + \mathbf{Q}$, and $\sigma_3 = -\sigma_2 = \sigma$, and $\sigma_1 = -\sigma_4$, and the choice between σ_1 and σ_2 is subjected to the interaction term and does not impact the result.

3.4 Topological properties

For the calculation of topological invariants in a single particle picture (also applicable to mean field electronic bands), we use the TR invariant formula discussed in Chapter 1.

In the present 1D case, the helicity or the TR polarizability is reversed along the direction of the nesting. For both singlet and triplet cases, we find that Pf[w] changes sign when going from $k_x = 0$ to $k_x = \pi$, and it vanishes at $k_x = \pi/2$, but not in the perpendicular directions. Therefore, the system possesses a strong Z_2 topological invariant ($\nu_1 = 1$) along this direction (in 1D), but a weak topological insulator in 2D with invariants (0:10). This behavior also makes our model distinct from the Kane-Mele model of the QSH insulator in graphene which is defined by Z_2 invariant (1:00). Since our model is invariant under parity, we can calculate the Z_2 invariant using the eigenvalues of the parity operator as discussed in Chapter 1. It turns out that the party eigenvalue is given by

$$\delta_{k_x,k_y} = sign(\xi_{\mathbf{k}} - \xi_{\mathbf{k+Q}}) = sign(-4t_x \cos(k_x a)) \tag{3.13}$$

which gives

$$\begin{aligned} \delta_{0,0} &= -1, \delta_{\pi,0} = 1, \delta_{\pi,\pi} = 1, \delta_{0,\pi} = -1 \\ \Longrightarrow \prod_{TRIM} &= 1 = (-1)^0 \end{aligned} \tag{3.14}$$

$$\tag{3.15}$$

while

$$\prod_{\text{along } k_x} = -1 = (-1)^1 \quad \text{and} \quad \prod_{\text{along } k_y} = 1 = (-1)^0 \tag{3.16}$$

hence, the system can be classified as a weak topological insulator in 2D with invariants (0:10).

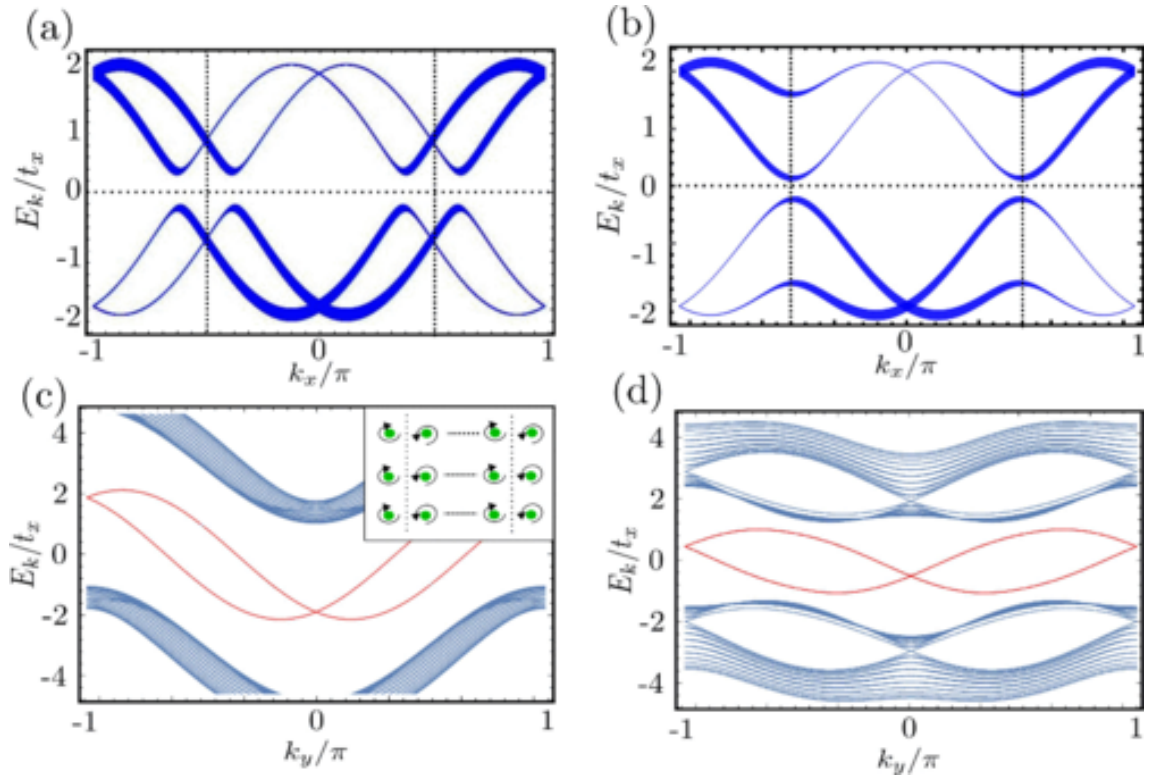

Figure 3.6: Electronic dispersion and Edge states in quasi-1D strip geometries.(a-b) We plot the Electronic band structure at k_y = 0 for singlet and triplet states, respectively. The width of each line dictates the corresponding Electronic weight in the QSHDW state. The vertical dashed lines give the RBZ boundaries.(c-d) Edge states in quasi-1D strip geometries for the singlet and triplet state, respectively. We show the spectrum of the interacting quasi-1D QSHDW in a strip geometry (inset).

3.5 Boundary state

Due to the bulk-boundary correspondence, non-trivial Z_2 invariant implies the existence of zero energy edge states as long as the TR symmetry is held. The present system resembles a Su-Schrieffer-Heeger [48] type model in 1D if we map the two atoms with opposite chirality in the larger unit cell as two sub-lattices. Therefore, the topological invariant in the bulk dictates a single end state inside the gap. The end state is localized at the two ends of the lattice in the nesting direction (here x-direction) but disperses along the y-direction. They are further split by

the RSOC.

To show the behavior of these edge states, we investigate a strip geometry, see *inset* to Fig. 3.6(d), with open boundary condition along the x-direction while keeping the periodic boundary condition along the y-direction. Splitting the corresponding (triplet) Hamiltonian into three parts as $H_{\rm strip} = H_1 + H_2 + H_{12}$, where H_1 and H_2 are the non-interacting terms in the first and second RBZ, while H_{12} is the interaction term, we get

$$\begin{aligned} H_1 &= {\sum_{k_y,j,\sigma}}' \Big[-2t_y \cos(k_y) c^\dagger_{k_y,j,\sigma} c_{k_y,j,\sigma} - t_x c^\dagger_{k_y,j,\sigma} c_{k_y,j\pm1,\sigma} \\ &\quad + \alpha_R \sin(k_y) c^\dagger_{k_y,j,\sigma} c_{k_y,j,\bar\sigma} - \lambda \frac{\alpha_R}{2} c^\dagger_{k_y,j,\sigma} c_{k_y,j+\lambda,\bar\sigma} \Big], \end{aligned} \tag{3.17}$$

$$H^s_{12} = \Delta_{10} {\sum_{k_y,j.\sigma}}' \Big[e^{iQ_x j} c^\dagger_{k_y,j,\sigma} c_{k_y,j,\bar\sigma} + e^{-iQ_x j} c^\dagger_{k_y,j,\sigma} c_{k_y,j,\bar\sigma} \Big], \tag{3.18}$$

$$\begin{aligned} H^t_{12} &= -i\Delta_{20}/2 {\sum_{k_y,j,\sigma}}' \Big[e^{-iQ_x(j+1)} c^\dagger_{k_y,j,\sigma} c_{k_y,j+1,\bar\sigma} \\ &\quad - e^{-iQ_x(j-1)} c^\dagger_{k_y,j,\sigma} c_{k_y,j-1,\bar\sigma} + \text{ h.c.} \Big]. \end{aligned} \tag{3.19}$$

Here $H_2 = H_1(\mathbf{k} \to \mathbf{k} + \mathbf{Q})$. The index $\lambda = \pm 1$ takes care of the fact that for the RSOC, the nearest neighbor (spin-flip) hopping along $\pm\mathbf{r}$ directions have opposite sign. j is the lattice site index along the x-direction, and prime over summation indicates that it is restricted within the corresponding RBZ. $H^{t/s}_{12}$ corresponds to the triplet/singlet case. Also, 1^{st} 'c' operator in $\mathrm{H}^{t/s}_{12}$ belongs to k sub lattice while 2^{nd} 'c' operator belongs to $(k+Q)$ sub-lattice. The eigenvalues of $H_{\rm strip}$ are plotted in Fig. 3.6(c-d) with $\Delta_0 = 1.48t_x (3.3t_x)$ for triplet (singlet) case. This gap value requires an interaction strength of $g \approx 3.3t_x (5.0t_x)$. It should be noted that the interaction strength chosen to show the edge state is much higher than the value required to open the insulating gap. For each 1D strip, $\nu_1 = 1$ invariant dictates zero energy end states (Zak phase). The nearest neighbor end states are coupled to each other by RSOC, and thus are split at all k_y

values except at the TR invariant points. Since the bulk system is a weak topological insulator, the boundary states are not immune to perturbations, as also evident from the presence of an even number of Dirac nodes in the BZ.

3.6 2D extension

We discuss the possibility of extending the QSHDW state to 2D systems. Here we explicitly include both nestings $Q_x = (\pi, 0)$, and $Q_y = (0, \pi)$, which makes the Hamiltonian in Eq. [3.8 & 3.10] a 6×6 one. In such a case, the topological properties become difficult to deduce analytically. Numerically, we find that Pf[w] changes sign every time while going from one TRIM point to another, in both x, and y-directions, giving rise to the weak Z_2 invariant (0:11), a 2D QSHDW insulator.

3.7 Conclusions

We presented the theory of a new state of matter, called QSHDW state, which is a spontaneous symmetry breaking quantum phase associated with a non-trivial Z_2 invariant. Designing and synthesis of quasi-2D atomic quantum wires have become a routine laboratory exercise, and it has been extensively shown that both intrinsic and extrinsic tunings of electronic properties, SOC and Coulomb interaction are very easy in such geometry.[3] In fact, the FS nesting between different helical states is observed in a number of quasi-1D,[73] and 2D systems.[74] Moreover, it is shown that the FS nesting properties, RSOC as well as the charge screening process can be monitored by varying sample thickness and substrate.[73, 74] In this connection, ferroelectric or polar substrates can also have a versatile role to enhance SOC and interaction strength.

Few remarks are in order about why the present mean-field model gives the correct result in such

quasi-1D systems. In quasi-1D systems, one may expect that a Luttinger liquid theory might be more appropriate. However, experimentally it is demonstrated that at finite temperature and in the presence of impurity scattering, the quantitative difference between the Luttinger liquid and Fermi liquid behavior is small and often undetectable.[75] Therefore, a Fermi liquid-like physics with mean-field order parameter can be used here. Moreover, in the weak coupling region, quantum fluctuations are Fermi liquid like, i.e. it scales quadratically with energy. Such weak fluctuations only become appreciable near the quantum critical regime where the gap becomes small. Away from the critical region, the QSHDW order is robust against quantum fluctuations.

1D SOC is recently observed in optical lattice, where our idea can also be explored with the existing setups. From a theoretical perspective, the generalization of the proposed topological phase to higher dimensional FS's with the same nesting condition along all directions is possible. For example, non-centrosymmetric heavy-fermion materials would be potential candidates to explore large SOC and interaction. Therefore, we envision that the emergence of QSHDW insulator may open a new area in the field of interaction-induced TIs.

4

Higgs-Axion conversion and anomalous magnetic phase diagram in $TlCuCl_3$

4.1 Introduction

In the previous chapter, we saw how a local order gives rise to a novel Z_2 topological phase. In this chapter, we reverse the order and see how an intrinsic topological order can affect the properties of local order. The main things we are concerned about is the order of phase transition, the mass of the Higgs and the Paramagnon[1] modes and their lifetime among others. The study was done mainly to explain some of the unresolved properties of a well studied (experimentally) material $TlCuCl_3$, but the results presented are quite general and are applicable to a wide range of materials.

$TlCuCl_3$ has maintained a steady theme of research interests for more than two decades due to

[1]Paramagnons are the Higgs equivalent mode in the paramagnetic phase.

its unconventional magnetic properties. This material simultaneously accommodates several unusual magnetic properties, which are either individually present in other magnetic systems, or even absent. $TlCuCl_3$ is paramagnetic at ambient condition but undergoes a quantum phase transition to an antiferromagnetic (AFM) state with small pressure[76, 5](Fig. 4.1), or with magnetic field[77, 78]. (a) The AFM phase of $TlCuCl_3$ arises from the formation of nearest neighbor quantum dimer $-$ a spin-singlet excitation often seen in spin-liquid systems, and it does not necessarily break the translational symmetry. (b) $TlCuCl_3$ is one of the earlier systems where a Higgs mode was observed in the AFM phase, in addition to the usual Goldstone modes. (c) According to basic quantum field theory, the Higgs mass disappears at the quantum critical point.[79] But in $TlCuCl_3$, one of the Higgs mode remains massive across the AFM critical point.[80](Fig. 4.2) (d) Paramagnons, gapped magnetic excitations in the non-magnetic phase, usually have a short lifetime, as they decay into the particle-hole continuum. But in $TlCuCl_3$, paramagnons have an equally large lifetime as that of the Higgs mode across the critical point.[6](Fig. 4.3) (e) In this material, Bose-Einstein condensation of magnons was experimentally achieved.[77] So, what is so special in $TlCuCl_3$ which drives such a wide variety of unusual magnetic properties in the same crystal?

Considerable experimental and theoretical studies have been devoted to understand these usual magnetic properties of $TlCuCl_3$ [81, 80, 6, 76, 5, 77, 78, 82, 83, 79, 84, 85, 86, 87, 88]. In the theoretical models, mainly the Heisenberg type spin-spin interaction is considered via various models[82, 83]. These models consistently explain the formation of spin-singlet dimers and reproduce the experimental spin-wave dispersion[76, 5, 77]. Within the so-called ϕ^4-theory, one can also obtain a characteristic scale of the Higgs mode's lifetime[82, 83, 79].

To look into these questions from a materials specific, microscopic perspective, we investigate the magnetic properties of $TlCuCl_3$ constrained by its DFT band structure. To our surprise, we find that there exists an isolated Dirac cone in the bulk band structure, even in the absence of spin-orbit coupling (SOC) and magnetism. The origin of such a Dirac cone is traced back

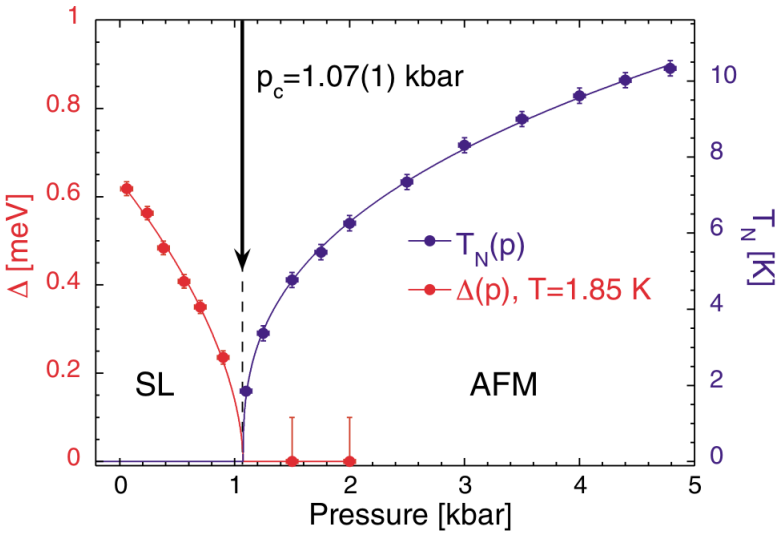

Figure 4.1: Phase diagram of $TlCuCl_3$ as a function of pressure. Below the critical pressure p_c=1.07 kbar, the system is in the spin liquid phase with the spin excitation gap $\Delta(p)$. Above the critical pressure, the system turns into an antiferromagnet with the Neel temperature $T_N(p)$. The figure is taken from the Ref. [5]

to the presence of a Cu-chain along the c-direction, which is reminiscent of the celebrated Su-Schrieffer-Heeger (SSH) chain, so far known in 1D poly-acetylene chain.[48] The SSH chain can produce a 1D Dirac-like degenerate point at $k_z = \pm\pi/c$. However, the DFT result shows a single band crossing point at $\mathbf{k} = (0, 0, \pm\pi/c)$. We develop a 3D SSH model for this system, which reproduces the anisotropic 3D Dirac cone with chiral (sublattice-momentum locking) states along the k_z-direction and helical (spin-momentum locking) state in the basal plane.

As the AFM order turns on, we find that the spin-singlet dimers are formed between the nearest neighbor Cu-sublattices of the SSH chain. This causes an inversion of the helicity between the two Cu-sublattices, driving a topologically non-trivial phase, as distinguished by a finite axion-angle (θ) within the Chern-Simon theory. The interplay between the topological excitations (axions) and magnetic excitations (Goldstone, Higgs, paramagnons modes) is studied here within a microscopically derived Chern-Simons-Ginzburg-Landau (CSGL) model. We find that the CS

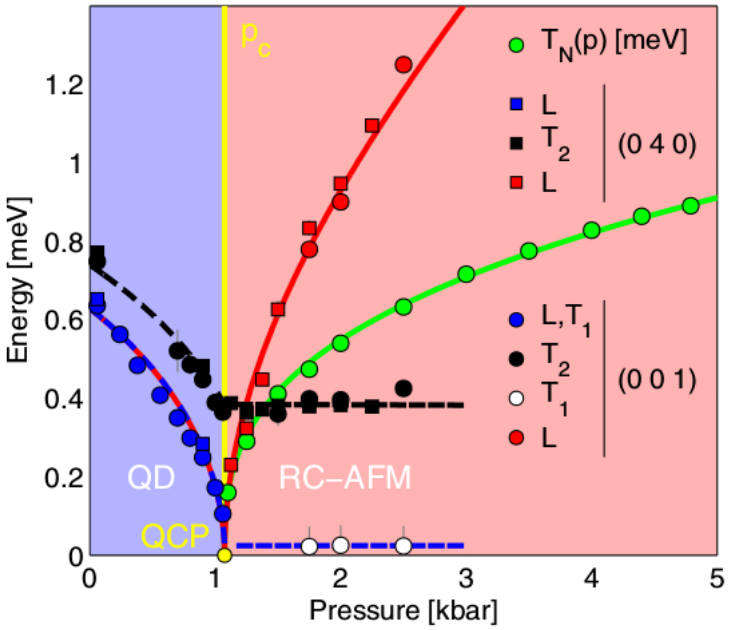

Figure 4.2: Gap of all the three triplet excitation measured using inelastic neutron scattering (INS) as a function of pressure at 1.85 K temperature. The figure is taken from the Ref. [5]

term characteristically modifies the magnetic phase transition. In addition, the axion term gives a new contribution to the Higgs mass term which is independent of the magnetic order parameter, and hence Higgs mode remains massless across the AFM critical point. This explains why the Higgs modes remain indifferent to the magnetic critical point, and the Higgs-paramagnon conversion becomes independent of the magnetic order parameter.

4.2 DFT Results

$TlCuCl_3$ crystallizes in the monoclinic $P2_1/c$ space group, with 4 formula units per unit cell. We use the experimental lattice constants of a = 14.144 Å, b = 8.890 Å, and c = 3.983 Å, and α = 96.32°. The top view in Fig. 4.4(a) shows a rectangular projection of the unit cell on the $a-b$ plane. Each formula unit contains two inequivalent SSH chains along the c-axis as shown in

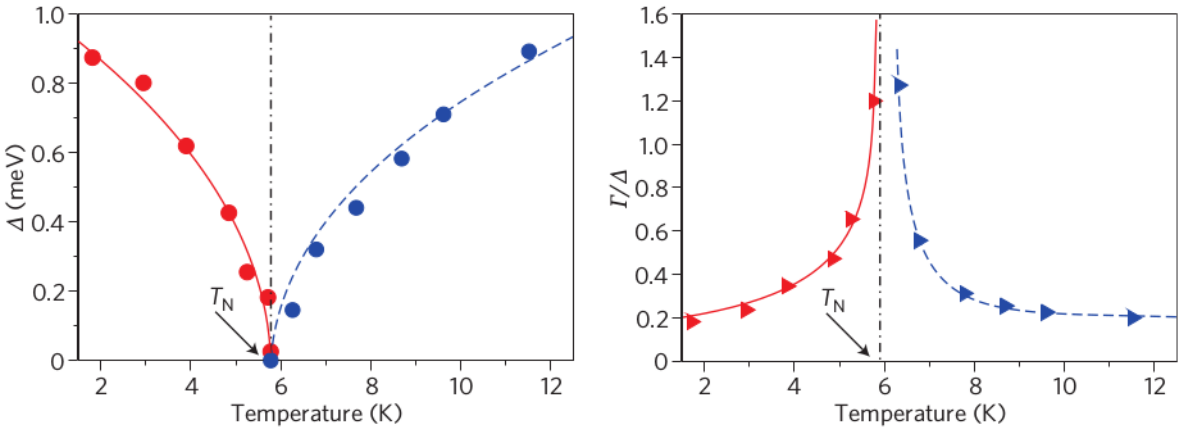

Figure 4.3: Magnon and paramagnon energies as a function of temperature (a) Energy gap of magnon as a function of temperature at 1.75kbar pressure. Red dots show the Higgs magnon-gap below the Neel temperature (T_N) while the blue dots represents paramagnon gap for the temperature above Neel Temperature. (b) The ratio of magnon lifetime (Γ) to the magnon gap (Δ) as a function of temperature. Red triangle corresponds to the Higgs magnon below the Neel temperature while the blue triangles correspond to the paramagnon modes above the Neel temperature. The figure is taken from Ref. [6]

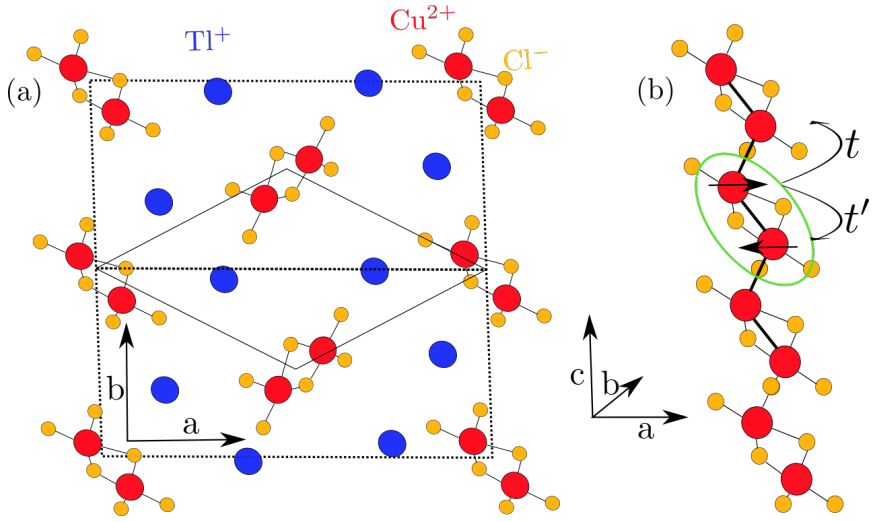

Figure 4.4: Top (a) and side (b) views of $TlCuCl_3$ unit cell. Each unit cell contains two SSH chain of Cu-atoms (red symbols), which are mutually rotated by 90^o. (b) Shown a single SSH chain, with in-plane spin-polarization in the AFM phase.

Fig. 4.4(b), at the center and corners of the rectangle. Because of different Cl-environments, the

two nearest neighbor hoppings between Cu-Cu atoms become slightly different resulting in an SSH structure.

We compute the DFT band structure using the Local Density Approximation (LDA) exchange-correlation as implemented in the Vienna ab-initio simulation package (VASP)[89, 90]. LDA+U (U = 4 eV) method is used to deal with the strong correlation features on Cu-3d orbitals. The non-magnetic DFT band structure in Fig. 4.6(a) shows four bands near the Fermi level (E_F), stemming from the d-orbitals of the Cu-atoms. Each SSH chain is individually responsible for forming a 1D Dirac cone at the $k_z = \pm\pi/c$-point. The inter-chain hopping breaks the degeneracy of the bands, resulting in two gapped bands, and one single Dirac cone. The Dirac cone formation in the non-magnetic state is robust to various values of U and DFT functionals. While the band degeneracy $k_z = \pm\pi/c$ is guaranteed by the chiral symmetry of the SSH chain, in the absence of SOC, there is no reason that the two sub-lattice bands must also be degenerate only at $k_x = k_y = 0$. However, thanks to the crystal symmetry and the crystal field splitting, $TlCuCl_3$ obtains a unique combination of the hopping integrals such that the bands are non-degenerate at every other $\mathbf{k}$-points, except at $\mathbf{k}^* = (0, 0, \pi/c)$. Our DFT band structure agrees well with a previous LMTO calculation[91], and is also reproducible with other DFT functionals.

4.2.1 DFT calculation W/ SOC

We again compute the DFT band structure using the Local Density Approximation (LDA) exchange-correlation as implemented in the Vienna ab-initio simulation package (VASP)[89]. The results remain characteristically the same for the GGA and other functionals. The DFT band structure also agrees well with a previous LMTO calculation. In our LDA+U calculation, the electronic wave function is expanded using plane wave up to a cutoff energy of 500 eV. Brillouin zone sampling is done by using a $(8 \times 8 \times 8)$ Monkhorst-Pack k-grid. Projected augmented-wave (PAW) pseudo-potentials are used to describe the core electron in the calculation[90].

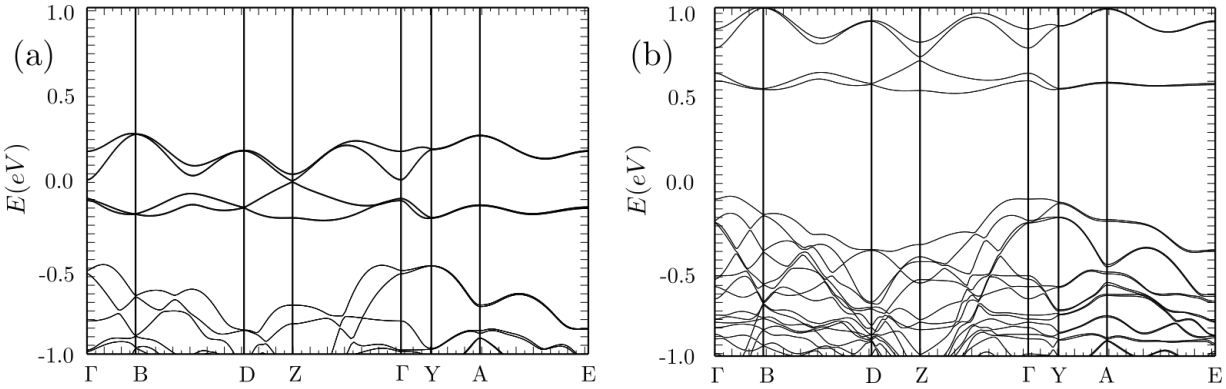

Figure 4.5: Computed *ab-inito* band structure of $TlCuCl_3$ in the presence of spin-orbit coupling (a) with magnetism and (b) without magnetism.

We found in the DFT band structure that the magnetic gap ($\Delta \sim 1.3$ eV) is larger than the crystal field splitting (CFS) (Fig. 4.5),[2] and thus one obtains a band insulating behavior in the electronic properties. As one approaches the magnetic critical point, the magnetic gap takes over for $\Delta < \Delta_{\mathrm{CFS}}$.

4.3 Tight-binding model

Our main interest is to study the topological properties arising from the bulk Dirac cone. Since there is only one band crossing in the bulk state at E_F, the minimal model required to capture the essential topological properties is a two-band model forming the Dirac cone. We, therefore, start with a two-band tight-binding model, coming from the Cu-sublattices in a given SSH chain, and allow inter-chain hoppings in all three dimensions. We may refer to the corresponding model as a 3D SSH model.

In what follows, we work in a single Cu-chain per conventional unit cell, as indicated in

[2]We again compute the DFT band structure using the Local Density Approximation (LDA) exchange correlation as implemented in the Vienna ab-initio simulation package (VASP)[89, 90]. LDA+U (U = 4 eV) method is used to deal with the strong correlation features on Cu-3d orbitals and the spins were allowed to align anti-ferromagnetically.

Fig. 4.4(a). We express the corresponding Hamiltonian in a 2-component spinor as $\Psi(\mathbf{k}) = (\psi_{\rm A}(\mathbf{k}), \psi_{\rm B}(\mathbf{k}))^T$, where 'A', and 'B' stand for two Cu-atoms, as

$$H_0 = \sum_{\mathbf{k}, ij\in({\rm A,B})} \Big[\xi^{ij}_{\mathbf{k}} \psi^\dagger_i(\mathbf{k})\psi_j(\mathbf{k}) - \mu\psi^\dagger_i(\mathbf{k})\psi_i(\mathbf{k})\Big]. \tag{4.1}$$

Here $\xi^{\rm AA}_{\mathbf{k}} = \xi^{\rm BB}_{\mathbf{k}}$, and $\xi^{\rm AB}_{\mathbf{k}}$ are the intra-, and inter-sublattice dispersions, respectively.

4.3.1 SSH term

The expression for SSH like term in our 3D model looks like

$$\begin{aligned} H_{AA} &= C_{10}\cos((k_x+k_z)/2) + C_{11}\cos(k_y) + C_{12}\cos((k_x-k_z)/2) + C_{13}\cos(2k_y) \\ &\quad + C_{14}\cos(k_x) + C_{15}\cos(k_z) + C_{16}\cos(k_x+k_z) + C_{17}\cos(k_x-k_z) + C_{18} \end{aligned} \tag{4.2}$$

$$\begin{aligned} H_{AB} &= e^{ik_z/2}\left(C_0 + C_1 e^{-ik_z} + \left(C_2 + C_3 e^{-ik_z}\right)\left(C_4 e^{i(k_x+k_y)/2} + C_5 e^{-i(k_x+k_y)/2}\right)\right. \\ &\quad \left. + \left(C_6 + C_7 e^{-ik_z}\right)\left(C_8 e^{i(k_x-k_y)/2} + C_9 e^{-i(k_x-k_y)/2}\right)\right) \end{aligned} \tag{4.3}$$

where C's are the TB parameters. The above equation for inter-sublattice hopping can be rewritten in the form,

$$H_{AB} = e^{ik_z/2} T_{\mathbf{k}\perp}\left(1 + \frac{T'_{\mathbf{k}\perp}}{T_{\mathbf{k}\perp}} e^{ik_z}\right) \tag{4.4}$$

where

$$\begin{aligned} T_{\mathbf{k}\perp} &= C_0 + C_2C_4 e^{i(k_x+k_y)/2} + C_2C_5 e^{-i(k_x+k_y)/2} + C_6C_8 e^{i(k_x-k_y)/2} + C_6C_9 e^{-i(k_x-k_y)/2} \\ T'_{\mathbf{k}\perp} &= C_1 + C_3C_4 e^{i(k_x+k_y)/2} + C_3C_5 e^{-i(k_x+k_y)/2} + C_7C_8 e^{i(k_x-k_y)/2} + C_7C_9 e^{-i(k_x-k_y)/2} \end{aligned} \tag{4.5}$$

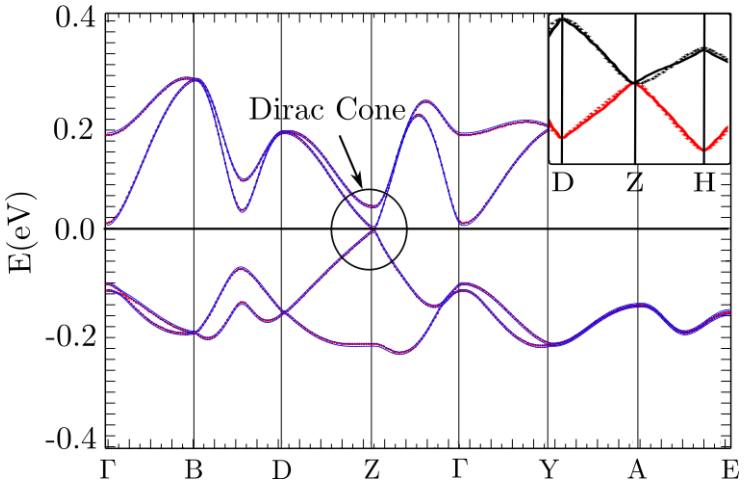

Figure 4.6: DFT band structure of $TlCuCl_3$, plotted along $\Gamma(0,0,0), B(0,\pi,0), D(0,\pi,\pi), Z(0,0,\pi), Y(-\pi,0,0), A(-\pi,\pi,0), E(-\pi,\pi,\pi)$. Blue and red colors depict the bands without and with SOC respectively. Since SOC is of the order of 5 meV, the band splitting is not visible in this energy scale. *Inset:* Fittings of the 2D SSH model near the Dirac cone.

The TB parameters are C_{0-18} = [0.156, 0.209, -0.076, 0.223, -0.135, -0.325, 1.466, -0.019, -0.030, 0.045, 0.002, -0.033, -0.003, 0.027, -0.002, 0.095, -0.105, -0.019] in eV.

The energy eigenvalues of the Hamiltonian in Eq. 4.1 are $E^{\pm}_{\mathbf{k}} = \xi^{\rm AA}_{\mathbf{k}} \pm |\xi^{\rm AB}_{\mathbf{k}}|$. The two bands meet at the locii of $|\xi^{\rm AB}_{\mathbf{k}}| = 0$, while $\xi^{\rm AA}_{\mathbf{k}}$ gives an overall shift of the degenerate points in energy. In the case of an isolated 1D SSH chain, $\xi^{\rm AB}_{k_z}$ is often described by $\xi^{\rm AB}_{k_z} \rightarrow \left(t + t' e^{-ik_z}\right)$ (we set $a = b = c = 1$ for simplicity), where t, and t' are the inter-sublattice hoppings along the $\pm z$-direction, respectively [see Fig. 4.4(b)]. A Dirac cone forms at $k_z = \pm\pi$ when $t' = t$. In the same spirit, we can cast the Hamiltonian in Eq. 4.1 into a 3D SSH model as

$$\xi^{\rm AB}_{\mathbf{k}} \;=\; T_{\mathbf{k}_\perp} + T'_{\mathbf{k}_\perp} e^{-ik_z}, \tag{4.6}$$

where $\mathbf{k}_\perp = (k_x, k_y)$. $T'_{\mathbf{k}_\perp}$, and $T_{\mathbf{k}_\perp}$ have the same meanings as t', and t defined above, but due to inter-SSH chain hoppings, they acquire in-plane dispersions. $\xi^{\rm AA}_{\mathbf{k}}$, $T_{\mathbf{k}_\perp}$, and $T'_{\mathbf{k}_\perp}$ are expressed

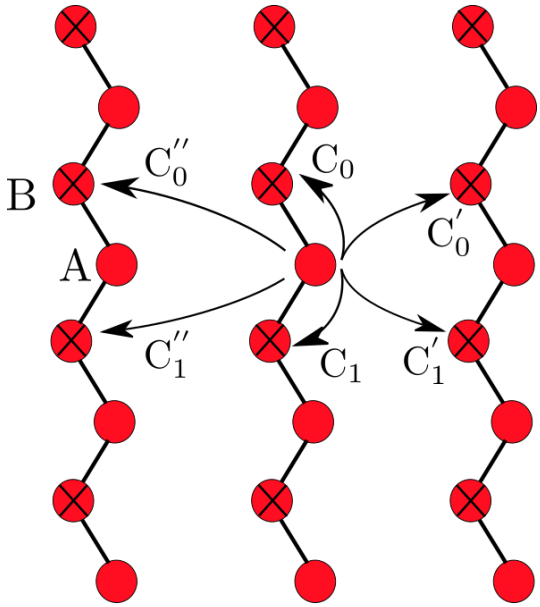

Figure 4.7: Figure showing effective hopping in (x+y,z) plane. Here C_0', C_0'', C_1' and C_1'' correspond to C_2C_4, C_2C_5, C_3C_4 and C_3C_6 respectively. We have similar kind of hopping term in (x-y,z) plane as well.

in terms of the Slater-Koster tight-binding (TB) hopping integrals between intra-, and inter-chain hoppings.

Following the DFT result, we fit the TB dispersions to the DFT band with the constraint that $T'_{\mathbf{k}^*} = T_{\mathbf{k}^*}$ only at $\mathbf{k}^* = (0, 0, \pi)$. Hence we reproduce a 3D Dirac cone, with linear dispersion in q_z, and quadratic dispersion in (q_x, q_y), where $\mathbf{q} = \mathbf{k}^* - \mathbf{k}$ and $\mathbf{q} << 1$ (see *inset* to Fig. 4.6).

4.3.2 Spin-Orbit coupling (SOC)

Although SOC is weak here, however, it is sufficient to introduce a chirality in the very low energy spectrum across $\mathbf{k}^*$. Due to anisotropy between the ab-plane and the c-axis, we can

conveniently split the SOC Hamiltonian into in-plane and out-of-plane, as

$$H_{\rm SO} = \sum_{i,j\in(A,B)}\sum_{\mathbf{k},ss'}\Big[\psi^{\dagger}_{i,s}(\mathbf{k})\left(\boldsymbol{\alpha}^{ij}_{\mathbf{k}}\times\boldsymbol{\sigma}_{ss'}\right)\psi_{j,s'}(\mathbf{k}) + \psi^{\dagger}_{i,s}(\mathbf{k})\left(\boldsymbol{\beta}^{ij}_{\mathbf{k}}\cdot\sigma^{z}_{ss'}\right)\psi_{j,s'}(\mathbf{k})\Big]. \tag{4.7}$$

In the first term, the in-plane spin is locked to its transverse velocity matrix $\boldsymbol{\alpha}^{ij}_{\mathbf{k}}$, while the out-of-plane spin is locked to the longitudinal one $\boldsymbol{\beta}^{ij}_{\mathbf{k}}$. The components of the velocity operators are

$$\boldsymbol{\alpha}^{ij}_{\mathbf{k}} = \alpha^{ij}_{0}\left(-\frac{\partial\xi^{ij}_{\mathbf{k}}}{\partial k_y},\frac{\partial\xi^{ij}_{\mathbf{k}}}{\partial k_x},0\right),\ \boldsymbol{\beta}^{ij}_{\mathbf{k}}=\beta^{ij}_{0}\left(0,0,\frac{\partial\xi^{ij}_{\mathbf{k}}}{\partial k_z}\right). \tag{4.8}$$

α^{ij}_{0}, and β^{ij}_{0} are the corresponding SOC strengths. Eq. 4.7 allows several SOC terms, however, fitting to DFT results indicate that $\beta^{ij}_{0}\to 0$, implying that the spins are aligned perpendicular to the SSH chain. $\alpha^{\rm AA}_{0}$ is the second nearest neighbor SOC term and is negligibly small, while $\alpha^{\rm AA}_{0}=0.05$ eV.

4.3.3 Dirac Hamiltonian

Combining Eqs. 4.1, and 4.7, the full non-magnetic Hamiltonian can be expressed in terms of a spinor $\Psi(\mathbf{k})=(\psi_{\rm A\uparrow},\psi_{\rm B\uparrow},\psi_{\rm A\downarrow},\psi_{\rm B\downarrow})^{T}$ as:

$$H(\mathbf{k})=\xi^{\rm AA}_{\mathbf{k}}\mathbf{1}_{4\times4}+\sum_{i=1}^{5}d_i(\mathbf{k})\Gamma_i. \tag{4.9}$$

where $\Gamma=(\sigma_x\otimes\mathbf{1},\sigma_y\otimes\mathbf{1},\mathbf{1}_{2\times2}\otimes\tau_x,\mathbf{1}_{2\times2}\otimes\tau_y,\sigma_z\otimes\tau_z)$, where σ, and τ are the Pauli matrices in the spin and sub-lattice basis, respectively. The components of the d-vectors are $\mathbf{d}$ = ($\alpha^{\prime\rm AA}_{x}$,$-\alpha^{\prime\prime\rm AA}_{y}$,$\xi^{\prime\rm AB}$, $\xi^{\prime\prime\rm AB}$,0). The Hamiltonian is invariant under time-reversal symmetry and parity operation. The parity operation constitutes of $\mathbf{k}\leftrightarrow-\mathbf{k}$, and A$\leftrightarrow$B.

4.3.4 AFM calculations

Next, we have performed non-collinear, spin-polarized DFT calculations with and without the SOC. We find an AFM ground state with antiparallel spin between 'A' and 'B' sub-lattices of the SSH chain[3]. We find that the spins are quantized in the ab plane, as seen in experiment[6, 76, 5, 77], and the easy axis is almost along the diagonal direction in this plane. The DFT predicted magnetic moment along the z-direction is negligibly small, and that in the ab-plane are $m_{\mathrm{A,B}} = \pm 0.43$ for the two Cu atoms, respectively. The magnetic band structure shows insulating behavior with a band gap of $\sim$ 1.3 eV.[4] From the band gap and magnetic moment, we estimate the AFM coupling to be around $J \sim$ 1.5 eV, which is close to the value estimated in neutron scattering measurement.[92, 93]

Since the magnetic moment is small, we can treat the magnetic ground state within a mean-field order approximation. We start with the nearest neighbor spin interaction term $H_{\mathrm{I}} = J \sum_{\langle i,j \rangle \in (\mathrm{A,B})} \mathbf{S}_i.\mathbf{S}_j$, where $\mathbf{S}_i$ is the spin operator. Guided by the DFT results, we consider only the spin-spin interaction along the spin-quantization axis, and between the nearest 'A' and 'B' sub lattices only. The AFM order parameter is defined as $\phi = (m_{\mathrm{A}} - m_{\mathrm{B}})/2$, where the magnetization is $m_{\mathrm{A/B}} = \langle S^{\mathrm{z}}_{\mathrm{A/B}} \rangle$. The excitation energy gap in the band structure is $\Delta = J\phi$. Such an order parameter have been used earlier in $TlCuCl_3$ and is found via self-consistent calculation to define the AFM ground state.[88] Using Hubbard-Stratonovic decomposition of

[3] In the DFT calculation, we used experimental lattice constant which produces a small pressure 0.5 GPa in the unit cell, and thus it mimics the experimental condition of pressure tunned AFM transition.

[4] The magnetic state represents a non-trivial topological axion insulator in the small magnetic moment region near the critical point. However, owing to the loss of time-reversal symmetry, the surface state does not host any gapless state. We do not expect to observe any edge state in the DFT calculation.

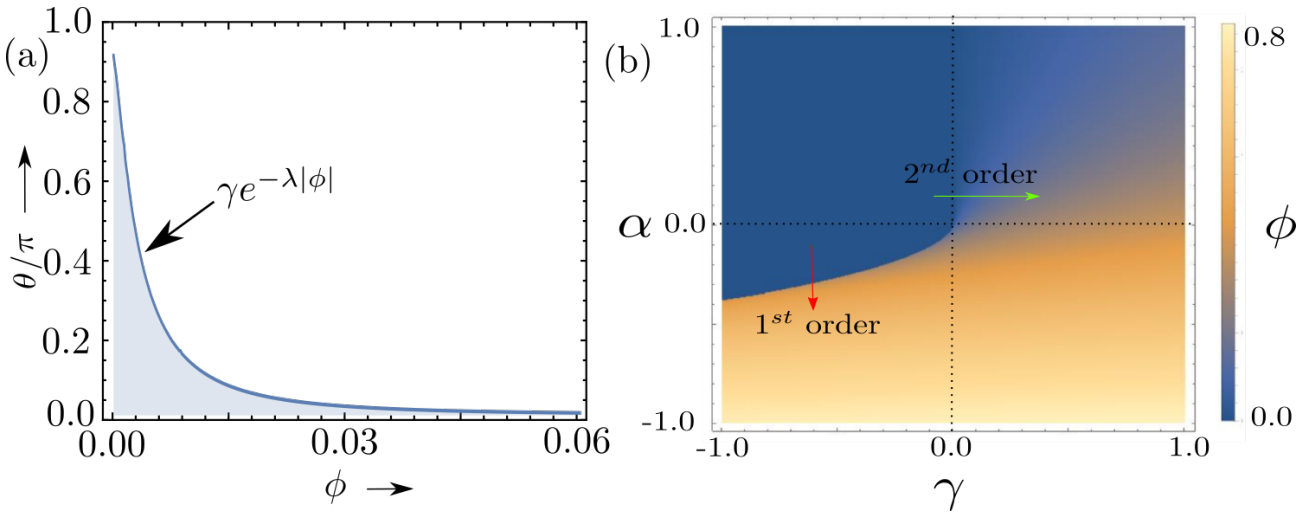

Figure 4.8: (a) Computed values of the axion angle θ as a function of the magnetic order parameter ϕ. (b) The color plot depicts values of magnetization as a function of the GL coefficient α, and the CS coefficient γ from Eq. 9. We set $\beta > 0$. Horizontal arrow (green) indicates a second order phase transition line where the order parameter decreases continuously, while the vertical arrow dictates the first-order line.

the $H_{\rm I}$, we obtain the magnetic perturbation

$$H_{\rm I} \approx J \sum_{\langle i,j\rangle\in({\rm A,B})} (\langle \mathbf{S}_i\rangle.\mathbf{S}_j + \mathbf{S}_i.\langle \mathbf{S}_j\rangle - \langle \mathbf{S}_i\rangle.\langle \mathbf{S}_j\rangle) \tag{4.10}$$

$$\approx J \sum_{\langle i,j\rangle\in({\rm A,B})} \left(m_A S_j^z + m_B S_i^z - m_A m_B\right) \tag{4.11}$$

assuming $m_B = -m_A$ for the anti-ferromagnetic case and dropping $m_A m_B$ in the above equation, we get

$$H_{\rm I} \approx J \sum_{\langle i,j\rangle\in({\rm A,B})} \phi \left(S_j^z - S_i^z\right) \tag{4.12}$$

which, in momentum space becomes

$$H_{\rm I}(k) \approx J\phi\Gamma_5 = d_5\Gamma_5. \tag{4.13}$$

4.3.5 Helicity inversion and topological axion insulator

The AFM order introduces a crucial change in the SOC Hamiltonian in Eq. (4.7). Since the spin polarization is fully reversed between the 'A' and 'B' sub-lattices, the corresponding SOC is also reversed, i.e., $\alpha_{\mathbf{k}}^{\mathrm{AA}} = -\alpha_{\mathbf{k}}^{\mathrm{BB}}$. This induces an inversion in the helicity between the 'A' and 'B' sub-lattices, i.e., if the up spin is right moving in the 'A' sub-lattice, it becomes left moving in the 'B' sub-lattice, and vice versa. This helicity inversion endows the system to acquire a non-trivial topological phase.[94, 72, 54] Within the above Hamiltonian we incorporate the helicity inversion by changing $\Gamma_{1,2} \to \sigma_x \otimes \tau_z, \sigma_y \otimes \tau_z$.

The topological invariant of the 3D AFM insulator cannot be defined by the usual $\mathbb{Z}_2$ invariant or Chern number, but by an 'axion' invariant θ[95, 96, 97, 98]. The axion invariant (θ) is precisely the $\mathbb{Z}_2$ invariant (multiplied by π) for a time-reversal invariant system and vanishes continuously as the magnetization increases spontaneously[96, 97, 99]. The axion invariant is the solid angle enclosed in the d-space as one encircles the entire 3D Brillouin zone.[99, 98] Reminiscence to the topological phase transition in a single SSH chain, we also find here that θ becomes finite when the zeros of $d_3(\mathbf{k}) = \xi_{\mathbf{k}}^{\prime\mathrm{AB}}$ lies inside the solid angle, giving the condition that $T_{\mathbf{k}_\perp} \leq T'_{\mathbf{k}_\perp}$, for $\mathbf{k} \in \mathrm{BZ}$. Having a Dirac cone in the SOC band structure, we ensure that such a condition is automatically satisfied in the non-interacting phase. For $\phi \to 0$, we obtain $\theta = \pi$.

For finite $|\phi| > 0$, we numerically find that θ decreases exponentially as shown in Fig. 4.8a, using the formula[99]

$$\theta = \int_{\mathrm{BZ}} \frac{d^3k}{4\pi} \frac{2|d| + d_4}{(|d| + d_4)^2 |d|^3} \epsilon^{ijkl} d_i \partial_{k_x} d_j \partial_{k_y} d_k \partial_{k_z} d_l. \tag{4.14}$$

as

$$\theta = \pi e^{-\lambda|\phi|}, \tag{4.15}$$

where $\lambda \propto J$, is a fitting parameter, obtained to be λ =220. Owing to time-reversal symmetry breaking, the corresponding topological axion phase does not exhibit any gapless edge state.[5]

4.4 Chern-Simons-Ginzburg-Landau analysis

Finally, we discuss the implications of the topological excitations to the magnetic properties. The topology induced axion excitations are described by a Chern-Simons (CS) term in the effective Lagrangian.[95, 96, 97] On the other hand, the interaction induced magnetic excitations are captured within the Ginzburg-Landau (GL) theory. The field-theory description of the competition between electronic interaction and topological responses due to probe electromagnetic fields $(A_0, \mathbf{A})$ is developed earlier in the context of fractional quantum Hall effect,[100, 101, 102, 103, 104, 105] and is termed as Chern-Simons-Ginzburg-Landau (CSGL) theory. In addition to probe fields, there may arise intrinsic 'statistical' gauge fields $(a_0, \mathbf{a})$. Thanks to the linear combination form of the intrinsic and probe gauge fields in the Lagrangian, we can combine their effects in a total gauge field as $\mathcal{A}_0 = a_0 + A_0$, and $\boldsymbol{\mathcal{A}} = \mathbf{a} + \mathbf{A}$. The full Lagrangian density can be split into four parts[6] [100, 101, 102, 103, 104, 105] $\mathcal{L}_{\rm total} = \mathcal{L}_{\rm KE} + \mathcal{L}_{\rm MW} + \mathcal{L}_{\rm GL} + \mathcal{L}_{\rm CS}$. $\mathcal{L}_{\rm KE}$ is the kinetic energy term which arises from the space and time-dependent parts of the field ϕ, and θ ($\mathcal{L}_{\rm KE} = 1/2(\partial_\mu\phi)(\partial^\mu\phi)$). $\mathcal{L}_{\rm MW}$ is the Maxwell term due to EM fields. These two terms do not contribute to the magnetic phase diagram and Higgs mode we set out to discuss below and thus are not included henceforth. The remaining GL and CS terms can be derived using the path integral description of coherent states of the total Hamiltonian $H_0 + H_{\rm SOC} + H_{\rm I}$, and then integrating out the fermionic degrees of freedom (Grassman variables) to obtain an effective CSGL theory.

[5] The magnetic state represents a non-trivial topological axion insulator in the small magnetic moment region near the critical point. However, owing to the loss of time-reversal symmetry, the surface state does not host any gapless state. We do not expect to observe any edge state in the DFT calculation.

[6] Additional CS terms related to anyons,[100, 101, 102, 103, 104, 105] and the Maxwell terms are not included since they do not directly impact the field ϕ in the lowest orders.

4.4.1 Ginzburg-Landau theory

Here we develop the GL theory of our Hamiltonian around the AFM order parameter. We write the partition function for the total Hamiltonian, $H + H_{\rm I}$ written in terms of the Dirac matrices in Eq. (4.9) as

$$Z = \int \mathcal{D}[\psi, \bar{\psi}] \exp\left[- \int_0^\beta d\tau \left(\bar{\psi}(\partial_\tau \mathbb{I}_{4\times 4} - H_{\mathbf{k}})\psi - J \sum_{\langle i,j \rangle} \mathbf{S}_i . \mathbf{S}_j \right) \right], \tag{4.16}$$

where ψ are 4 component Grassman variables $\psi = (\psi_{A\uparrow}, \psi_{B\uparrow}, \psi_{A\downarrow}, \psi_{B\downarrow})^T$ (same as the Dirac spinor used in the main text), and $\bar{\psi}$ is the conjugate of ψ. i,j denote 'A', 'B' sub-lattices. $\mathbf{S}_i$'s are the corresponding spin operators. We orient the spin-quantization axis along σ^z, i.e., we only consider S_i^z component. We define the AFM field as $\phi = (S_{\rm A}^z - S_{\rm B}^z)/2$. Using the Hubbard Stratonovich transformation for $H_{\rm I}$ in terms of the FM fields in the last term of Eq. (4.16), we obtain

$$\begin{aligned} \int \mathcal{D}[\psi, \bar{\psi}] \exp\left\{ \left(-J \sum_{\langle i,j \rangle} \mathbf{S}_i . \mathbf{S}_j \right) \right\} \;\; &= \;\; \int \mathcal{D}[\psi, \bar{\psi}, \phi, \bar{\phi}] \\ &\quad \times \exp\left[-J\phi(S_{\rm A}^z - S_{\rm B}^z) - \frac{\phi^2}{4J} \right]. \end{aligned} \tag{4.17}$$

Now we express S_i^z in terms of the Grassman variables as $S_i^z = (\bar{\psi}_{i\uparrow}\psi_{i\uparrow} - \bar{\psi}_{i\downarrow}\psi_{i\downarrow})/2$. In doing so, we can write the AFM term in terms of the Grassman spinor ϕ as $J\phi(S_{\rm A}^z - S_{\rm B}^z) = \bar{\psi}\left(J\phi\Gamma_5\right)\psi$, where $\Gamma_5 = \sigma_z \otimes \tau_z$, as defined in the main text. Substituting this identity in Eq. (4.17), and then inserting it back to Eq. (4.16), we get

$$Z = \int \mathcal{D}[\psi, \bar{\psi}, \phi, \bar{\phi}] \exp\left[- \int_0^\beta d\tau \bar{\psi} \left(\mathbf{G}_0^{-1}(\tau, \mathbf{k}) - \mathbf{M}(\phi) \right) \psi \right]. \tag{4.18}$$

Here we have defined the non-interacting Green's function matrix $\mathbf{G}_0^{-1}(\mathbf{k}, \tau) = \partial_\tau \mathbb{I}_{4\times 4} - H_{\mathbf{k}}$, and the magnetization matrix as $\mathbf{M}(\phi) = J\phi\Gamma_5$. Now we can go to the Matsubara frequency $i\omega_n$

domain and integrate out fermion variables $(\psi, \bar{\psi})$ to get the effective Lagrangian density as

$$\mathcal{L} = \mathrm{Log}\left[\mathrm{Det}\left(\sum_{i\omega_n,\mathbf{k}} \mathbf{G}_0^{-1}(i\omega_n,\mathbf{k}) - \mathbf{M}(\phi)\right)\right] - \frac{\phi^2}{4J}. \tag{4.19}$$

Under the saddle point approximation around the AFM, using the identity Log[Det[..]] = Tr[Log[..]] and $\mathrm{Log}[1+x] = -\sum_{n=1}^{\infty}(-1)^n x^n/n$, we get the GL Lagrangian potential

$$\mathcal{L}_{\mathrm{GL}} = \alpha|\phi|^2 + \beta|\phi|^4 + \mathcal{O}(|\phi|^6), \tag{4.20}$$

where

$$\alpha = -\frac{1}{4J} + \mathrm{Tr}\sum_{k,k'} \mathbf{G}_0(k)\Gamma_5\mathbf{G}_0(k')\Gamma_5, \tag{4.21}$$

$$\beta = \mathrm{Tr}\sum_{k,k',k'',k'''} \mathbf{G}_0(k)\Gamma_5\mathbf{G}_0(k')\Gamma_5\mathbf{G}_0(k'')\Gamma_5\mathbf{G}_0(k''')\Gamma_5, \tag{4.22}$$

where we define $k = (\mathbf{k}, i\omega_n)$. Exact computation of α and β variables are difficult, but we can already grasp the essence that $\beta > 0$, and $\alpha \to 0$ when the particle-hole bubble compensates the interaction terms. These results are typical for the GL theory.

4.4.2 The Chern-Simons term

Chern-Simons term arises in the presence of electromagnetic (EM) fields. In addition to probe fields, there may arise intrinsic 'statistical' gauge fields $(a_0, \mathbf{a})$ due to fluctuations of the bosonic fields ϕ. This can be seen easily. The statistical gauge field arises due to fluctuations of the order parameter, so we can write $a_0 \propto \partial_t(\delta\phi\delta\phi)$, and $\mathbf{a} \propto \nabla(\delta\phi\delta\phi)$, where $\delta\phi$ is the fluctuation of the AFM field around its saddle point ϕ_0. Such intrinsic gauge clearly arises from the $|\phi|^4$ term in the GL potential in Eq. (4.20), and persists above the AFM critical point. We are not particularly interested in the details of the origin of the intrinsic gauge field, except it conveys an important message that such due to spin-fluctuations in space-time dimensions, there can be CS term even

in the absence of any external EM field. Readers interested in the details of the origin of such statistical gauge field can refer to Refs. [106, 107, 98] and references therein

Due to the total EM field, we have a typical Maxwell term ($\mathcal{L}_{\rm MW}$), and the ~~Chern-Simons~~ θ term $\mathcal{L}_{\rm CS}$ as defined in 3+1 dimensions as[95, 96, 97, 108, 109, 110, 111]

$$\mathcal{L}_{\rm MW} = -\frac{1}{4}\mathcal{F}_{\mu\nu}\mathcal{F}^{\mu\nu} - \mathcal{A}_\mu\mathcal{J}^\mu, \tag{4.23}$$

$$\mathcal{L}_{\rm CS} = \theta\frac{\hbar}{\Phi_0^2}\epsilon^{\mu\nu\sigma\tau}\partial_\mu\mathcal{A}_\nu\partial_\sigma\mathcal{A}_\tau - \mathcal{A}_\mu\mathcal{J}^\mu. \tag{4.24}$$

where the Einsteins summation convention is implied. $\mathcal{F}_{\mu\nu} = \partial_\mu\mathcal{A}_\nu - \partial_\nu\mathcal{A}_\mu$, current density $\mathcal{J}^\mu$ is included by conservation principles and can be eliminated for the Lagrangian minimization problem of our interest. θ is the axion angle which is related to the momentum-space non-Abelian Berry connection $\mathscr{A}_\mu^{st} = -i\langle u_{\mathbf{k}}^s|\partial_{k_\mu}u_{\mathbf{k}}^t\rangle$, where $|u_{\mathbf{k}}^s\rangle$ is the $s^{\rm th}$-eigenstate of the mean-field Hamiltonian, as

$$\theta = \frac{1}{4\pi}\int_{\rm BZ} d^3k\epsilon^{\mu\nu\sigma}{\rm Tr}\left[\mathscr{A}_\mu\partial_\nu\mathscr{A}_\sigma + i\frac{2}{3}\mathscr{A}_\mu\mathscr{A}_\mu\mathscr{A}_\mu\right]. \tag{4.25}$$

By evaluating the eigenvectors of our Hamiltonian in the main text, we can obtain an algebraic, gauge independent form of the axion angle can be deduced to be:

$$\theta = \int_{\rm BZ}\frac{d^3k}{4\pi}\frac{2|d| + d_4}{(|d| + d_4)^2|d|^3}\epsilon^{ijkl}d_i\partial_{k_x}d_j\partial_{k_y}d_k\partial_{k_z}d_l. \tag{4.26}$$

where $|d|^2 = \sum_{i=1}^5 |d_i|^2$, and $d_5 = J\phi$, and i, j, k, l runs from 1,2,4,5. The above integral evaluates the solid angle enclosed in the d-space as one encircles the entire 3D Brillouin zone in the k-space. Reminiscence to the topological phase transition in a single SSH chain, here also show that θ acquires finite value where the zeros of $d_3(\mathbf{k})$ term lie inside the solid angle, giving the condition that $T_{\mathbf{k}_\perp} \leq T'_{\mathbf{k}_\perp}$, for $\mathbf{k} \in$ BZ. Having a Dirac cone in the SOC band structure, we ensure that such a condition is automatically satisfied in the non-interacting phase ($d_5 = 0$). Axion angle is calculated numerically (see below).

4.4.3 Chern-Simons-Ginzburg-Landau theory

The kinetic energy term due to the AFM field

$$\mathcal{L}_{\rm KE} \;=\; i\phi^*\mathcal{D}_0\phi + \frac{1}{2m}\phi^*\boldsymbol{\mathcal{D}}^2\phi. \tag{4.27}$$

Here the covariant derivative operators are $\mathcal{D}_0 = \partial_t + ie\mathcal{A}_0$, and $\boldsymbol{\mathcal{D}} = i\boldsymbol{\nabla} + e\boldsymbol{\mathcal{A}}$. Therefore the total Lagrangian density becomes[108, 109, 110, 111, 106, 107] $\mathcal{L}_{\rm total} = \mathcal{L}_{\rm KE} + \mathcal{L}_{\rm MW} + \mathcal{L}_{\rm GL} + \mathcal{L}_{\rm CS} + \mathcal{L}_{\rm AN}$. Here $\mathcal{L}_{\rm AN}$ represents the contribution from anyons arising from the fluctuation of the order parameters. The Maxwell term does not involve the order parameter or axion term, and thus also can be neglected. Neglecting space-time dependence of the order parameter, we obtain the effect GL and CS term in terms of the AFM field ϕ as

$$\mathcal{L}_{\rm GL} = \alpha|\phi|^2 + \beta|\phi|^4, \quad \mathcal{L}_{\rm CS} = \theta\frac{\hbar}{\Phi_0^2}\mathbf{E}\cdot\mathbf{B}, \tag{4.28}$$

Apparently, there is no direct coupling between the scalar field ϕ and the pseudo-scalar axion mode θ, rather the axion field θ directly stems from the scalar field ϕ, Eq. (4.15).We are interested in studying the behavior of θ as a function AFM field ϕ, which yields an exponential function $\pi e^{-\lambda|\phi|}$, where λ is a fitting parameter. For both signs of ϕ, ϕ decreases from π at $\phi \to 0$. Absorbing the remaining factors in the CS term into $\gamma = \frac{\pi\hbar}{\Phi_0^2}\mathbf{E}\cdot\mathbf{B}$, we obtain $\mathcal{L}_{\rm CS} = \gamma e^{-\lambda|\phi|}$. $\gamma > 0$ ($\gamma < 0$) if $\mathbf{E}$ and $\mathbf{B}$ are parallel (antiparallel) to each other. Substituting for θ in Eq. (4.28), we get $\mathcal{L}_{\rm CS} = \gamma e^{-\lambda|\phi|}$, where $\gamma = \frac{\pi\hbar}{\Phi_0^2}\mathbf{E}\cdot\mathbf{B}$ is a variational parameter. $\gamma > 0$ ($\gamma < 0$) if $\mathbf{E}$ and $\mathbf{B}$ are parallel (antiparallel) to each other, and otherwise zero. Neglecting the irrelevant space-time dependence of the order parameter, we arrive at the CSGL term, expressed exclusively in terms of the AFM field ϕ as

$$\mathcal{L}_{\rm CSGL} \;=\; \alpha|\phi|^2 + \beta|\phi|^4 + \gamma(e^{-\lambda|\phi|} - 1). \tag{4.29}$$

(We have added a constant term $-\gamma$ to shift the Free energy ($\propto \mathcal{L}$) minimum to zero at $\phi = 0$). The magnetic phase transition and magnetic excitations can now be studied as a function of four variational parameters α, β, γ, and λ.

4.4.4 Magnetic phase diagram

Minimization of $\mathcal{L}_{\mathrm{CSGL}}$ at a finite value of $\phi = \phi_0$ is obtained by solving the equation

$$\left.\frac{\partial F[\phi]}{\partial \phi}\right|_{\phi_0} = 0 \tag{4.30}$$

which gives the following secular equation:

$$2\left(\alpha + 2\beta|\phi_0|^2\right)|\phi_0| = \gamma\lambda e^{-\lambda|\phi_0|}. \tag{4.31}$$

A solution of the Eq. 4.31 is non-trivial to manage analytically. For $\gamma \to 0$, we recover the typical GL result of $|\phi_0| = \sqrt{-\alpha/2\beta}$, giving a second order phase transition as α becomes negative (with $\beta > 0$).

For small λ in Eq. 4.31, we can expand the exponential up to third power in ϕ to get

$$\alpha|\phi|_0 + 4\beta|\phi|_0^3 - \lambda\gamma(1 - \lambda|\phi| + \frac{\lambda^2|\phi|^2}{2!} - \frac{\lambda^3|\phi|^3}{3!}) = 0. \tag{4.32}$$

It turns out that any arbitrarily small value of γ, this leads to a minima in free energy away from $\phi = 0$ but very close. At high temperature, it goes arbitrarily close to 0.

Since we are in the vicinity of a second order phase transition, we set $\beta > 0$, and $\lambda = 220$ (from Fig. 4.8 (a)). We study the solution of ϕ_0 as a function of α and γ, as given in Fig. 3b. For $\gamma > 0$ region, we find that ϕ_0 decreases *continuously* to zero, suggesting a second order phase

transition as a function of both α, and λ. On the other hand, for $\gamma < 0$, we notice that the phase boundary from finite ϕ_0 to zero is *discontinuous*, implying that the phase transition becomes first order. To understand this behavior, we expand the CS term in the leading order in $|\phi|$ as $-\gamma\lambda|\phi|$. So, for $\gamma > 0$, $\mathcal{L}_{\rm CSGL}$ decreases with increasing $|\phi|$, and hence its minima continuously move from $\phi = 0$ to $|\phi_0| > 0 -$ a second order phase transition. While for $\gamma < 0$, the increases with increasing $|\phi|$, and then a second minima occurs at a finite $|\phi_0| > 0$. Since $|\phi_0|$ minima are now disjointed from the $\phi = 0$ minima, we have a first order phase transition.

In both cases, we also observe that the phase boundary shifts from the GL limit of $\alpha = 0$ line to finite values of $\pm\alpha$ in the two cases, respectively. This has implications to the values of the Néel temperature and the Higgs mass.

If we assume $T_{\rm N,0}$ to be the Néel temperature without the axion term, then for a second order phase transition, we can write

$$\alpha = a_0(1 - T/T_{\rm N,0}), \tag{4.33}$$

where $\alpha_0 > 0$ is a constant. This coefficient is modified to [7]

$$\alpha' = \alpha + \gamma\lambda^2/2 \tag{4.34}$$

$\alpha' = 0$ gives the AFM transition. Therefore, the phase transition condition becomes

$$\alpha_0 \left(1 - \frac{T_{\rm N}}{T_{\rm N,0}}\right) + \gamma\lambda^2/2 = 0, \tag{4.35}$$

which gives

$$T_{\rm N} = T_{\rm N,0} \left(1 + \frac{\gamma\lambda^2}{2\alpha_0}\right). \tag{4.36}$$

$T_{\rm N}$ increases (decreases) for $\gamma > 0$ ($\gamma < 0$). This means, $T_{\rm N}$ increases (decreases) as the applied

[7] By adding the quadratic term of the CS free energy from Eq. 4.29

magnetic and electric fields are parallel (antiparallel), which provides a unique testbed to verify the topological nature of this magnetic ground state.

4.4.5 Magnetic excitations

Finally, we study the interplay between the magnetic and topological excitations. We expand the order parameter near its expectation value as $\phi = |\phi_0 + \delta\phi(x)|e^{i\eta(x)}$, where $\delta\phi$, and η are the corresponding amplitude, and phase fluctuations, respectively. In Eq. (4.28), we find that $\mathcal{L}_{\rm CSGL}$ depends on the amplitude $|\phi|$ only, and thus the phase, η, fluctuations remain gapless (Goldstone modes) even in the presence of the axion term [In fact, the Goldstone modes can be gauged out by a suitable gauge transformation of the electromagnetic fields $\mathcal{A}$]. Substituting $\phi = |\phi_0 + \delta\phi(x)|$ in Eq. (4.28), we can estimate the mass of the amplitude mode as

$$M = \frac{1}{2}\partial^2_{\delta\phi}\mathcal{L}|_{\delta\phi=0}. \tag{4.37}$$

After substituting Eq. (4.31) at the saddle point of the Lagrangian, we obtain the Higgs mass as

$$M = \alpha + \lambda\alpha|\phi_0| + 6\beta|\phi_0|^2 + \lambda\beta|\phi_0|^3. \tag{4.38}$$

For $\gamma \to 0$, we recover the GL value of $M = 4\beta|\phi_0|^2$ vanishing at the critical point where $\phi_0 \to 0$. However, in the present case, we find that there is a finite Higgs mass even above the critical point and eventually vanishes only when $\alpha = 0$. On the other hand, for $\gamma > 0$, we notice in Fig. 3b, that a continuous phase transition can occur at $\alpha > 0$, giving a non-vanishing Higgs mass at the critical point, which may be called 'topological paramagnons'. For $\gamma < 0$, we have a first order phase transition at $\alpha < 0$, where the order parameter is discontinuous, and thus also the Higgs mass must vanish discontinuously.

Calculation of Higgs mode's lifetime is rather cumbersome. One source of Higgs lifetime is the quartic term in the Lagrangian. In this spirit, the leading term in the inverse lifetime (τ)

is proportional to the coefficient of the $\delta\phi^3$, which can be obtained from $\partial^3\mathcal{L}_{\rm CSGL}/\partial\delta\phi^3|_{\delta\phi=0}$, leading to

$$\frac{1}{\tau} \propto 2(12\beta - \alpha\lambda^2)|\phi_0| - 4\lambda^2\beta|\phi_0|^3. \tag{4.39}$$

The result suggests that Higgs lifetime rather decreases near the critical point for $\gamma \neq 0$, while away from the critical point, as the second term becomes dominant, it tends to increase. Hence we can argue that the 'topological paramagnons' have much-reduced decay rate, and is topologically protected.

4.5 Conclusions and outlook

In the present model, axion is a pseudo-scaler, and there is only one Higgs mode. Therefore, the axion-Higgs coupling can be captured well within the proposed CSGL theorem, and the corresponding Lagrangian resemblance that of the Standard Model of the particle physics. It is known that in the case of a Higgs doublet, there arises axion-Higgs cross term in the Lagrangian, and the system loses its CSGL symmetry, and one obtains a so-called Peccei-Quinn (PQ) symmetry, which violates the Standard model.[112, 113] However, the predicted Higgs doublet is yet to be observed. Based on the above analysis, we anticipate that our work will stimulate research for the realization of PQ symmetry in condensed matter systems where topological axion and Higgs terms are intertwined.[112, 113]

5

Bosonic Integer and Fractional Quantum Hall effect in an interacting lattice model

Topological states of matter have recently got a surge of attention due to their non-trivial properties and unconventional behavior like the presence of edge states, the non-trivial signature of quantum entanglement, among others. Furthermore, Bosonic systems with non-trivial topological states have also gained a lot of attention in the last few years. Since bosons tend to condense without interaction, we need interaction between bosons to stabilize any topological phases in the system, unlike the fermionic counterpart which can host (symmetry protected) topologically non-trivial ground states even in the absence of interaction. This makes the study of the topological phases intrinsically non-trivial in bosonic systems.

Recently an idea for realizing the bosonic integer quantum Hall effect (BIQHE) was proposed by Senthil and Levin [114] as an example of an interacting symmetry protected topological (SPT) phase for bosons where the boson number conservation can stabilize the topological phase in absence of time reversal symmetry. The proposal contains two flavors of bosons (say b_1 and

b_2) and by attaching a mutual flux of one species of boson with another (using flux attachment Chern-Simons theory)[1], it was shown that the system can host a BIQH ground state. A lattice realization of similar kind of state was demonstrated by He,*et. al*, [7]. In a subsequent work[115], using bosonization techniques within a coupled wire construction, it was proposed that the same model can also host bosonic fractional quantum Hall (BFQH) ground state at 1/3 filing and is described by the Halperin [221] state. In our present work, we explore the presence of BIQH as well as BFQH states in the same model as used in Refs. [7] and [115] at 1/2 and 1/3 filling respectively using exact diagonalization calculations and present preliminary evidence for such phases. The model consists of hard-core bosons spread over honeycomb lattice with the nearest neighbor and correlated next nearest neighbor hopping. There is also a background gauge flux which explicitly breaks the time reversal symmetry. We have found unique ground states of the system on a finite honeycomb lattice at both the fillings for open boundary conditions.

Although the BIQH phase is an example of symmetry protected topological (SPT) phase, the BFQH phase is a symmetry enriched topologically ordered state[2] that can host fractional bosonic excitations whose signatures are revealed in a charge pumping experiment. We adiabatically insert 2π flux through the center of the system and observe a charge flow of 2/3, which is a signature that the ground state has a quantized charge conductance, $\sigma_{xy} = 2/3$[116]. We have also looked at the excitation spectrum to confirm the presence of chiral edge modes.

[1]Mutual flux attachment is achieved by the following transformation:[114]

$$\tilde{b}_1(x) = e^{-i\int d^2x'\Theta(x-x')\rho_2(x')}.b_1(x), \text{ and}$$
$$\tilde{b}_2(x) = e^{-i\int d^2x'\Theta(x-x')\rho_1(x')}.b_2(x)$$

[2]topologically ordered states are the one which doesn't need any symmetry protection per say and classified by topological order but in presence of symmetry, there is a finer scale of classification and is characterized by the "symmetry enriched topological order"

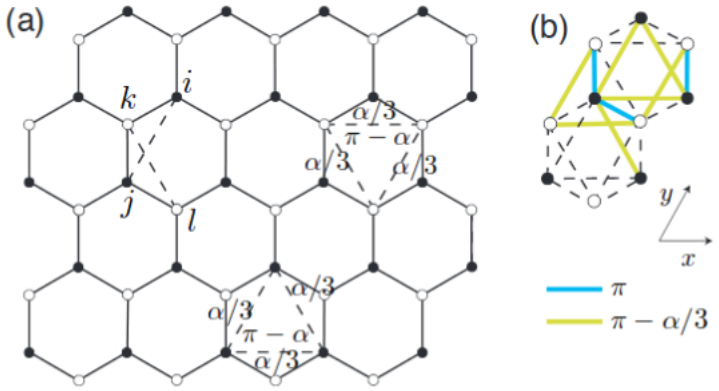

Figure 5.1: Figure showing bipartite honeycomb lattice along with one of the possible gauge choice having π flux per plaquette. The figure is taken from the Ref. [7]

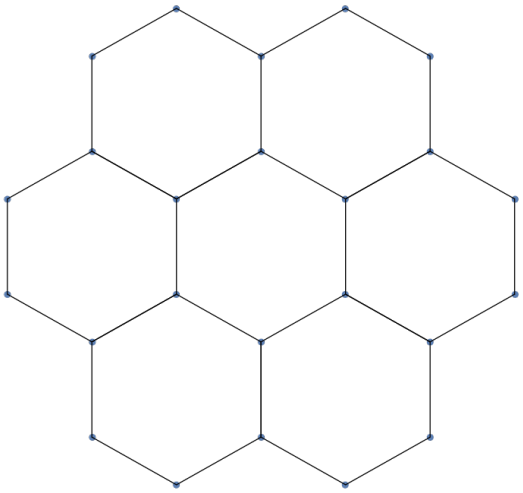

Figure 5.2: System used to perform exact diagonalization calculations at 1/2 filling and 1/3 filling. This system has C_6 rotation symmetry along with two reflection planes. It consists of 24 sites and BIQH and BFQH calculations were performed with 12 and 8 particles respectively.

5.1 Model

We work on a specific model proposed earlier to verify the presence of Bosonic Integer and Fractional Quantum Hall Effect (BFQHF)[7, 115]. Our system consists of hardcore bosons on

a honey-comb lattice with nearest neighbor (NN) and correlated next nearest neighbor (NNN) hopping described by the Hamiltonian

$$\begin{aligned}\mathcal{H} &= \sum_{<<i,j>>} e^{iA_{ij}} \left(2n_k^b - 1\right) a_i^\dagger a_j + h.c. \\ &+ \sum_{<<k,l>>} e^{iA_{kl}} \left(2n_j^a - 1\right) b_k^\dagger b_l + h.c. \\ &+ \lambda \sum_{<i,k>} e^{iA_{ik}} a_i^\dagger b_k + h.c.\end{aligned} \tag{5.1}$$

where $a(a^\dagger)$ and $b(b^\dagger)$ are bosonic creation (annihilation) operators on different sub-lattices with hard core constraint such that

$$(a_i^\dagger)^2 = (b_j^\dagger)^2 = 0, \tag{5.2}$$

$n_i^{a(b)} = a_i^\dagger a_i (b_i^\dagger b_i)$ is the particle number operator of the bosons of species $a(b)$, A_{ij} is the Pierls phase to incorporate the presence of a magnetic field in the system, "$<,>$" and "$<<,>>$" denotes NN and NNN respectively and λ is a tuning parameter. The first two terms are correlated hopping, i.e, hopping between A sub lattices depends on the occupation of intermediate B sub-lattice while the last term is a normal hopping between A and B sub-lattices. In this model, the two sub lattices behaves as two component bosons and the correlated hopping implements the flux attachment picture discussed in Appendix E. This can be understood in the following way: $n_i^{a(b)}$ can take values either 0 or 1, hence we can write

$$(2n_i^\alpha - 1) = -e^{i\pi n_i^\alpha} \tag{5.3}$$

(where $\alpha = a/b$ is the sub-lattice index), hence the Hamiltonian in Eq. 5.2 becomes

$$\begin{aligned}\mathcal{H} = & - \sum_{<<i,j>>} e^{iA_{ij}} e^{i\pi n_k^b} a_i^\dagger a_j + h.c. \\ & - \sum_{<<k,l>>} e^{iA_{kl}} e^{i\pi n_j^a} b_k^\dagger b_l + h.c. \\ & + \lambda \sum_{<i,k>} e^{iA_{ik}} a_i^\dagger b_k + h.c.\end{aligned} \tag{5.4}$$

in the above Hamiltonian, it is easy to see that if a particle is present at an intermediate site, the next nearest neighbor hopping term will acquire an extra phase of π while if there is no particle present at an intermediate site, no extra phase will be acquired by the next nearest neighbor hopping term. This is equivalent to the mutual flux attachment of one species of boson onto another.

At $\lambda = 0$, the system has $U(1) \times U(1)$ symmetry, i.e., particle number on both the sub-lattices are conserved individually (n^a and n^b both are conserved). In other words, the charge ($n^a + n^b$) and the pseudo spin ($n^a - n^b$) both are individually conserved. For any finite value of λ, tunneling between the sub-lattices is allowed and hence the $U(1) \times U(1)$ breaks down to the global $U(1)$ symmetry (only the total charge, $n^a + n^b$ is conserved).

5.2 Limiting cases

In this section, we will study two limiting cases of the Hamiltonian in Eq. [5.2]: (i) when $\lambda = 0$ and (ii) when $\lambda \to \infty$

5.2.1 $\lambda = 0$

when $\lambda = 0$ the Hamiltonian in Eq. 5.2 reduces to

$$\mathcal{H} = \sum_{<<i,j>>} e^{iA_{ij}} \left(2n_k^b - 1\right) a_i^\dagger a_j + h.c. \\ \sum_{<<k,l>>} e^{iA_{kl}} \left(2n_j^a - 1\right) b_k^\dagger b_l + h.c. \tag{5.5}$$

this Hamiltonian is known to host BIQHE at half filling [7]. At filling $\nu = 1/3$, this system was proposed to host BFQHE as well[115]. In the later sections, we will provide evidence for the presence of BIQH as well as BFQH ground states of the system at different fillings.

5.2.2 $\lambda \to \infty$

When $\lambda \to \infty$, the Hamiltonian (normalized with λ) in Eq. [5.2] reduces to

$$\mathcal{H} = \sum_{<i,k>} e^{iA_{ik}} a_i^\dagger b_k + h.c. \tag{5.6}$$

This can be easily mapped to the $XY-$model by mapping the creation ($a_i^\dagger$ and $b_i^\dagger$) and annihilation (a_i and b_i) operators to spin lowering (S_i^-) and raising (S_i^+) operators respectively. It can be shown by using mean field theory as well as other more sophisticated methods that the Hamiltonian in Eq. [5.6] possess an SF ground state. We have calculated the super-fluid density (by calculating $\sigma_x - \sigma_x$ correlation functions) for the Hamiltonian in Eq. [5.6] to verify the presence of super-fluid ground states. As the magnetic flux is π through each hexagon, the magnetic unit cell contains 2 conventional unit cells. Hence, for a single particle, the Hamiltonian becomes a 4×4 matrix having extremal eigenvalues at wave vectors $\pm(\pi/6, \pi/2)$ and $\pm(5\pi/6, \pi/2)$[117] and the soft modes are supposed to lie around these points.

5.3 Bosonic Integer Quantum Hall Effect: $\nu = 1/2$

In this section, we will study the ground state and a few excited states of the Hamiltonian presented in Eq. 5.2 on a finite honeycomb lattice shown in Fig. 5.2 using exact diagonalization (using Lanczos algorithm). The total number of sites is 24 and we fix the particle number to be 12 such that the filling $\nu = 1/2$. We fix the flux through each hexagon to be π. More information about the gauge choice can be found in Appendix F. It should be noted that due to the π flux through each hexagon, the magnetic unit cell becomes twice (4 sites) that of the primitive unit cell (2 sites).

5.3.1 Phase diagram

This model is supposed to possess a BIQH ground state(GS)[7] for small λ when the flux per plaquette is set to π at half filling. Here we try to confirm the presence of the BIQH GS using exact diagonalization on a small system. We calculate the ground state fidelity [Fig. 5.3 (a)] and fidelity susceptibility [Fig 5.3 (b)] to characterize the different phases of the system[118, 119]. Fidelity (which comes from a concept in quantum information) is the overlap of the two ground states $|\psi(\lambda)\rangle$ and $|\psi(\lambda + \delta\lambda)\rangle$[120, 121, 122]

$$\mathcal{F}(\lambda, \lambda + \delta\lambda) = |\langle\psi(\lambda)|\psi(\lambda + \delta\lambda)\rangle| \tag{5.7}$$

The fidelity susceptibility is defined as

$$\chi(\lambda) = \lim_{\delta\lambda \to 0} \frac{-2ln\mathcal{F}(\lambda, \lambda + \delta\lambda)}{(\delta\lambda^2)} \tag{5.8}$$

Any non-analyticity in $\chi(\lambda)$ is a signature of qualitative difference in the two ground states across a quantum phase transition[123]. Therefore QPTs can be characterized by χ[119, 123, 124, 125, 126, 127, 128, 129]. We find that for $\lambda >> 1$ the system has a super-fluid GS. We observe only

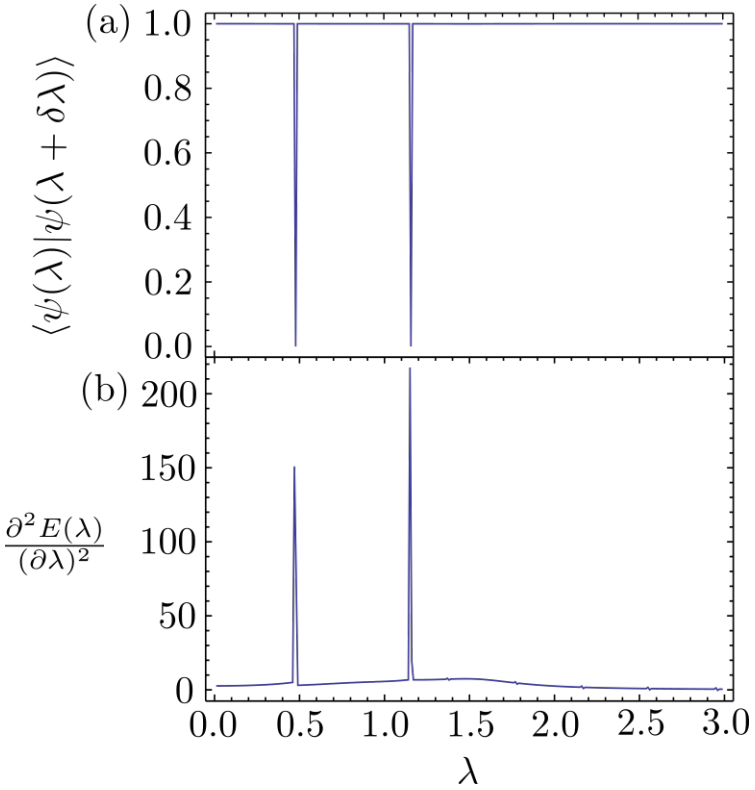

Figure 5.3: (a) Fidelity and (b) fidelity susceptibility showing the phase transition as a function of λ for 12 particles (i.e, $\nu = 1/2$) in the Hamiltonian in Eq. 5.2. Two phase transitions happen at $\lambda \sim 0.5$ and $\lambda \sim 1.2$. The first phase transition at $\lambda \sim 0.5$ is an artifact of the finite system as discussed in a later section and is expected to go away in the thermodynamic limit.

two phase transitions (with the help of χ), at $\lambda \sim 0.5$ and $\lambda \sim 1.2$. Below $\lambda \sim 0.5$, the GS is a BIQH state and above $\lambda \sim 1.2$, the GS is a super-fluid. The phase in between $\lambda \sim 0.5$ and $\lambda \sim 1.2$ is also a BIQH state in the bulk. Due to the instability of higher angular momentum states on the edge, a state that is adiabatically connected to an edge excitation at $\lambda = 0$ becomes the ground state of the system for $0.5 < \lambda < 1.2$ (as shown in the Fig. 5.7). This instability is discussed in detail in a later section.

5.3.2 Superfluid Density

As mentioned earlier, we can map the hard-core boson model to a spin model by using the transformation

$$a_i(b_i) = S^-_{i,a(b)}, a^\dagger_i(b^\dagger_i) = S^+_{i,a(b)} \tag{5.9}$$

such that

$$a^\dagger_i a_j + hc = S^x_{i,a}S^x_{j,a} + S^y_{i,a}S^y_{j,a}, \text{and} \tag{5.10}$$

$$a^\dagger_i a_i = \left(\frac{1}{2} + S^z_{i,a}\right). \tag{5.11}$$

Now the model Hamiltonian in Eq. 5.2 can be transformed into the spin XY Hamiltonian. The superfluid phase can be characterized by calculating the superfluid density (ρ_{SF}) given by

$$\rho_{\mathcal{SF}}(i,j) = \langle S^x_i S^x_j + S^y_i S^y_j \rangle, \tag{5.12}$$

which is equivalent to the calculation of $\langle a^\dagger_i a_j + a^\dagger_j a_i \rangle$ in the equivalent hard core boson model. The super-fluid density shows a dramatic change across the phase transition around $\lambda = 1.2$ which is demonstrated in Fig. 5.4.

5.3.3 Charge Pump

Charge pumping is a unique property of a quantum Hall system and is often used to characterize the quantum Hall state. It is expected from a quantum Hall system that an extra flux threaded through the system will cause charge pumping to the edge and its magnitude will depend on the strength of the applied magnetic field as well as the Chern number. To explore the presence of BIQHE we added an extra $B_1\delta(\vec{r})$ flux in the system [Fig 5.6]. This extra flux, upon changing by 2π, causes a spectral flow to the edge from the bulk (or from the edge to the bulk) and leads to

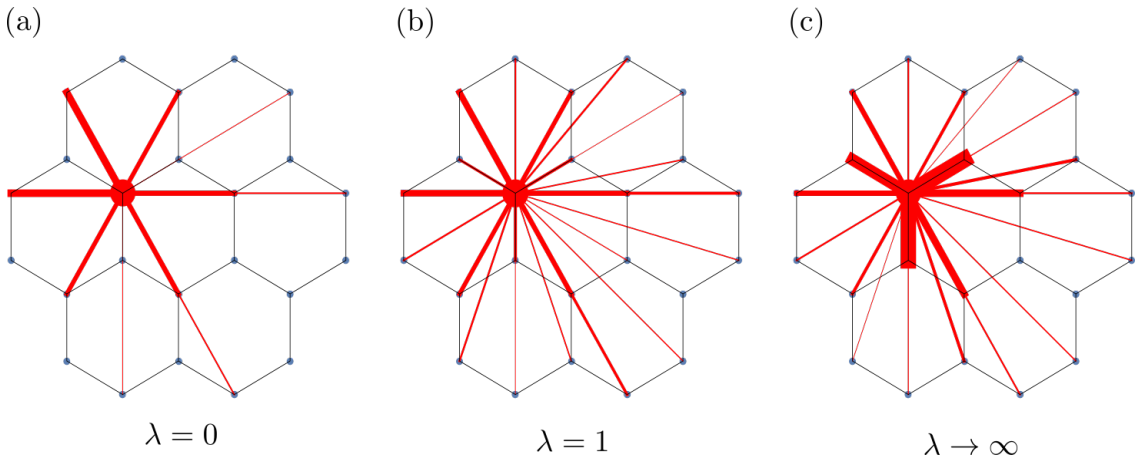

Figure 5.4: Figure to show $\rho_{\mathcal{SF}}(1,i)$ correlation on the lattice at (a) $\lambda = 0$, (b) $\lambda = 1$ and (c) $\lambda \to \infty$. The thickness of the red line between sites i and j shown corresponds to the magnitude of $\rho_{SF}(i,j)$.

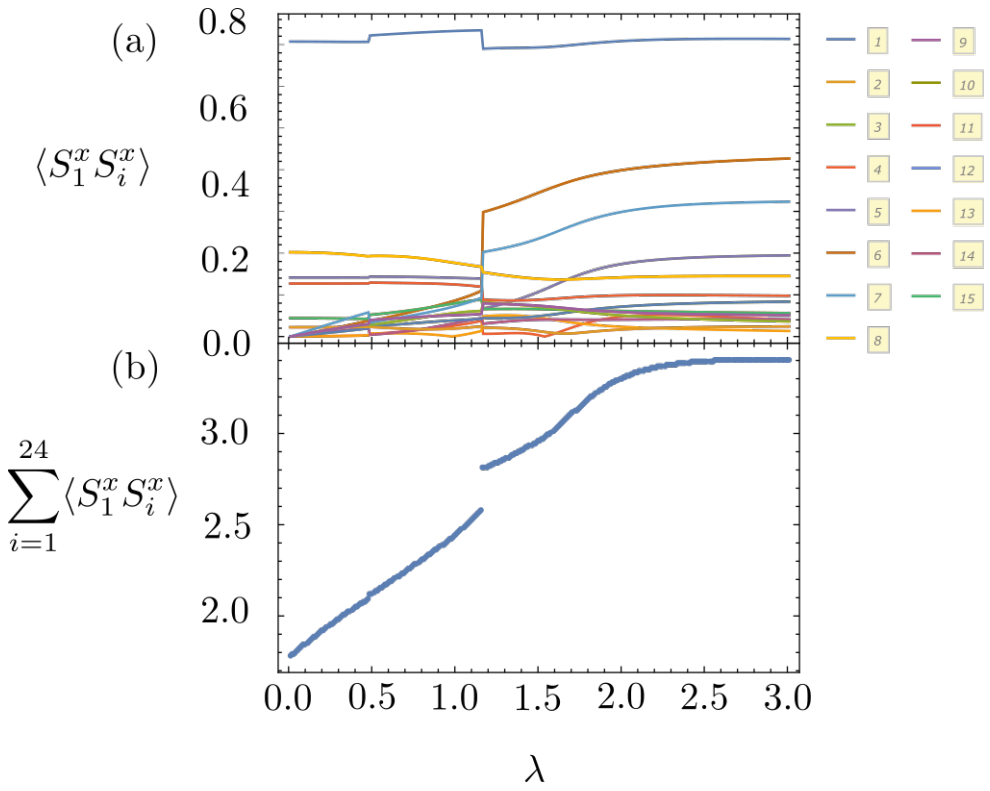

Figure 5.5: Plot to show (a) $\rho_{\mathcal{SF}}(1,i)$ and (b) $\sum_{i=1}^{24} \rho_{\mathcal{SF}}(1,i)$ as a function of λ($\lambda = 0$ to $\lambda = 3$). The sudden jump in $\rho_{\mathcal{SF}}(1,i)$ corresponds to the transition to a superfluid phase.

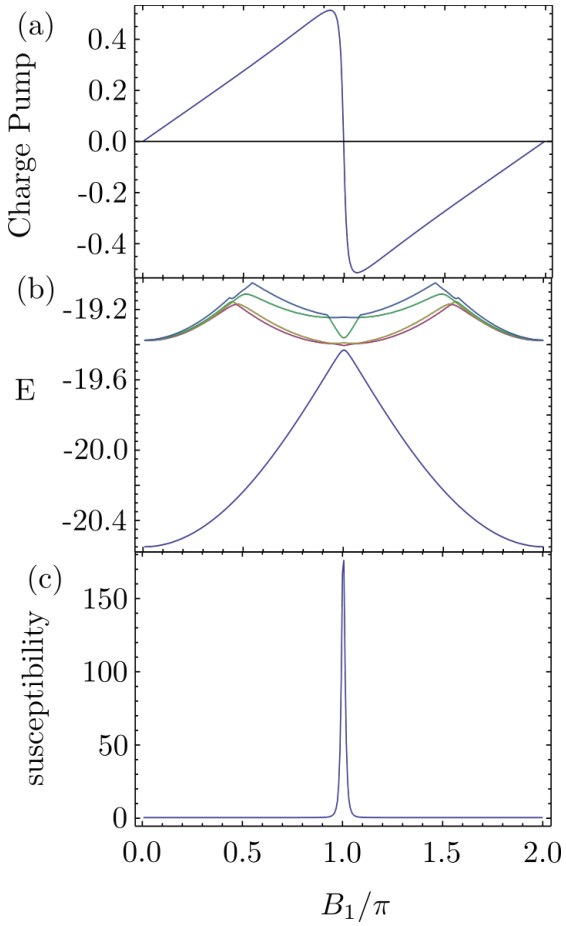

Figure 5.6: Figure showing (a) charge pumping, (b) evolution of low energy states and (c) fidelity of the ground state as a function of the threaded flux B_1. There is a jump in the charge pump because of an unavoidable phase transition happening in the system as demonstrated in (b) and (c).

charge pumping. The charge pump is defined as

$$\text{Charge Pump} = \sum_i{}' \langle a_i^\dagger a_i \rangle_{B=B_0} - \langle a_i^\dagger a_i \rangle_{B=0} + \sum_j{}' \langle b_j^\dagger b_j \rangle_{B=B_0} - \langle b_j^\dagger b_j \rangle_{B=0}, \tag{5.13}$$

where the restricted summation runs over the edge of the system. The quantity of charge pumped is exactly the same as the transverse conductivity, σ_{xy}.

5.3.4 Excitation Spectrum

The existence of excitations on the edge is also a hallmark of quantum Hall states. A unique degeneracy pattern can be derived for any given K-matrix. In the present case, the K-matrix[7] is given by[3]

$$K = \begin{pmatrix} 0 & 1 \\ 1 & 0 \end{pmatrix}, \tag{5.14}$$

We calculate the spectrum of eigenstates to check the degeneracy of the first excited state [Fig 5.7 (a)] and the gap between the ground state and the first excited state [Fig. 5.7 (b)]. The first excited state is four-fold degenerate at $\lambda = 0$ as expected from the edge theory shown in the Appendix G.

The K-matrix has a lot more information about the quantum Hall state than just the edge excitation spectra. The absolute value of the determinant of the K-matrix gives the degeneracy of the GS on a 2-Torus and the sign of the eigenvalues of it gives the directionality of the modes. In the present case, Det$[K] = -1$ and the eigenvalues are ± 1, which means that the ground state is not topologically ordered, it is an integer quantum Hall state and there are two counter propagating edge modes[130].

[3]One can write down the effective theory for the most general Abelian quantum Hall state by introducing N emergent gauge field a^i_μ, with $i = 1...N$ as

$$S_K[a^i, A] = \int d^3x \frac{1}{4\pi} K_{ij} \epsilon^{\mu\nu\rho} a^i_\mu \partial_\nu a^j_\rho + \frac{1}{2\pi} t_i \epsilon^{\mu\nu\rho} A_\mu \partial_\nu a^i_\rho$$

where K-matrix specifies the various Chern-Simons couplings and t_i specifies the linear combinations of currents.

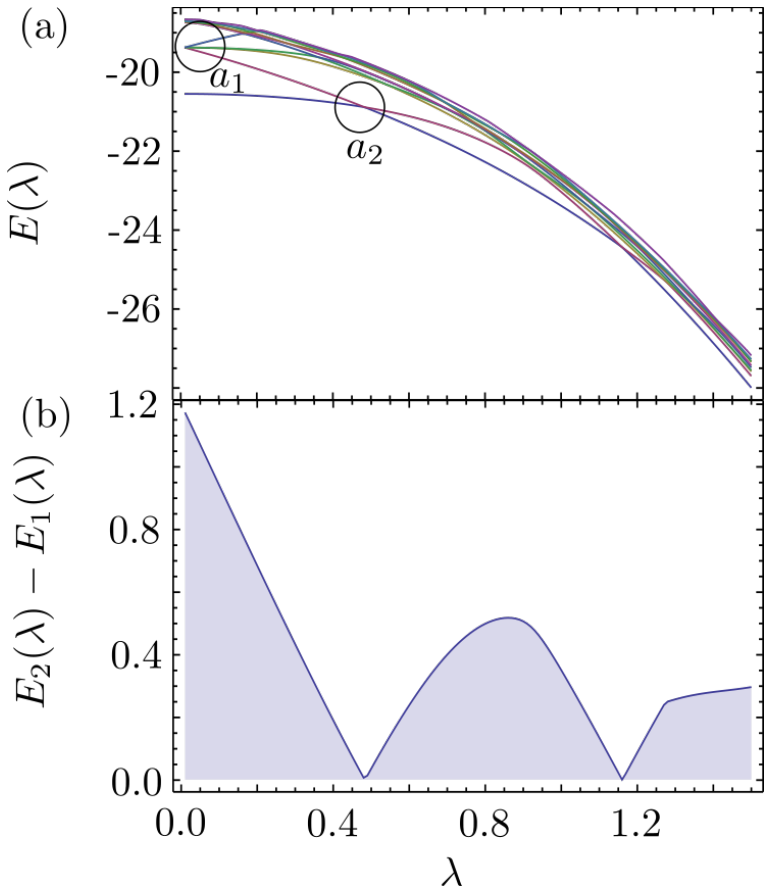

Figure 5.7: Plot showing (a) Exact eigenstate spectrum and (b) gap to the first excitation as a function of λ. Four-fold degeneracy of the first excited (indicated by a_1) state is consistent with the edge theory presented in Ref. [7]. a_2 indicates the crossing of the ground state and the first excited state at $\lambda \sim 0.5$.

5.4 Bosonic Fractional Quantum Hall Effect: $\nu = 1/3$

In this section, we again study the ground state and a few excited states of the Hamiltonian presented in Eq. 5.2 on a finite honeycomb lattice shown in Fig. 5.2 but fix the particle number to be 8 such that the filling $\nu = 1/3$. The flux through each hexagon is still π and the gauge choice is still the same (see Appendix F).

5.4.1 Phase Diagram

This model (Hamiltonian in Eq. 5.2) was proposed to possess a BFQH ground state(GS)[115] for $\nu = 1/3$ when the flux per plaquette is set to π. Here, again we try to confirm the presence of BFQH GS using exact diagonalization on a small system (Fig. 5.1). We calculate the fidelity ($\mathcal{F}$) and the fidelity susceptibility (χ) [Fig 5.8 (a-b)] to characterize the different phases of the system. We find that for $\lambda >> 1$ the system has a super-fluid GS. We again observe only two phase transitions (with the help of $\mathcal{F}$ and χ), at $\lambda \sim 0.2$ and $\lambda \sim 1.2$. Below $\lambda \sim 0.2$, the GS is a BFQH state and above $\lambda \sim 1.2$, the GS is a super-fluid. The phase in between $\lambda \sim 0.2$ and $\lambda \sim 1.2$ is also a BFQH state in the bulk, but due to the instability of higher angular momentum states on the edge, a state that is adiabatically connected to one of the edge excitations at $\lambda = 0$ becomes the ground state of the system for $0.5 < \lambda < 1.2$, similarly to the half-filled case discussed earlier.

5.4.2 Charge Pump

To confirm the presence of BFQHE we again added an extra $B_1\delta(\vec{r})$ flux in the system. It is expected for a fractional quantum Hall system that this extra flux will cause charge pumping to the edge and its magnitude will depend on the strength of the applied magnetic field [Fig 5.9].

5.4.3 Excitation Spectrum

The BFQH state can be described by the Halperin [221] state[115] having K-matrix given by

$$K = \begin{pmatrix} 2 & 1 \\ 1 & 2 \end{pmatrix} \tag{5.15}$$

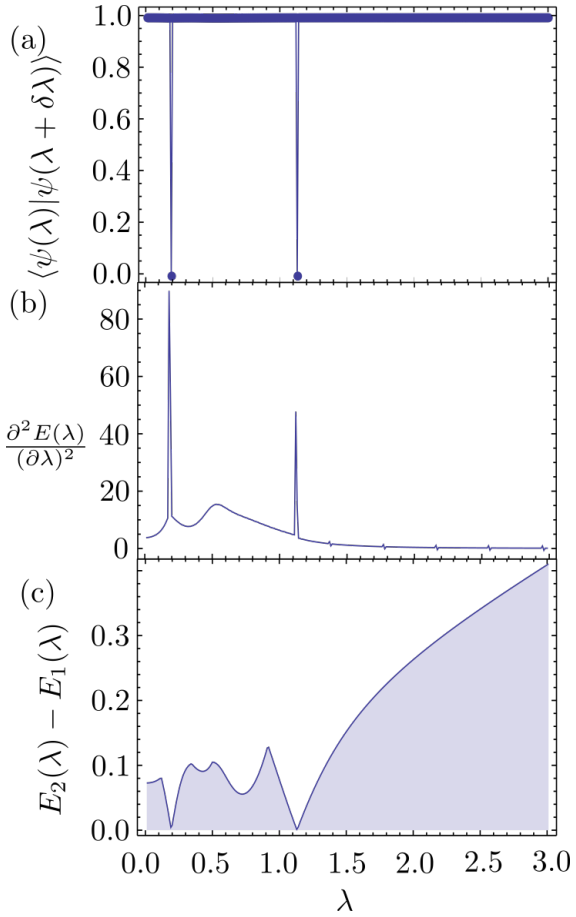

Figure 5.8: (a) Ground state fidelity and (b) fidelity susceptibility showing phase transitions as a function of λ for $\nu = 1/3$. Again the phase transition at $\lambda \sim 0.2$ is due to the instability at the edge as discussed in a later section and is expected to go away in the thermodynamic limit. (c) gap to the first excitation as a function of λ.

having Det$[K] = 3$ and eigenvalues 1 and 3 which means that the ground state is topologically ordered having 3 fold degeneracy on a 2-Torus and there are two co-propagating chiral modes[130]. Thus the behavior of its edge modes is similar to the ones of FQH states, whose effective Lagrangian is:

$$\mathcal{L} = -\frac{1}{4\pi}\left(K_{\alpha\beta}\partial_t\phi_\alpha\partial_x\phi_\beta + V_{\alpha\beta}\partial_x\phi_\alpha\partial_x\phi_\beta\right) \tag{5.16}$$

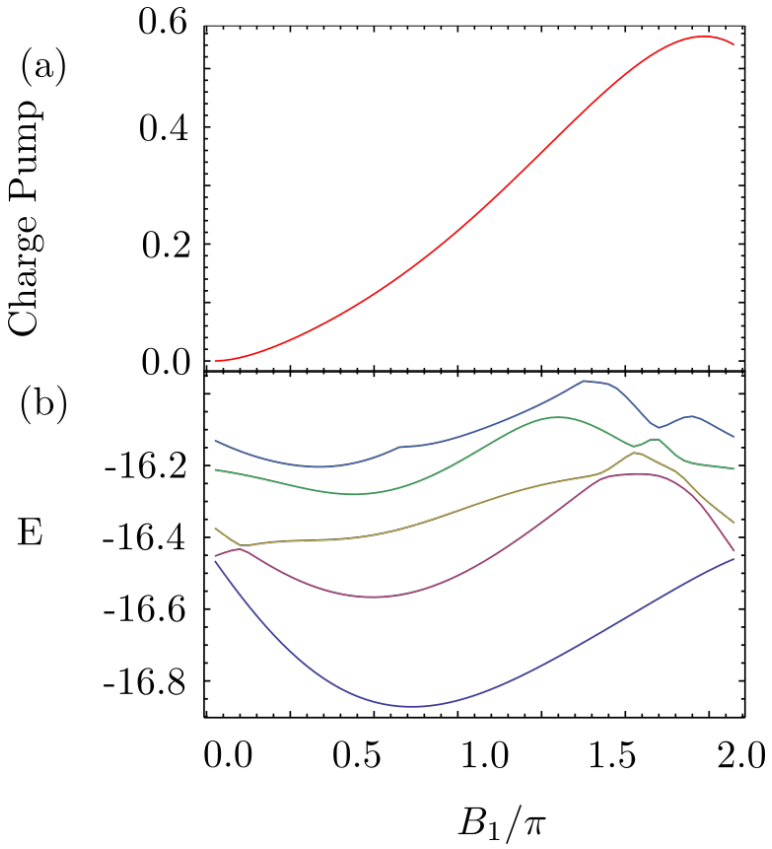

Figure 5.9: (a) Charge pump and (b) evolution of the first five states as a function of threaded flux. Charge pump of around 2/3 is the direct consequence of $\sigma_{xy} = 2/3$. It is not exactly 2/3 because edge states protrude a little into the bulk.

5.5 Stability of the First phase transition

Here we look at the stability of the "extra" phase transition happening at $\lambda \sim 0.5$ at $\nu = 1/2$ and $\lambda \sim 0.2$ at $\nu = 1/3$. We find that these are very susceptible to the variation of the nearest neighbor term on the edge while the other phase transitions are not (Fig. 5.10). This can be understood in the following way: The hopping term in the Hamiltonian with $\lambda > 0$ would like to stabilize the higher angular momentum state while the correlated hopping tries to stabilize the 0 angular momentum state. This leads to a competition between them. On the edge, the

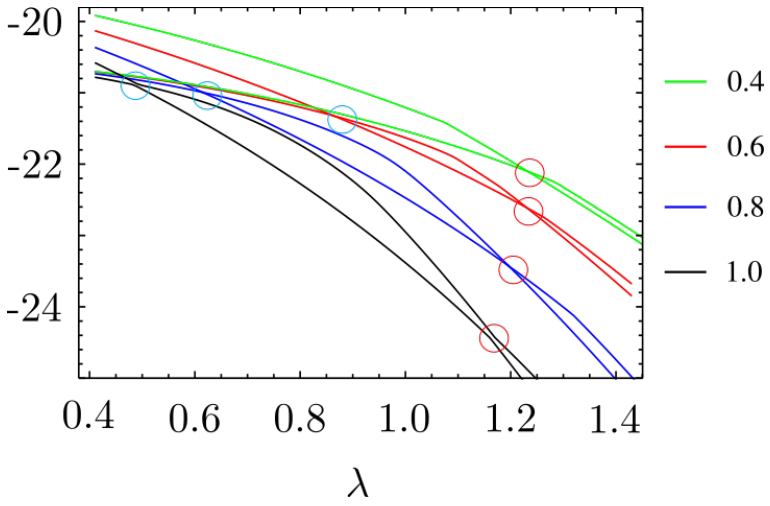

Figure 5.10: Eigen-spectrum as a function of λ for different values of NN hopping on the edge. The crossing (avoided) at $\lambda \sim 0.5$ is more susceptible to the perturbation on the edge (marked by blue circles) compared to the crossing (avoided) at $\lambda \sim 1.2$ (marked by red circles).

effectiveness of nearest neighbor hopping increases over the correlated hopping (because of the broken bonds on the boundary)[4], and leads to instability on the edge to stabilize the higher angular momentum state even though the bulk still has a stable 0 angular momentum state.

5.6 Conclusions

In summary, we have presented numerical evidence for the presence of integer as well as fractional quantum Hall effect of bosons on a honeycomb lattice with the nearest neighbor and correlated next nearest neighbor hopping in the presence of π flux per hexagon. We found the presence of a unique ground state for fillings $\nu = 1/2, 1/3$ in the Hamiltonian in Eq. 5.2. We also verified the presence of low energy edge excitations with degeneracies in agreement with the edge theory. Furthermore, we performed the flux threading experiment to measure the charge

[4]In the bulk, there are six NNN and three NN bonds, while on the edge, there are only 3-4 NNN bonds (depending upon the edge site) but there are 2-3 NN bonds. So, effectively NN hopping fraction increases on the surface and the phase transition on the edge occurs before the phase transition in the bulk.

pumping to the surface as a function of the threaded flux.

6

Conclusion and future outlook

Here we first summarize the results presented in the previous Chapters and then we discuss some relevant future directions on these topics.

We started this thesis with a broad introduction to the field of topological insulator when it was first discovered and the future development in the field, trying to keep the chronological order in mind (with some hiccups here and there). We discussed the classification of topological insulators based on Berry phase and equivalent topological quantum numbers. Then we moved on to discuss the basic concepts of field theory used in condensed matter physics while keeping in mind their relevance in the upcoming chapters.

6.1 Summary of the results

In Chapter 3, we discussed the emergence of a Z_2 type of topological order due to the development of a symmetry breaking field (spin-orbit density wave, SODW) in the system. A quasi 1D system with a strong Rashba SOC tends to get unstable towards a SODW ground state. We showed that at a magic nesting of $Q = (\pi, 0)/(0, \pi)$, the helicity gets inverted on different sub-lattices ($\alpha_{k+Q} = \alpha_k^*$). The resultant quantum order parameter breaks translation symmetry, but preserves time reversal symmetry and is inherently associated with a Z_2 type of topological order along each density wave direction. Hence it is a weak topological insulator in 2D with an even number of spin-polarized edge states. This phase is analogous to quantum spin-Hall state, except for the fact that the TR polarization is spatially modulated. This state should be realizable in many systems including thin atomic wires and 1D optical lattices where interaction and SOC can be tuned independently.

In Chapter 4, we discussed the unique topological and magnetic properties of an experimentally well studied magnetic material, $TlCuCl_3$. $TlCuCl_3$ has many unique properties such as a massive Higgs mode at the magnetic critical point, long-lived paramagnons and dimerized antiferromagnetic ground state. To study these properties, we performed DFT (as implemented in VASP) calculations and found the presence of an isolated dirac cone. The dirac cone is a direct consequence of the presence of a 1D chain like structures equivalent to SSH chains stacked in 3D. The SSH chains, combined with SOC, give rise to an isolated anisotropic 3D dirac cone where chiral and helical states are intertwined. As we turn on the Heisenberg interaction, we show the formation of AFM ground state. In the magnetic ground state, we also find a naturally occurring topological phase, distinguished by the axion angle. Finally, we derived a Chern-Simons-Ginzburg-Landau (CSGL) action to study the coupling of magnetic excitation and topological axion excitations. We find that the extra topological term provides an additional mass to the Higgs mode and a lifetime to paramagnons.

In Chapter 5, we performed ED studies on an interacting lattice model of bosons to explore the presence of integer as well as fractional quantum Hall effect of bosons. The model consists of hard core bosons on honeycomb lattice having π flux per unit cell with the nearest neighbor and correlated next nearest neighbor hopping. We provided preliminary evidence for the presence of integer as well as fractional quantum Hall ground state. Although the BIQH phase is an example of symmetry protected topological (SPT) phase, BFQH phase is a symmetry enriched topologically ordered state that can host fractional bosonic excitations whose signatures are revealed in a charge pumping calculation. We adiabatically insert 2π flux through the center of the system and observe a charge flow of 2/3, which is a signature that the ground state has a quantized charge conductance, $\sigma_{xy} = 2/3$. We also looked at the excitation spectrum to confirm the presence of chiral edge modes.

6.2 Outlook for future studies

The approaches discussed above can be extended to infer more testable and measurable results. Below, we discuss some natural avenues in which one can pursue this goal.

We proposed a topological transition driven by quantum phase transition in Chapter 3 in a quasi 1D system. The most straight forward generalization would be to study the same in higher dimensions i.e, in 2D and 3D. In that case, one will be required to introduce nesting along all the direction ($(\pi, 0)$ and $(0, \pi)$ in 2D and $(\pi, 0, 0), (0, \pi, 0)$ and $(0, 0, \pi)$ in 3D). This will lead to a 6×6 (8×8) Hamiltonian in 2D (3D). It would also be very interesting to study the effect of fluctuations on the top of the mean field results. Another possibility would be to study the interacting Hamiltonian presented using non-perturbative techniques such as bosonization and coupled wire construction[131, 132].

The model presented in Chapter 4 deals with axion angle, a pseudo scalar topological term along

with a single Higgs mode. This leads to axion-Higgs coupling accessible within the prepared CSGL term. The corresponding Lagrangian shares some common features with the Standard Model of particle physics. In the case of a Higgs doublet, an axion-Higgs cross term arises in the Lagrangian which breaks the CSGL symmetry and leads to a so-called Peccei-Quinn (PQ) symmetry, which violates the Standard model[112, 113]. However, the predicted Higgs doublet is yet to be observed. This could be a very fruitful study as the real material hosts two Higgs mode. It will also be interesting to derive an analytical expression for the θ term near the phase transition. Again, it will be interesting to see the effect of fluctuations on top of the mean field analysis presented, especially how the topological axion term affects the critical exponents.

Although we have provided preliminary evidence for BIQHE and BFQHE in Chapter 5, we would like to resolve the issue of phase transition happening while threading the flux through the central hexagon. Apart from that, the correlated hopping plays an essential role in stabilizing BIQHE and BFQHE (which naively can be thought of as a mutual flux attachment). It will be interesting to see if this kind of correlated hopping can stabilize other SPT and non-SPT phases such as phases with $\sigma_{xy} = \pm 4, \pm 4/3, ..$ by adding more complicated background gauge flux and/or different fillings. Another interesting possibility would be to study the competition between different BQHE phases or between the BQHE phase and topologically trivial phases as it is known that some repulsive interaction in the present model can lead to a topologically trivial Mott phase[133, 134]. It will also be very interesting to develop a microscopic theory for general filling apart from the perturbative approach.

A

Pancharatnam phase or Berry phase

In this Appendix, we will derive the Berry phase expressions and related quantities. We start with a time-varying Hamiltonian $\mathcal{H}(\mathbf{R}(\mathbf{t}))$ with

$$\mathcal{H}(\mathbf{R})|n(\mathbf{R})\rangle = \mathcal{E}_n(\mathbf{R})|n(\mathbf{R})\rangle \tag{A.1}$$

where $\mathbf{R}(\mathbf{t})$ is a (vector) time-dependent parameter of the Hamiltonian and $|n(\mathbf{R})\rangle$ is the instantaneous eigenstate of $\mathcal{H}(\mathbf{R})$. The requirement is that the adiabaticity should be followed, i.e., the rate of change of the Hamiltonian should be much slower than the gap in the system[1]. The time evolution of the system is given by

$$\mathcal{H}(\mathbf{R})|\psi(t)\rangle = i\hbar\frac{d}{dt}|\psi(t)\rangle \tag{A.2}$$

[1] this means that the system need to have finite gap for excitations

for $|\psi(t)\rangle = e^{-i\phi(t)}|n(\mathbf{R}(t))\rangle$, the above equation becomes

$$\mathcal{E}_n(\mathbf{R})|n(\mathbf{R})\rangle = \hbar\left(\frac{d}{dt}\phi(t)\right)|n(\mathbf{R})\rangle + i\hbar\frac{d}{dt}|n(\mathbf{R})\rangle \tag{A.3}$$

hitting the above Eq. with $\langle n(\mathbf{R})|$ we get

$$\mathcal{E}_n(\mathbf{R}) - i\hbar\langle n(\mathbf{R})|\frac{d}{dt}|n(\mathbf{R})\rangle = \hbar\left(\frac{d}{dt}\phi(t)\right) \tag{A.4}$$

we can now solve for ϕ by integrating the above equation

$$\phi(t) = \frac{1}{\hbar}\int_0^t \mathcal{E}_n(\mathbf{R}(t'))dt' - i\int_0^t \langle n(\mathbf{R}(t'))|\frac{d}{dt}|n(\mathbf{R}(t'))\rangle dt' \tag{A.5}$$

as we can easily recognize, the first part on the right of the above equation is the conventional dynamical phase while the other part is the negative of the Berry phase[1]. We can now write

$$|\psi(t)\rangle = exp\left(-\frac{i}{\hbar}\int_0^t \mathcal{E}_n(\mathbf{R}(t'))dt'\right) exp\left(i\gamma_n\right)|n(\mathbf{R}(t))\rangle \tag{A.6}$$

where

$$\gamma_n = i\int_0^t \langle n(\mathbf{R}(t'))|\frac{d}{dt'}|n(\mathbf{R}(t'))\rangle dt' \tag{A.7}$$

[1]in-spite of having an i, berry phase is a real number because $\langle n(\mathbf{R})|\frac{d}{dt}|n(\mathbf{R})\rangle$ is always imaginary

which over a closed cycle, becomes

$$\gamma_n = i\int_0^{t_{closed\_cycle}} \langle n(\mathbf{R}(t'))|\nabla_{\mathbf{R}}|n(\mathbf{R}(t'))\rangle \frac{d\mathbf{R}}{dt'}dt' = i\int_{\mathcal{C}} \langle n(\mathbf{R})|\nabla_{\mathbf{R}}|n(\mathbf{R})\rangle d\mathbf{R} \tag{A.8}$$

the above equation can also be written as

$$\gamma_n = \int_{\mathcal{C}} d\mathbf{R}.\mathcal{A}_n(\mathbf{R}) \tag{A.9}$$

where $\mathcal{A}_n(\mathbf{R}) = i\langle n(\mathbf{R})|\nabla_{\mathbf{R}}|n(\mathbf{R})\rangle$ is called the Berry connection or Berry vector potential (analogous to the electromagnetic vector potential)[2]. Since the Berry phase is a real number, we can write the above equation as

$$\gamma_n = -Im\int_{\mathcal{C}} \langle n(\mathbf{R})|\nabla_{\mathbf{R}}|n(\mathbf{R})\rangle \tag{A.10}$$

applying Stokes theorem to the above equation gives

$$\gamma_n = -Im\int d\mathbf{S}.\left(\nabla \times \langle n(\mathbf{R})|\nabla_{\mathbf{R}}|n(\mathbf{R}\rangle\right) = -Im\int d\mathbf{S}.\left(\langle\nabla n(\mathbf{R})| \times |\nabla n(\mathbf{R}\rangle\right) \tag{A.11}$$

where $\langle\nabla n(\mathbf{R})| \times |\nabla n(\mathbf{R})\rangle$ is the Berry curvature.

[2]it should be noted that although the Berry phase is a gauge invariant quantity, one needs to fix the gauge for numerical calculations which, sometimes, becomes hard. For better understanding, one should consult the dedicated references such as B.A. Bernevig[36].

B

Ginzburg-Landau Theory

In this Appendix, we will derive the Ginzburg-Landau free energy functional discussed in Chapter 2. Since the free energy changes continuously near the transition point, we can expand it (Eq. 2.10) for small Δ. The inverse of the Greens function can be written as

$$\hat{\mathcal{G}}^{-1} = \hat{\mathcal{G}}_0^{-1}\left[1 + \hat{\mathcal{G}}_0\begin{pmatrix} 0 & \Delta \\ \bar{\Delta} & 0 \end{pmatrix}\right] \tag{B.1}$$

where $\hat{\mathcal{G}}_0 \equiv \hat{\mathcal{G}}(\Delta = 0)$ is the non-interacting greens function. Now we can expand ln det $(\mathcal{G}^{-1}[\Delta])$ (using the identity ln det(A)= tr ln(A)[1]) as

[1]this can be easily shown by going to the diagonal basis of A, i.e., ln det(A)=ln det(A_D)=ln $\Pi_i\lambda_i = \sum_i \ln\lambda_i =$ tr ln $A_D =$ tr ln A

$$\ln\det\hat{\mathcal{G}}^{-1} = \text{tr}\ln\hat{\mathcal{G}}^{-1} = \text{tr}\ln\hat{\mathcal{G}}_0^{-1} - \frac{1}{2}\text{tr}\left[\hat{\mathcal{G}}_0\begin{pmatrix}0 & \Delta\\ \bar{\Delta} & 0\end{pmatrix}\right]^2 + \ldots \tag{B.2}$$

the first term in the above equation is the contribution of the non-interacting part. Using the identity

$$\begin{aligned}\mathbb{1} &= \sum_{k\equiv\mathbf{k},\omega_n}|k\rangle\langle k|,\\ \Delta_k &= \frac{1}{\sqrt{\beta L^d}}\int dx e^{ik.x}\Delta(x)\end{aligned}$$

the second term can be written as

$$\begin{aligned}\text{tr}\,\hat{G}_0^{(p)}\Delta\hat{G}_0^{(h)}\bar{\Delta} &= \sum_{k,k'}G_0^{(p)}(k)\langle k|\Delta|k'\rangle G_0^{(h)}(k')\langle k'|\bar{\Delta}|k\rangle\\ &\overset{q=k-k'}{=} \sum_q\Delta_q\bar{\Delta}_{-q}\frac{1}{\beta L^d}\sum_k G_0^{(p)}(k)G_0^{(h)}(k+q)\end{aligned} \tag{B.3}$$

which on combining with the non-interacting term, we get

$$\begin{aligned}\mathcal{Z} &= \int D\left[\bar{\Delta},\Delta\right]e^{-\mathcal{S}\left[\bar{\Delta},\Delta\right]}\\ \mathcal{S}\left[\bar{\Delta},\Delta\right] &= \sum_{\omega_n,q}\left[\frac{1}{g}+\Pi(\omega_n.q)\right]|\Delta_{\omega_n,q}|^2+\mathcal{O}(\Delta^4)\end{aligned} \tag{B.4}$$

where

$$\Pi(\omega_n.q) = \frac{1}{\beta L^d}\sum_k G_0^{(p)}(k)G_0^{(h)}(k+q)$$

now, one can do the gradient expansion of $\Pi(\omega_n,q)$ as

$$\Pi(\omega_n,q) = \Pi(0,0)+\frac{q^2}{2}\partial_q^2\Pi(\omega_n,q)|_{(0,0)}+\mathcal{O}(\omega_n,q^4) \tag{B.5}$$

which gives

$$\mathcal{S}[\Delta] = \int d^d r \left[b|\Delta|^2 + K|\partial\Delta|^2 + d|\Delta|^4 + \dots \right] \tag{B.6}$$

where $b = 1/2g + \Pi(0,0)/2$, $K = \lim_{q\to 0} \partial_q^2 \Pi(q,0)/2 > 0$ and $d > 0$. The effective free energy functional is given by

$$\begin{aligned} \mathcal{F}[\Delta] &= -k_\beta T \ln\, e^{-\mathcal{S}[\Delta]} \\ \mathcal{F}[\Delta] &= k_B T \mathcal{S}[\Delta] = k_B T \int d^d r \left[b|\Delta|^2 + K|\partial\Delta|^2 + d|\Delta|^4 + \dots \right] \end{aligned} \tag{B.7}$$

this is the famous Ginzburg-Landau free energy functional.

C

Derivation of the order parameter

The order parameter discussed in Chapter 3 can possibly arise from many types of interaction, here we have shown some cases [1] from where these order parameters can arise. Let's start with the most common approximation of the Coulomb interaction, the Hubbard interaction.

C.1 Hubbard Interaction

$$H_{\text{int}} = \frac{U}{N}\sum_i n_{i\uparrow}n_{i\downarrow} = \frac{U}{N}\sum_i c^\dagger_{i\uparrow}c_{i\uparrow}c^\dagger_{i\downarrow}c_{i\downarrow}, \tag{C.1}$$

[1] these are commonly used interactions in condensed matter physics

where i, j are the site index and N is the total number of sites. Taking the Fourier transformation to the momentum space, we get

$$\begin{aligned} H_{\text{int}} &= \frac{U}{N}\sum_i \left(\frac{1}{N^2} \sum_{k,k',k'',k'''} e^{i(\mathbf{k}-\mathbf{k}'+\mathbf{k}''-\mathbf{k}''').\mathbf{r}_i} c^\dagger_{k\uparrow} c_{k'\uparrow} c^\dagger_{k''\downarrow} c_{k'''\downarrow} \right), \\ &= \frac{U}{N^2} \sum_{k,k',k''} c^\dagger_{k\uparrow} c_{k'\uparrow} c^\dagger_{k''\downarrow} c_{k'''\downarrow} \Big|_{k'''=k-k'+k''} \end{aligned} \tag{C.2}$$

(1) For $k' = k$, and $k'' = k + Q$ we get

$$H^1_{\text{int}} = g \sum_k c^\dagger_{k\uparrow} c_{k\uparrow} c^\dagger_{k+Q\downarrow} c_{k+Q\downarrow}, \tag{C.3}$$

where $g = U/N^2$. Using the fermionic anti-commutation relations we can rearrange the operators in H_{int} to get

$$H^1_{\text{int}} = g \sum_k \left(c^\dagger_{k\uparrow} c_{k\uparrow} - c^\dagger_{k\uparrow} c_{k+Q\downarrow} c^\dagger_{k+Q\downarrow} c_{k\uparrow} \right). \tag{C.4}$$

The first term gives the Hartee interaction which is neglected here (usually density-functional theory based calculation incorporates this term). Expanding the Hamiltonian in terms of the mean-field order parameter Δ_1, we get

$$\begin{aligned} H^1_{\text{int}} &= -g \sum_k \Big(\langle c^\dagger_{k\uparrow} c_{k+Q\downarrow} \rangle c^\dagger_{k+Q\downarrow} c_{k\uparrow} \\ &\quad + c^\dagger_{k\uparrow} c_{k+Q\downarrow} \langle c^\dagger_{k+Q\downarrow} c_{k\uparrow} \rangle - \langle c^\dagger_{k\uparrow} c_{k+Q\downarrow} \rangle \langle c^\dagger_{k+Q\downarrow} c_{k\uparrow} \rangle \Big). \end{aligned} \tag{C.5}$$

(2) If we take $k'$and k''=$k + Q$ in Eq. (S2), we get

$$H^2_{\text{int}} = g \sum_k c^\dagger_{k\uparrow} c_{k+Q\uparrow} c^\dagger_{k+Q\downarrow} c_{k\downarrow}, \tag{C.6}$$

Expanding the Hamiltonian in terms of the mean-field order parameter Δ_2, we get

$$H^2_{\text{int}} = g\sum_k \Big(\langle c^\dagger_{k\uparrow}c_{k+Q\uparrow}\rangle c^\dagger_{k+Q\downarrow}c_{k\downarrow} + c^\dagger_{k\uparrow}c_{k+Q\uparrow}\langle c^\dagger_{k+Q\downarrow}c_{k\downarrow}\rangle - \langle c^\dagger_{k\uparrow}c_{k+Q\uparrow}\rangle\langle c^\dagger_{k+Q\downarrow}c_{k\downarrow}\rangle\Big). \tag{C.7}$$

C.2 Heisenberg Interaction

$$H_{\text{int}} = JS_i.S_j, \tag{C.8}$$

where i, j are site index and

$$\begin{aligned}
\vec{S}_i &= c^\dagger_i\vec{\sigma}c_i,\\
S_{ix} &= c^\dagger_{i\uparrow}c_{i\downarrow} + c^\dagger_{i\downarrow}c_{i\uparrow},\\
S_{iy} &= -i\left(c^\dagger_{i\uparrow}c_{i\downarrow} - c^\dagger_{i\downarrow}c_{i\uparrow}\right),\\
S_{iz} &= c^\dagger_{i\uparrow}c_{i\uparrow} - c^\dagger_{i\downarrow}c_{i\downarrow},
\end{aligned} \tag{C.9}$$

This gives

$$H_{\text{int}} = J(2c^\dagger_{i\uparrow}c_{i\downarrow}c^\dagger_{j\downarrow}c_{j\uparrow} + 2c^\dagger_{i\downarrow}c_{i\uparrow}c^\dagger_{j\uparrow}c_{j\downarrow} - c^\dagger_{i\uparrow}c_{i\uparrow}c^\dagger_{j\downarrow}c_{j\downarrow} - c^\dagger_{i\downarrow}c_{i\downarrow}c^\dagger_{j\uparrow}c_{j\uparrow}), \tag{C.10}$$

as seen in the Hubbard term, the above terms will also lead to similar terms on taking the Fourier transformation and hence leads to similar type of order parameter.

C.3 Hund's Coupling

$$H_{\rm int} = J_H S_i^{\alpha}.S_j^{\beta}, \tag{C.11}$$

where α, β are band indices and i, j are the site indices. Since Hund's coupling is very much similar to Heisenberg interaction hence this will also lead to similar type of order parameters.

D

Self-consistent gap equations

In this section we will show how the two gap terms ($\Delta_{1,2}$) changes with the interaction strength by solving for them self-consistently. The mean-field Hamiltonians corresponding to the two order parameters are

$$H_1 = \begin{pmatrix} \xi_k & \alpha_k & 0 & \Delta_1 \\ \alpha_k^* & \xi_k & \Delta_1 & 0 \\ 0 & \Delta_1 & \xi_{k+Q} & \alpha_k^* \\ \Delta_1 & 0 & \alpha_k & \xi_{k+Q} \end{pmatrix},$$

$$H_2 = \begin{pmatrix} \xi_k & \alpha_k & \Delta_2 & 0 \\ \alpha_k^* & \xi_k & 0 & -\Delta_2 \\ \Delta_2 & 0 & \xi_{k+Q} & \alpha_k^* \\ 0 & -\Delta_2 & \alpha_k & \xi_{k+Q} \end{pmatrix}.$$

So we can evaluate $\Delta_{1(2)}$ self-consistently by finding out the expectation value of Γ_1 (Γ_3), i.e, $\sum_n \langle n| \Gamma_1 |n\rangle$ ($\sum_n \langle n| \Gamma_3 |n\rangle$) where $|n\rangle$ are the eigenstates of H below the Fermi level. The

corresponding result is shown in Fig. D.1.

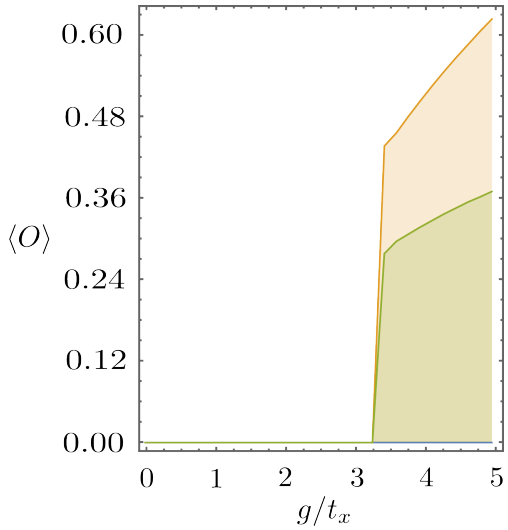

Figure D.1: We show the variation of order parameter Δ_1 and Δ_2 (defined in Eq. 1 in the main text) as a function of interaction strength g. Orange curve shows the order parameter Δ_1 while green curve shows that for Δ_2.

E

Bosonic Integer Quantum Hall

In this appendix, we will discuss the theory of Bosonic integer Quantum Hall Effect (BIQHE). Let's consider a two-component bosonic system which might be a bilayer system or a bosonic spinor for instance. In the presence of magnetic field, the Hamiltonian can be written as[114]

$$\mathcal{H} = \sum_I H_I + H_{int} \tag{E.1}$$

$$H_I = \int d^x a_I^\dagger \left(-\frac{(\vec{\nabla} - i\vec{A})^2}{2m} - \mu \right) a_I \tag{E.2}$$

$$H_{int} = \int d^2x d^2x' \rho_I(x) V_{IJ}(x - x') \rho_J(x') \tag{E.3}$$

where $a_I(a_I^\dagger)$ are the bosonic annihilation(creation) operators of species $I = 1, 2$ and $\rho_I = a_I^\dagger a_I$ is the density operator. Now we define new bosonic operators based on flux attachment Chern-

Simons theory as:

$$\tilde{a}_1(x) = e^{-i\int d^2x'\Theta(x-x')\rho_2(x')}.a_1(x) \tag{E.4}$$

$$\tilde{a}_2(x) = e^{-i\int d^2x'\Theta(x-x')\rho_1(x')}.a_2(x) \tag{E.5}$$

where $\theta(\vec{x})$ gives the angle of $\vec{x}$. This is an implementation of the flux attachment which attaches one flux quanta of one species to the other. At $\nu = 1$ filling, this cancels the externally applied field in the mean field approximation. Now, an effective Chern-Simons Ginzburg-Landau theory can be written in terms of these new bosons (composite bosons)

$$\mathcal{L} = \sum_I \mathcal{L}_I + \mathcal{L}_{int} + \mathcal{L}_{CS} \tag{E.6}$$

$$\mathcal{L}_I = i\tilde{a}_I^* \left(\partial_0 - iA_{I0} + i\alpha_{I0}\tilde{a}_I - \frac{|\vec{\nabla}\tilde{a}_I - i\left(\vec{A}_I - \vec{\alpha}_I\right)\tilde{a}_I|^2}{2m} \right) + \mu|\tilde{a}_I|^2 \tag{E.7}$$

$$\mathcal{L}_{int} = -V_{IJ}|\tilde{a}_I|^2|\tilde{a}_J|^2 \tag{E.8}$$

$$\mathcal{L}_{CS} = \frac{1}{4\pi}\epsilon^{\mu\mu\lambda}(\alpha_{1\mu}\partial_\nu\alpha_{2\lambda} + \alpha_{2\mu}\partial_\nu\alpha_{1\lambda}) \tag{E.9}$$

where two gauge fields $\alpha_{1/2}$ have been introduced to implement the flux attachment. As there is no magnetic field for composite bosons, they can condense to lock the external gauge field to the internal gauge field which gives an effective Lagrangian for the external probe field [1]

$$\mathcal{L}_{eff} = \frac{1}{4\pi}\epsilon^{\mu\nu\lambda}\left(A_{1\mu}\partial_\nu A_{2\lambda} + A_{2\mu}\partial_\nu A_{1\lambda}\right) \tag{E.10}$$

we can now introduce two new probe gauge fields

$$A_c = \frac{A_1 + A_2}{2} \tag{E.11}$$

$$A_s = \frac{A_1 - A_2}{2} \tag{E.12}$$

[1] Canceling the internal gauge field with the external gauge field in Eq. E.7 requires $A_I = \alpha_I$. Putting this in Eq. E.9 results in Eq. E.10.

which couples to the charge and pseudospin currents respectively. Now, the effective Lagrangian becomes

$$\mathcal{L}_{eff} = \frac{1}{4\pi}\epsilon^{\mu\nu\lambda}\left(A_{c\mu}\partial_\nu A_{c\lambda} - A_{s\mu}\partial_\nu A_{s\lambda}\right) \tag{E.13}$$

which represents an incompressible Quantum Hall state with Hall conductivity $\sigma^c_{xy} = +2$ and pseudospin Hall conductivity of $\sigma^s_{xy} = -2$.

F

Gauge fixing

In this appendix, we will discuss the fixing of the gauge in Chapter 5 for performing exact diagonalization. Here we choose symmetric gauge because it preserves the C_6 rotation symmetry of the system. In symmetric gauge, the vector potential looks like

$$\vec{A} = -\frac{B_0}{2}(-y, x, 0) \tag{F.1}$$

such that

$$\vec{B} = \vec{\nabla} \times \vec{A} = B_0 \hat{z} \tag{F.2}$$

where B_0 (the magnetic field strength) is chosen such that the flux through each hexagon is π. The advantage of choosing the symmetric gauge is the presence of C_6 rotation symmetry in the Hamiltonian, which helps in characterizing different eigenstates of the system (by assigning different "angular momentum" quantum number).

G

Excitation Spectrum/Edge theory

The BIQH state discussed in Chapter 5 can be described by an Abelian Chern-Simons theory with the K-matrix[7]

$$K = \begin{pmatrix} 0 & 1 \\ 1 & 0 \end{pmatrix}. \tag{G.1}$$

Thus the behavior of its edge modes is similar to the ones of FQH states, whose effective Lagrangian is:

$$\mathcal{L} = -\frac{1}{4\pi}\left(K_{\alpha\beta}\partial_t\phi_\alpha\partial_x\phi_\beta + V_{\alpha\beta}\partial_x\phi_\alpha\partial_x\phi_\beta\right) \tag{G.2}$$

where $\alpha, \beta = A, B$ and $(1/2\pi)\partial_x\phi_\alpha$ gives the density of the corresponding species of bosons, and $V_{\alpha\beta}$ is the velocity matrix. To diagonalize the above Lagrangian, we introduce the charge and (pseudo) spin modes $\phi_{c(s)} = \left(\phi_a \pm \phi_b\right)/\sqrt{2}$

We can now obtain the edge Hamiltonian and the corresponding momentum operator:

$$H = \frac{2\pi}{L_y}\left(v_c L_0^c + v_s L_0^s\right), and \tag{G.3}$$

$$P = \frac{2\pi}{L_y}(L_0^c - L_0^s) \tag{G.4}$$

with

$$L_0^{c(s)} = \frac{\left(\Delta N_a \pm \Delta N_b\right)^2}{4} + \sum_{m=1}^{\infty} m n_m^{c(s)} \tag{G.5}$$

Here,L_y is the length of the 1D edge; $\Delta N_{a(b)}$ is the change in the particle number of $a(b)$ boson relative to the ground state;$n_m^{c(s)}$ is the set of non-negative integers describing oscillator modes. These oscillator modes exhibit the well-known 1, 1, 2, 3,... degeneracy pattern.

Bibliography

[1] K. v. Klitzing, G. Dorda, and M. Pepper. New method for high-accuracy determination of the fine-structure constant based on quantized hall resistance. *Phys. Rev. Lett.*, 45:494–497, Aug 1980.

[2] Tanmoy Das. Imprints of spin-orbit density wave in the hidden-order state of uru_2si_2. *Phys. Rev. B*, 89:045135, Jan 2014.

[3] C Brand, Herbert Pfnür, G Landolt, S Muff, JH Dil, Tanmoy Das, and Christoph Tegenkamp. Observation of correlated spin–orbit order in a strongly anisotropic quantum wire system. *Nature communications*, 6:8118, 2015.

[4] Tanmoy Das. Interaction induced staggered spin-orbit order in two-dimensional electron gas. *Phys. Rev. Lett.*, 109:246406, Dec 2012.

[5] Ch. Rüegg, B. Normand, M. Matsumoto, A. Furrer, D. F. McMorrow, K. W. Krämer, H. U. Güdel, S. N. Gvasaliya, H. Mutka, and M. Boehm. Quantum magnets under pressure: Controlling elementary excitations in $\mathrm{tlcucl_3}$. *Phys. Rev. Lett.*, 100:205701, May 2008.

[6] P Merchant, B Normand, KW Krämer, M Boehm, DF McMorrow, and Ch Rüegg. Quantum and classical criticality in a dimerized quantum antiferromagnet. *Nature physics*,

10(5):373, 2014.

[7] Yin-Chen He, Subhro Bhattacharjee, R. Moessner, and Frank Pollmann. Bosonic integer quantum hall effect in an interacting lattice model. *Phys. Rev. Lett.*, 115:116803, Sep 2015.

[8] Paul M Chaikin and Tom C Lubensky. *Principles of condensed matter physics*, volume 1. Cambridge university press Cambridge, 1995.

[9] Lev Davidovich Landau. On the theory of phase transitions. *Ukr. J. Phys.*, 11:19–32, 1937.

[10] Chetan Nayak, Steven H Simon, Ady Stern, Michael Freedman, and Sankar Das Sarma. Non-abelian anyons and topological quantum computation. *Reviews of Modern Physics*, 80(3):1083, 2008.

[11] A Yu Kitaev. Fault-tolerant quantum computation by anyons. *Annals of Physics*, 303(1):2–30, 2003.

[12] D. J. Thouless, M. Kohmoto, M. P. Nightingale, and M. den Nijs. Quantized hall conductance in a two-dimensional periodic potential. *Phys. Rev. Lett.*, 49:405–408, Aug 1982.

[13] Barry Simon. Holonomy, the quantum adiabatic theorem, and berry's phase. *Phys. Rev. Lett.*, 51:2167–2170, Dec 1983.

[14] F. D. M. Haldane. Model for a quantum hall effect without landau levels: Condensed-matter realization of the "parity anomaly". *Phys. Rev. Lett.*, 61:2015–2018, Oct 1988.

[15] C. L. Kane and E. J. Mele. Z_2 topological order and the quantum spin hall effect. *Phys. Rev. Lett.*, 95:146802, Sep 2005.

[16] J. E. Moore and L. Balents. Topological invariants of time-reversal-invariant band structures. *Phys. Rev. B*, 75:121306, Mar 2007.

[17] Liang Fu, C. L. Kane, and E. J. Mele. Topological insulators in three dimensions. *Phys. Rev. Lett.*, 98:106803, Mar 2007.

[18] Rahul Roy. Topological phases and the quantum spin hall effect in three dimensions. *Phys. Rev. B*, 79:195322, May 2009.

[19] Yuqi Xia, Dong Qian, David Hsieh, L Wray, Arijeet Pal, Hsin Lin, Arun Bansil, DHYS Grauer, Yew San Hor, Robert Joseph Cava, et al. Observation of a large-gap topological-insulator class with a single dirac cone on the surface. *Nature physics*, 5(6):398, 2009.

[20] Y. L. Chen, J. G. Analytis, J.-H. Chu, Z. K. Liu, S.-K. Mo, X. L. Qi, H. J. Zhang, D. H. Lu, X. Dai, Z. Fang, S. C. Zhang, I. R. Fisher, Z. Hussain, and Z.-X. Shen. Experimental realization of a three-dimensional topological insulator, bi2te3. *Science*, 325(5937):178–181, 2009.

[21] J Von Neumann. J. von neumann and e. wigner, phys. z. 30, 467 (1929). *Phys. Z.*, 30:467, 1929.

[22] Xiao-Liang Qi, Taylor L Hughes, and Shou-Cheng Zhang. Topological field theory of time-reversal invariant insulators. *Physical Review B*, 78(19):195424, 2008.

[23] Alexander Altland and Ben D Simons. *Condensed matter field theory*. Cambridge University Press, 2010.

[24] Nigel Goldenfeld. Lectures on phase transitions and the renormalization group. 2018.

[25] SHUN-QING. SHEN. *TOPOLOGICAL INSULATORS: Dirac Equation in Condensed Matter*. SPRINGER, 2017.

[26] Alekseĭ Alekseevich Abrikosov, Lev Petrovich Gorkov, and Igor Ekhielevich Dzyaloshinski. *Methods of quantum field theory in statistical physics*. Courier Corporation, 2012.

[27] Roger S. K. Mong, Andrew M. Essin, and Joel E. Moore. Antiferromagnetic topological insulators. *Phys. Rev. B*, 81:245209, Jun 2010.

[28] S. Raghu, Xiao-Liang Qi, C. Honerkamp, and Shou-Cheng Zhang. Topological mott insulators. *Phys. Rev. Lett.*, 100:156401, Apr 2008.

[29] Maxim Dzero, Kai Sun, Victor Galitski, and Piers Coleman. Topological kondo insulators. *Phys. Rev. Lett.*, 104:106408, Mar 2010.

[30] Andreas P. Schnyder, Shinsei Ryu, Akira Furusaki, and Andreas W. W. Ludwig. Classification of topological insulators and superconductors in three spatial dimensions. *Phys. Rev. B*, 78:195125, Nov 2008.

[31] N. Read and Dmitry Green. Paired states of fermions in two dimensions with breaking of parity and time-reversal symmetries and the fractional quantum hall effect. *Phys. Rev. B*, 61:10267–10297, Apr 2000.

[32] A Yu Kitaev. Unpaired majorana fermions in quantum wires. *Physics-Uspekhi*, 44(10S):131, 2001.

[33] Edwin H Hall. On a new action of the magnet on electric currents. *American Journal of Mathematics*, 2(3):287–292, 1879.

[34] J. E. Avron, R. Seiler, and B. Simon. Homotopy and quantization in condensed matter physics. *Phys. Rev. Lett.*, 51:51–53, Jul 1983.

[35] Gerald D Mahan. *Many-particle physics*. Springer Science & Business Media, 2013.

[36] B Andrei Bernevig and Taylor L Hughes. *Topological insulators and topological superconductors*. Princeton university press, 2013.

[37] B. I. Halperin. Quantized hall conductance, current-carrying edge states, and the existence of extended states in a two-dimensional disordered potential. *Phys. Rev. B*, 25:2185–2190, Feb 1982.

[38] R. B. Laughlin. Quantized hall conductivity in two dimensions. *Phys. Rev. B*, 23:5632–5633, May 1981.

[39] Xiao-Liang Qi, Yong-Shi Wu, and Shou-Cheng Zhang. General theorem relating the bulk topological number to edge states in two-dimensional insulators. *Phys. Rev. B*, 74:045125, Jul 2006.

[40] Yasuhiro Hatsugai. Edge states in the integer quantum hall effect and the riemann surface of the bloch function. *Phys. Rev. B*, 48:11851–11862, Oct 1993.

[41] Yasuhiro Hatsugai. Chern number and edge states in the integer quantum hall effect. *Phys. Rev. Lett.*, 71:3697–3700, Nov 1993.

[42] Roger S. K. Mong and Vasudha Shivamoggi. Edge states and the bulk-boundary correspondence in dirac hamiltonians. *Phys. Rev. B*, 83:125109, Mar 2011.

[43] Lukasz Fidkowski, T. S. Jackson, and Israel Klich. Model characterization of gapless edge modes of topological insulators using intermediate brillouin-zone functions. *Phys. Rev. Lett.*, 107:036601, Jul 2011.

[44] J. C. Solem and L. C. Biedenharn. Understanding geometrical phases in quantum mechanics: An elementary example. *Foundations of Physics*, 23(2):185–195, Feb 1993.

[45] S. Pancharatnam. Generalized theory of interference, and its applications. *Proceedings of the Indian Academy of Sciences - Section A*, 44(5):247–262, Nov 1956.

[46] and and and. Studies of the jahn-teller effect .ii. the dynamical problem. *Proceedings of the Royal Society of London A: Mathematical, Physical and Engineering Sciences*, 244(1236):1–16, 1958.

[47] Michael Victor Berry. Quantal phase factors accompanying adiabatic changes. *Proc. R. Soc. Lond. A*, 392(1802):45–57, 1984.

[48] W. P. Su, J. R. Schrieffer, and A. J. Heeger. Solitons in polyacetylene. *Phys. Rev. Lett.*, 42:1698–1701, Jun 1979.

[49] George Gruner. *Density waves in solids*. CRC Press, 2018.

[50] Markus König, Steffen Wiedmann, Christoph Brüne, Andreas Roth, Hartmut Buhmann, Laurens W. Molenkamp, Xiao-Liang Qi, and Shou-Cheng Zhang. Quantum spin hall insulator state in hgte quantum wells. *Science*, 318(5851):766–770, 2007.

[51] B. Andrei Bernevig, Taylor L. Hughes, and Shou-Cheng Zhang. Quantum spin hall effect and topological phase transition in hgte quantum wells. *Science*, 314(5806):1757–1761, 2006.

[52] Frank Wilczek. Magnetic flux, angular momentum, and statistics. *Phys. Rev. Lett.*, 48:1144–1146, Apr 1982.

[53] Xiao-Liang Qi, Rundong Li, Jiadong Zang, and Shou-Cheng Zhang. Inducing a magnetic monopole with topological surface states. *Science*, 323(5918):1184–1187, 2009.

[54] A. Bansil, Hsin Lin, and Tanmoy Das. Colloquium: Topological band theory. *Rev. Mod. Phys.*, 88:021004, Jun 2016.

[55] Xiao-Liang Qi and Shou-Cheng Zhang. Topological insulators and superconductors. *Rev. Mod. Phys.*, 83:1057–1110, Oct 2011.

[56] M. Z. Hasan and C. L. Kane. Colloquium: Topological insulators. *Rev. Mod. Phys.*, 82:3045–3067, Nov 2010.

[57] S. Raghu, Xiao-Liang Qi, C. Honerkamp, and Shou-Cheng Zhang. Topological mott insulators. *Phys. Rev. Lett.*, 100:156401, Apr 2008.

[58] Roger S. K. Mong, Andrew M. Essin, and Joel E. Moore. Antiferromagnetic topological insulators. *Phys. Rev. B*, 81:245209, Jun 2010.

[59] Maxim Dzero, Kai Sun, Victor Galitski, and Piers Coleman. Topological kondo insulators. *Phys. Rev. Lett.*, 104:106408, Mar 2010.

[60] Jian Li, Rui-Lin Chu, J. K. Jain, and Shun-Qing Shen. Topological anderson insulator. *Phys. Rev. Lett.*, 102:136806, Apr 2009.

[61] Roger S. K. Mong, Andrew M. Essin, and Joel E. Moore. Antiferromagnetic topological insulators. *Phys. Rev. B*, 81:245209, Jun 2010.

[62] Ivan Knez, Rui-Rui Du, and Gerard Sullivan. Evidence for helical edge modes in inverted $\mathrm{InAs/GaSb}$ quantum wells. *Phys. Rev. Lett.*, 107:136603, Sep 2011.

[63] Jeffrey C. Y. Teo, Liang Fu, and C. L. Kane. Surface states and topological invariants in three-dimensional topological insulators: Application to $\mathrm{bi}_{1-x}\mathrm{sb}_x$. *Phys. Rev. B*, 78:045426, Jul 2008.

[64] David Hsieh, Dong Qian, Lewis Wray, YuQi Xia, Yew San Hor, Robert Joseph Cava, and M Zahid Hasan. A topological dirac insulator in a quantum spin hall phase. *Nature*, 452(7190):970, 2008.

[65] Haijun Zhang, Chao-Xing Liu, Xiao-Liang Qi, Xi Dai, Zhong Fang, and Shou-Cheng Zhang. Topological insulators in bi 2 se 3, bi 2 te 3 and sb 2 te 3 with a single dirac cone on the surface. *Nature physics*, 5(6):438, 2009.

[66] Yuqi Xia, Dong Qian, David Hsieh, L Wray, Arijeet Pal, Hsin Lin, Arun Bansil, DHYS Grauer, Yew San Hor, Robert Joseph Cava, et al. Observation of a large-gap topological-insulator class with a single dirac cone on the surface. *Nature physics*, 5(6):398, 2009.

[67] Y. L. Chen, J. G. Analytis, J.-H. Chu, Z. K. Liu, S.-K. Mo, X. L. Qi, H. J. Zhang, D. H. Lu, X. Dai, Z. Fang, S. C. Zhang, I. R. Fisher, Z. Hussain, and Z.-X. Shen. Experimental realization of a three-dimensional topological insulator, bi2te3. *Science*, 325(5937):178–181, 2009.

[68] Juan Jiang, Sheng Li, Tong Zhang, Zhe Sun, Fei Chen, ZR Ye, Min Xu, QQ Ge, SY Tan, XH Niu, et al. Observation of possible topological in-gap surface states in the kondo insulator smb 6 by photoemission. *Nature communications*, 4:3010, 2013.

[69] Tay-Rong Chang, Tanmoy Das, Peng-Jen Chen, Madhab Neupane, Su-Yang Xu, M. Zahid Hasan, Hsin Lin, Horng-Tay Jeng, and A. Bansil. Two distinct topological phases in the mixed-valence compound ybb_6 and its differences from smb_6. *Phys. Rev. B*, 91:155151, Apr 2015.

[70] G. Grüner. The dynamics of charge-density waves. *Rev. Mod. Phys.*, 60:1129–1181, Oct 1988.

[71] G. Grüner. The dynamics of spin-density waves. *Rev. Mod. Phys.*, 66:1–24, Jan 1994.

[72] Tanmoy Das. Interaction induced staggered spin-orbit order in two-dimensional electron gas. *Phys. Rev. Lett.*, 109:246406, Dec 2012.

[73] C. Tegenkamp, D. Lükermann, H. Pfnür, B. Slomski, G. Landolt, and J. H. Dil. Fermi nesting between atomic wires with strong spin-orbit coupling. *Phys. Rev. Lett.*, 109:266401, Dec 2012.

[74] Hendrik Bentmann, Samir Abdelouahed, Mattia Mulazzi, Jürgen Henk, and Friedrich Reinert. Direct observation of interband spin-orbit coupling in a two-dimensional electron

system. *Phys. Rev. Lett.*, 108:196801, May 2012.

[75] D. W. Wang, A. J. Millis, and S. Das Sarma. Where is the luttinger liquid in one-dimensional semiconductor quantum wire structures? *Phys. Rev. Lett.*, 85:4570–4573, Nov 2000.

[76] Ch. Rüegg, A. Furrer, D. Sheptyakov, Th. Strässle, K. W. Krämer, H.-U. Güdel, and L. Mélési. Pressure-induced quantum phase transition in the spin-liquid $\mathrm{TlCucl_3}$. *Phys. Rev. Lett.*, 93:257201, Dec 2004.

[77] Thierry Giamarchi, Christian Rüegg, and Oleg Tchernyshyov. Bose–einstein condensation in magnetic insulators. *Nature Physics*, 4(3):198, 2008.

[78] O. Vyaselev, M. Takigawa, A. Vasiliev, A. Oosawa, and H. Tanaka. Field-induced magnetic order and simultaneous lattice deformation in $\mathrm{tlcucl_3}$. *Phys. Rev. Lett.*, 92:207202, May 2004.

[79] S Sachdev. Quantum phase transitions cambridge univ. *Press Cambridge Google Scholar*, 1999.

[80] Ch Rüegg, N Cavadini, A Furrer, H-U Güdel, Karl Krämer, H Mutka, A Wildes, K Habicht, and P Vorderwisch. Bose–einstein condensation of the triplet states in the magnetic insulator tlcucl 3. *Nature*, 423(6935):62, 2003.

[81] T. Nikuni, M. Oshikawa, A. Oosawa, and H. Tanaka. Bose-einstein condensation of dilute magnons in $\mathrm{tlcucl_3}$. *Phys. Rev. Lett.*, 84:5868–5871, Jun 2000.

[82] Masashige Matsumoto, B. Normand, T. M. Rice, and Manfred Sigrist. Magnon dispersion in the field-induced magnetically ordered phase of $\mathrm{tlcucl_3}$. *Phys. Rev. Lett.*, 89:077203, Jul 2002.

[83] H. D. Scammell and O. P. Sushkov. Nonequilibrium quantum mechanics: A "hot quantum soup" of paramagnons. *Phys. Rev. B*, 95:024420, Jan 2017.

[84] Jens Jensen and Henrik Smith. Bose-einstein condensation and the magnetically ordered state of $tlcucl_3$. *Phys. Rev. B*, 80:224419, Dec 2009.

[85] Maciej Fidrysiak and Józef Spałek. Stable high-temperature paramagnons in a three-dimensional antiferromagnet near quantum criticality: Application to $\mathrm{tlcucl_3}$. *Phys. Rev. B*, 95:174437, May 2017.

[86] Elbio Dagotto and T. M. Rice. Surprises on the way from one- to two-dimensional quantum magnets: The ladder materials. *Science*, 271(5249):618–623, 1996.

[87] Oleg P Sushkov. Paramagnons: The long and the short of it. *Nature Physics*, 10(5):339, 2014.

[88] Songbo Jin and Anders W. Sandvik. Universal néel temperature in three-dimensional quantum antiferromagnets. *Phys. Rev. B*, 85:020409, Jan 2012.

[89] G. Kresse and J. Furthmüller. Efficient iterative schemes for ab initio total-energy calculations using a plane-wave basis set. *Phys. Rev. B*, 54:11169–11186, Oct 1996.

[90] G. Kresse and D. Joubert. From ultrasoft pseudopotentials to the projector augmented-wave method. *Phys. Rev. B*, 59:1758–1775, Jan 1999.

[91] T Saha-Dasgupta and R Valenti. Comparative study between two quantum spin systems kcucl3 and tlcucl3. *EPL (Europhysics Letters)*, 60(2):309, 2002.

[92] N. Cavadini, G. Heigold, W. Henggeler, A. Furrer, H.-U. Güdel, K. Krämer, and H. Mutka. Magnetic excitations in the quantum spin system $\mathrm{tlcucl_3}$. *Phys. Rev. B*, 63:172414, Apr 2001.

[93] Akira Oosawa, Tetsuya Kato, Hidekazu Tanaka, K Kakurai, M Müller, and H-J Mikeska. Magnetic excitations in the spin-gap system tlcucl 3. *Physical Review B*, 65(9):094426, 2002.

[94] Tanmoy Das and Alexander V Balatsky. Engineering three-dimensional topological insulators in rashba-type spin-orbit coupled heterostructures. *Nature communications*, 4:1972, 2013.

[95] Xiao-Liang Qi, Taylor L. Hughes, and Shou-Cheng Zhang. Topological field theory of time-reversal invariant insulators. *Phys. Rev. B*, 78:195424, Nov 2008.

[96] Roger S. K. Mong, Andrew M. Essin, and Joel E. Moore. Antiferromagnetic topological insulators. *Phys. Rev. B*, 81:245209, Jun 2010.

[97] M. M. Vazifeh and M. Franz. Quantization and 2π periodicity of the axion action in topological insulators. *Phys. Rev. B*, 82:233103, Dec 2010.

[98] Akihiko Sekine and Kentaro Nomura. Axionic antiferromagnetic insulator phase in a correlated and spin–orbit coupled system. *Journal of the Physical Society of Japan*, 83(10):104709, 2014.

[99] Rundong Li, Jing Wang, Xiao-Liang Qi, and Shou-Cheng Zhang. Dynamical axion field in topological magnetic insulators. *Nature Physics*, 6(4):284, 2010.

[100] S. M. Girvin, A. H. MacDonald, and P. M. Platzman. Collective-excitation gap in the fractional quantum hall effect. *Phys. Rev. Lett.*, 54:581–583, Feb 1985.

[101] S. M. Girvin, A. H. MacDonald, and P. M. Platzman. Magneto-roton theory of collective excitations in the fractional quantum hall effect. *Phys. Rev. B*, 33:2481–2494, Feb 1986.

[102] S. M. Girvin and A. H. MacDonald. Off-diagonal long-range order, oblique confinement, and the fractional quantum hall effect. *Phys. Rev. Lett.*, 58:1252–1255, Mar 1987.

[103] N. Read. Order parameter and ginzburg-landau theory for the fractional quantum hall effect. *Phys. Rev. Lett.*, 62:86–89, Jan 1989.

[104] S. C. Zhang, T. H. Hansson, and S. Kivelson. Effective-field-theory model for the fractional quantum hall effect. *Phys. Rev. Lett.*, 62:82–85, Jan 1989.

[105] Shou Cheng Zhang. The chern–simons–landau–ginzburg theory of the fractional quantum hall effect. *International Journal of Modern Physics B*, 6(01):25–58, 1992.

[106] Shou Cheng Zhang. The chern–simons–landau–ginzburg theory of the fractional quantum hall effect. *International Journal of Modern Physics B*, 6(01):25–58, 1992.

[107] S. C. Zhang, T. H. Hansson, and S. Kivelson. Effective-field-theory model for the fractional quantum hall effect. *Phys. Rev. Lett.*, 62:82–85, Jan 1989.

[108] S. M. Girvin, A. H. MacDonald, and P. M. Platzman. Collective-excitation gap in the fractional quantum hall effect. *Phys. Rev. Lett.*, 54:581–583, Feb 1985.

[109] S. M. Girvin, A. H. MacDonald, and P. M. Platzman. Magneto-roton theory of collective excitations in the fractional quantum hall effect. *Phys. Rev. B*, 33:2481–2494, Feb 1986.

[110] S. M. Girvin and A. H. MacDonald. Off-diagonal long-range order, oblique confinement, and the fractional quantum hall effect. *Phys. Rev. Lett.*, 58:1252–1255, Mar 1987.

[111] N. Read. Order parameter and ginzburg-landau theory for the fractional quantum hall effect. *Phys. Rev. Lett.*, 62:86–89, Jan 1989.

[112] Domènec Espriu, Federico Mescia, and Albert Renau. Axion-higgs interplay in the two-higgs-doublet model. *Phys. Rev. D*, 92:095013, Nov 2015.

[113] J. R. Espinosa, C. Grojean, G. Panico, A. Pomarol, O. Pujolàs, and G. Servant. Cosmological higgs-axion interplay for a naturally small electroweak scale. *Phys. Rev. Lett.*, 115:251803, Dec 2015.

[114] T. Senthil and Michael Levin. Integer quantum hall effect for bosons. *Phys. Rev. Lett.*, 110:046801, Jan 2013.

[115] Yohei Fuji, Yin-Chen He, Subhro Bhattacharjee, and Frank Pollmann. Bridging coupled wires and lattice hamiltonian for two-component bosonic quantum hall states. *Phys. Rev. B*, 93:195143, May 2016.

[116] R. B. Laughlin. Quantized hall conductivity in two dimensions. *Phys. Rev. B*, 23:5632–5633, May 1981.

[117] R. Moessner and S. L. Sondhi. Ising models of quantum frustration. *Phys. Rev. B*, 63:224401, May 2001.

[118] Subir Sachdev. *Quantum phase transitions*. Cambridge university press, 2011.

[119] Shi-Jian Gu. Fidelity approach to quantum phase transitions. *International Journal of Modern Physics B*, 24(23):4371–4458, 2010.

[120] Wen-Long You, Ying-Wai Li, and Shi-Jian Gu. Fidelity, dynamic structure factor, and susceptibility in critical phenomena. *Phys. Rev. E*, 76:022101, Aug 2007.

[121] Lorenzo Campos Venuti and Paolo Zanardi. Quantum critical scaling of the geometric tensors. *Phys. Rev. Lett.*, 99:095701, Aug 2007.

[122] Paolo Zanardi and Nikola Paunković. Ground state overlap and quantum phase transitions. *Phys. Rev. E*, 74:031123, Sep 2006.

[123] Ho-Man Kwok, Wen-Qiang Ning, Shi-Jian Gu, and Hai-Qing Lin. Quantum criticality of the lipkin-meshkov-glick model in terms of fidelity susceptibility. *Phys. Rev. E*, 78:032103, Sep 2008.

[124] David Schwandt, Fabien Alet, and Sylvain Capponi. Quantum monte carlo simulations of fidelity at magnetic quantum phase transitions. *Phys. Rev. Lett.*, 103:170501, Oct 2009.

[125] A. Fabricio Albuquerque, Fabien Alet, Clément Sire, and Sylvain Capponi. Quantum critical scaling of fidelity susceptibility. *Phys. Rev. B*, 81:064418, Feb 2010.

[126] S. Greschner, A. K. Kolezhuk, and T. Vekua. Fidelity susceptibility and conductivity of the current in one-dimensional lattice models with open or periodic boundary conditions. *Phys. Rev. B*, 88:195101, Nov 2013.

[127] G. Sun and T. Vekua. Topological quasi-one-dimensional state of interacting spinless electrons. *Phys. Rev. B*, 93:205137, May 2016.

[128] Bo-Bo Wei and Xiao-Chen Lv. Fidelity susceptibility in the quantum rabi model. *Phys. Rev. A*, 97:013845, Jan 2018.

[129] Wen-Long You and Li He. Generalized fidelity susceptibility at phase transitions. *Journal of Physics: Condensed Matter*, 27(20):205601, 2015.

[130] Yuan-Ming Lu and Ashvin Vishwanath. Theory and classification of interacting integer topological phases in two dimensions: A chern-simons approach. *Phys. Rev. B*, 86:125119, Sep 2012.

[131] C. L. Kane, Ranjan Mukhopadhyay, and T. C. Lubensky. Fractional quantum hall effect in an array of quantum wires. *Phys. Rev. Lett.*, 88:036401, Jan 2002.

[132] Jeffrey C. Y. Teo and C. L. Kane. From luttinger liquid to non-abelian quantum hall states. *Phys. Rev. B*, 89:085101, Feb 2014.

[133] Tarun Grover and Ashvin Vishwanath. Quantum phase transition between integer quantum hall states of bosons. *Phys. Rev. B*, 87:045129, Jan 2013.

[134] Yuan-Ming Lu and Dung-Hai Lee. Quantum phase transitions between bosonic symmetry-protected topological phases in two dimensions: Emergent qed_3 and anyon superfluid. *Phys. Rev. B*, 89:195143, May 2014.